Supplementary information

Enhancing crystal growth using polyelectrolyte solutions and shear flow

Jian-Ke Sun, Yaroslav I. Sobolev, Weiyi Zhang, Qiang Zhuang & Bartosz A. Grzybowski✉

Supplementary Information for manuscript entitled "*Enhancing crystal growth using polyelectrolyte solutions and shear flow*".

CONTENTS:

Section 1. Synthesis and characterization of poly(ionic liquid)s
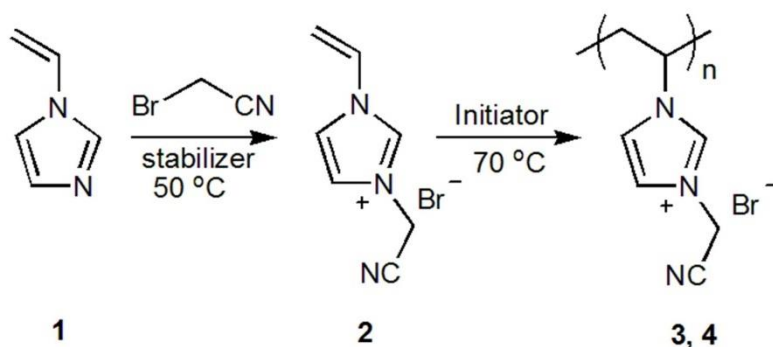
Polymer 3, 4: Poly(3-cyanomethyl-1-vinylimidazolium bromide) (simplified as "PImi-CNBr").
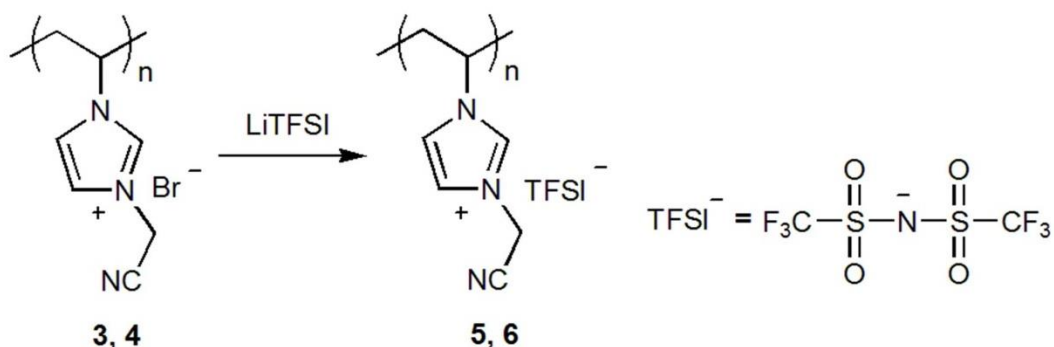
Polymer 5, 6: Poly(3-cyanomethyl-1-vinylimidazolium bis(trifluoromethanesulfonyl)imide) (**PIL-1**).
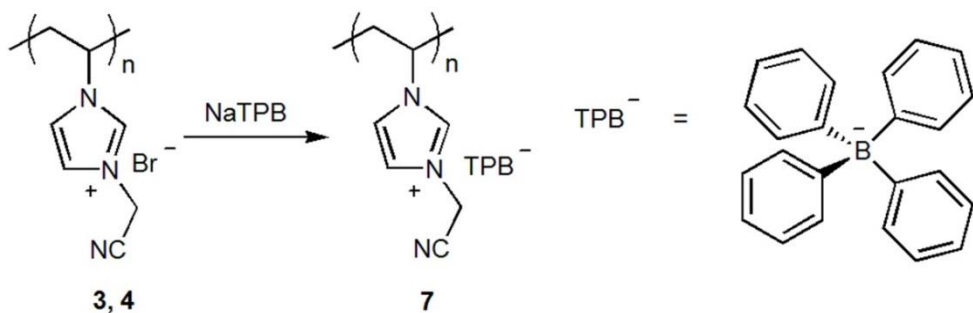
Polymer 7: Poly(3-cyanomethyl-1-vinylimidazolium tetraphenylborate) (**PIL-2**).
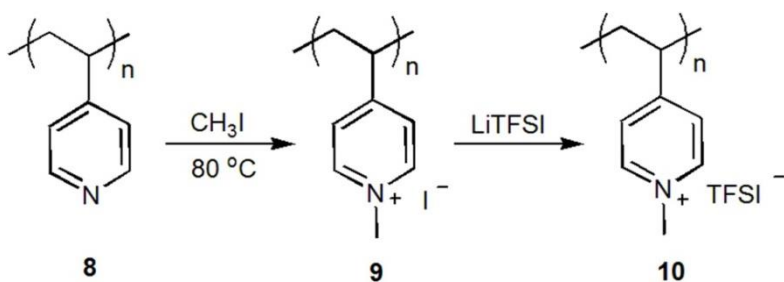
Polymer 10: Poly(1-methyl-4-vinylpyridinium bis(trifluoromethanesulfonyl)imide) (**PIL-4**).
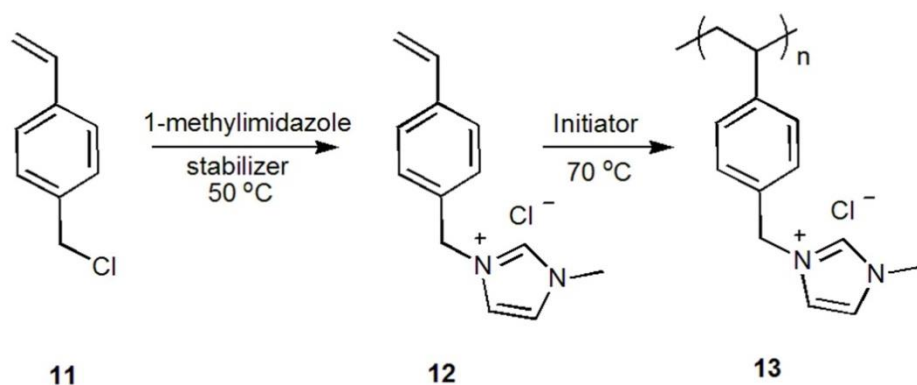
Polymer 13: Poly(3-methyl-1-(4-vinylbenzyl)imidazolium chloride) (**PIL-5**).

Polymer 15: Poly(tetrabutylammonium 4-styrenesulfonate) (**PIL-6**).

Polymer 18: Quaternary ammonium polyethyleneimine (**PIL-7**).

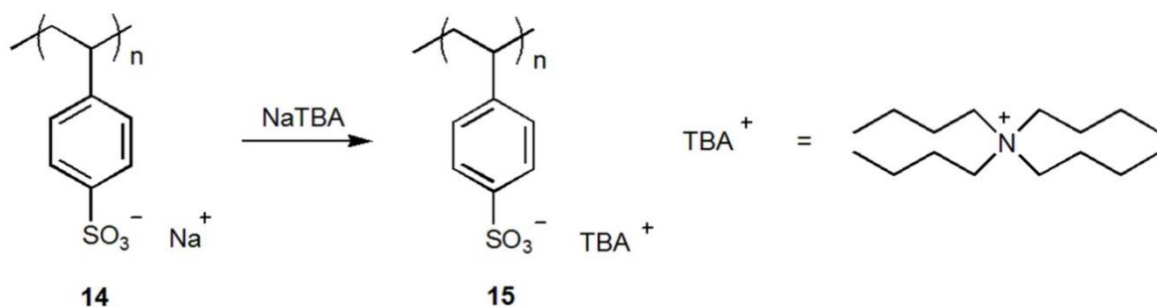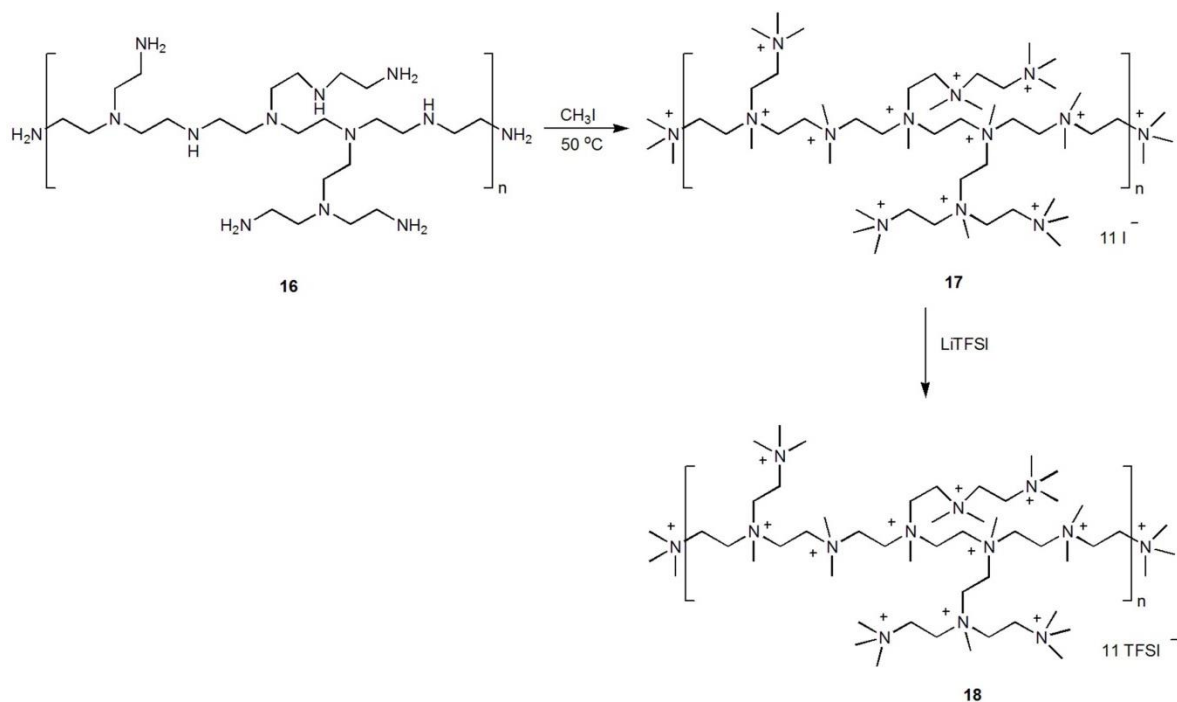**Monomer 2, 12 synthesis**: The preparation methods of 3-cyanomethyl-1-vinylimidazolium bromide (**2**), and 3-methyl-1-(4-vinylbenzyl)imidazolium (**12**) were described in previously published works[S1,S2]

Synthesis of polymer 3, 4: A mixture of monomers (**2**) with VA086 (1.5 mol%) as initiator was added to water (concentration: ~10 g or 15 g monomer in 150 mL solvent, respectively) inside of a 250 mL round-bottom Schlenk flask. The flask was treated with three freeze-pump-thaw cycles and finally purged with argon. The reaction was stirred at 65 °C for 24 h under argon atmosphere. Yellow powders were obtained after dialysis against water, precipitation in tetrahydrofuran (THF), and a vacuum drying process.

Synthesis of polymer 5, 6: Anion metathesis was conducted by dropwise addition of solution 2) into solution 1) : 1) 10 g of polymer **3, 4** dissolved in 1000 mL of deionized water, and 2) 1.1 eq. of lithium bis(trifluoromethanesulfonyl)imide in 50 mL deionized water. Pale white precipitate appeared during the addition process, and then it was filtered off and washed by deionized water 3 times, before dried in vacuum oven (80 °C) overnight.

Synthesis of polymer 7 (PIL-2): Poly(3-cyanomethyl-1-vinylimidazolium tetraphenylborate) (PIL-2) (**9**) was prepared by anion exchange of PImi-CNBr (**3**) with $NaB(C_6H_5)_4$ salt. Anion metathesis was conducted by dropwise addition of solution 2) into solution 1) : 1) 10 g of polymer **3** dissolved in 1000 mL of deionized water, and 2) 1.2 eq. of $NaB(C_6H_5)_4$ in 50 mL deionized water. Pale white precipitate appeared during the addition process, and then it was filtered off and washed by deionized water 3 times, before drying in vacuum oven (80 °C)

overnight. Afterwards, apparent weight-average molecular weight of **PIL-2** was estimated to be 4.44×10^5 g/mol.

Synthesis of polymer PIL-3: The preparation methods of 3-hexyl-1-vinylimidazolium iodide and poly(3-hexyl-1-vinylimidazolium iodide) (**PIL-3**) were described in the literature[S3].

Synthesis of polymer 10 (PIL-4): A mixture of commercially purchased poly(4-vinylpyridine) (5 g, Mw = 1.6×10^5 g/mol) and a 1.5 equivalent amount of iodomethane in 50 mL DMF was added into a 150 mL round flask. After heating at 80 °C for 8 h, dark brown powders were obtained upon precipitation in THF. Anion exchange was then performed in water similar to the process described in the synthesis of polymer **5, 6**. Pale white solids were obtained. Given the 160,000 molecular weight of commercially available poly(4-vinylpyridine), the apparent weight-average molecular weight of **PIL-4** is estimated at 6.09×10^5 g/mol.

Synthesis of polymer 13 (PIL-5): A mixture of monomers (**12**) with AIBN (2 wt%, 50 mg) as initiator was added to water (concentration: 10 g monomer in 150 mL solvent, respectively) inside of a 250 mL round-bottom Schlenk flask. The flask was treated with three freeze-pump-thaw cycles and finally purged with argon. The reaction was stirred at 70 °C for 24 h under argon atmosphere. Yellow powders were obtained after dialysis against water, precipitation in tetrahydrofuran (THF), and a vacuum drying process.

Synthesis of polymer 15 (PIL-6):
A mixture of commercially purchased poly(sodium 4-styrenesulfonate) (10 mL, MW = 7×10^4 g/mol, 30 wt. %) and 1.5 equivalent amount of tetrabutylammonium chloride (TBACl) in 50 mL H_2O was added into a 250 mL round flask. White precipitates appeared and the mixture was extracted with 50 mL DCM three times. The organic phase was concentrated by rotary evaporation and dialyzed in ethanol. The solvent was evaporated in vacuo to afford a yellowish viscous gel. Given the 7×10^4 g/mol molecular weight of commercial poly(sodium 4-styrenesulfonate), the apparent weight-average molecular weight of PIL-6 is estimated at 1.4×10^5 g/mol.

Synthesis of polymer 18 (PIL-7):
The synthesis of quaternary ammonium polyethyleneimine is based on a modified literature procedure[S4]. A solution of commercially available branched poly(ethyleneimine) solution (2.7 g, MW = 6×10^4 g/mol, 50 wt. %) in 50 mL ethanol was added dropwise into 30 mL of iodomethane under vigorously stirring. Then, 1.26 g NaOH was slowly added into the mixture. After heating at 80 °C for 60 h, the solvent was removed by evaporation and the resultant crude polymer was washed with ethanol, and dialyzed in water; yellowish solid was obtained by rotary evaporation. The anion exchange was performed in water similar to the process described in the synthesis of polymer **5, 6**. Yellowish powder was obtained.

Poly(3-cyanomethyl-1-vinylimidazolium bis(trifluoromethanesulfonyl)imide) (PIL-1): (Yield: 97%): ^{1}H NMR (400 MHz, DMSO-d_6, δ, ppm): 9.30 (br, 1H), 7.80 (br, 2H), 5.51 (br, 2H), 4.31 (m, 1H), 2.37 (br, 2H).

Poly(3-cyanomethyl-1-vinylimidazolium tetraphenylborate) (PIL-2): (Yield: 98%): ^{1}H NMR (400 MHz, DMSO-d_6, δ, ppm): 9.61 (br, 1H), 7.89 (br, 2H), 7.35-6.65 (m, 20H), 5.56 (br, 2H), 4.45 (br, 1H), 2.42 (br, 2H).

Poly(3-hexyl-1-vinylimidazolium iodide) (PIL-3): (Yield: 86%): ^{1}H NMR (400 MHz, DMSO-d_6, δ, ppm): 9.51 (br, 1H), 7.80 (br, 2H), 4.60 (br, 1H), 4.12 (br, 2H), 2.60 (br, 2H), 1.86 (br, 2H), 1.35 (br, 6H), 0.92 (br, 3H).

Poly(1-methyl-4-vinylpyridinium bis(trifluoromethanesulfonyl)imide) (PIL-4): (Yield: 95%): ^{1}H NMR (400 MHz, DMSO-d_6, δ, ppm): 8.72 (br, 2H), 7.35 (br, 2H), 4.22 (br, 3H), 1.70 (br, 3H).

Poly(3-methyl-1-(4-vinylbenzyl)imidazolium chloride) (PIL-5): (Yield: 77%): ^{1}H NMR (400 MHz, DMSO-d_6, δ, ppm): 9.05 (br, 1H), 7.32 (br, 2H), 6.42 (br, 2H), 5.21 (br, 2H), 4.43 (br, 3H), 3.68 (br, 2H), 1.20 (br, 3H).

Poly(tetrabutylammonium 4-styrenesulfonate) (PIL-6) (Yield: 97%): ^{1}H NMR (400 MHz, CDCl$_3$, δ, ppm): 7.56 (br, 2H), 6.50 (br, 2H), 3.17 (br, 8H), 1.45 (br, 8H), 1.21 (br, 8H), 0.79 (br, 12H).

The chemical structures of the polymers used in the present work were confirmed by ^{1}H NMR spectra in **Figures S1**-**S7.**
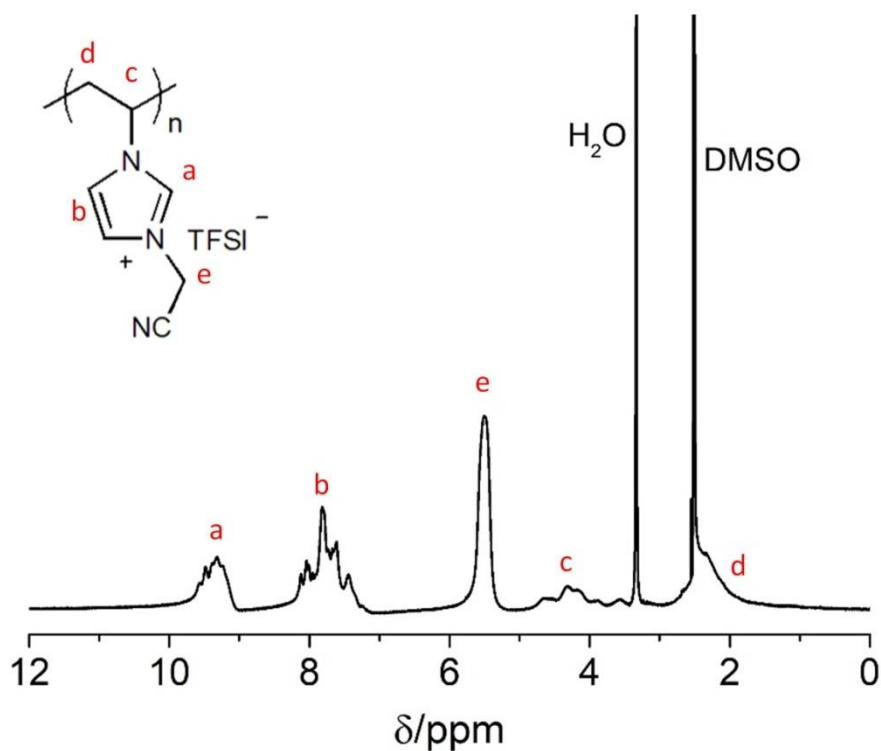
Figure S1 │ Chemical structure and ^{1}H-NMR spectrum of poly(3-cyanomethyl-1-vinylimidazolium bis(trifluoromethanesulfonyl)imide) (**PIL-1**).
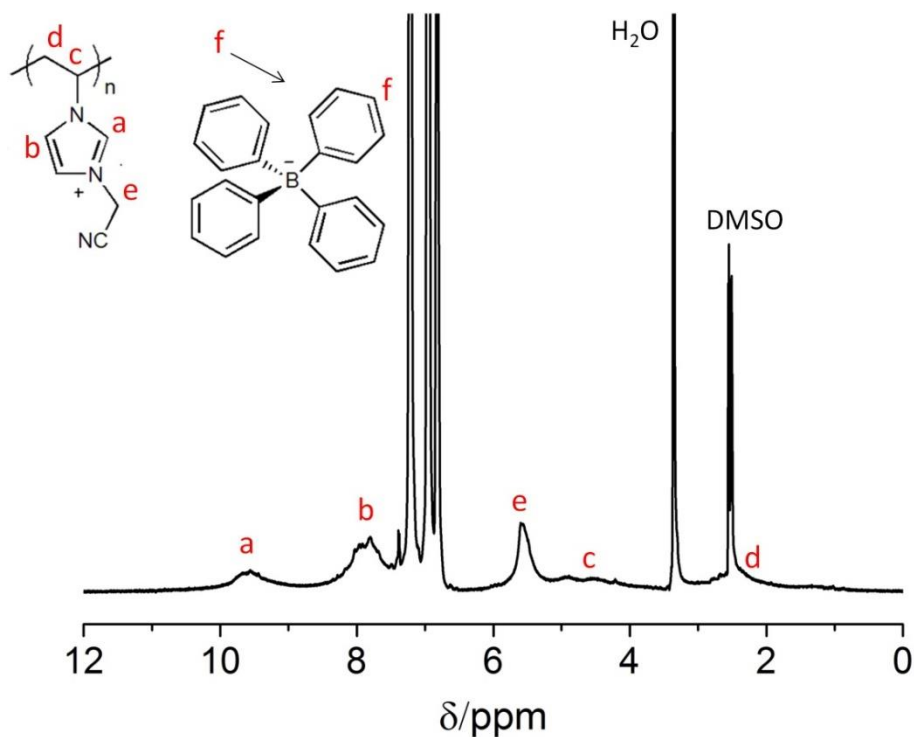
Figure S2 │ Chemical structure and ^{1}H-NMR spectrum of poly(3-cyanomethyl-1-vinylimidazolium tetraphenylborate) (**PIL-2**).
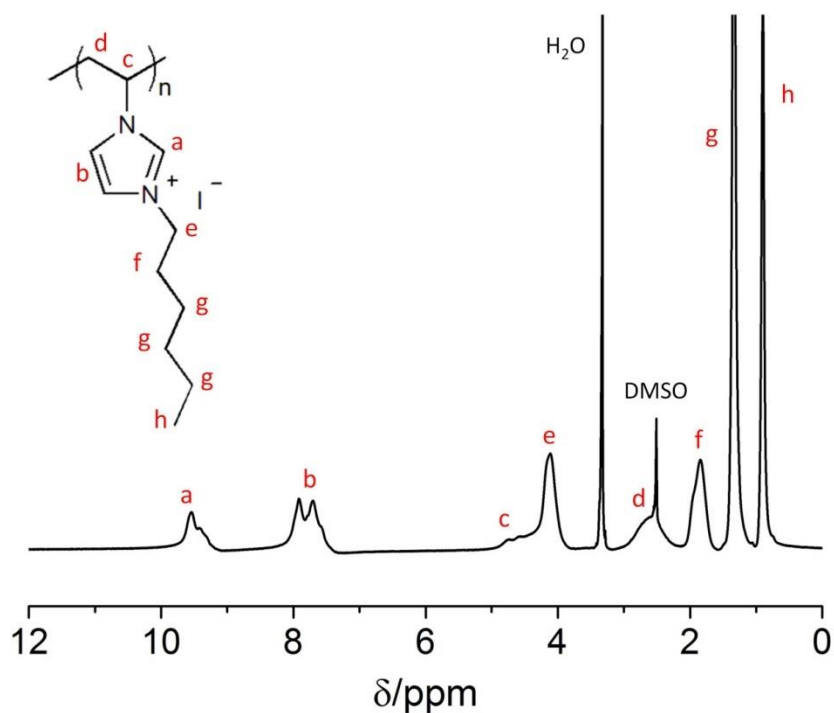
Figure S3 | Chemical structure and ^{1}H-NMR spectrum of poly(3-hexyl-1-vinylimidazolium iodide) (**PIL-3**).

Figure S4 | Chemical structure and ^{1}H-NMR spectrum of poly(1-methyl-4-vinylpyridinium bis(trifluoromethanesulfonyl)imide) (**PIL-4**).
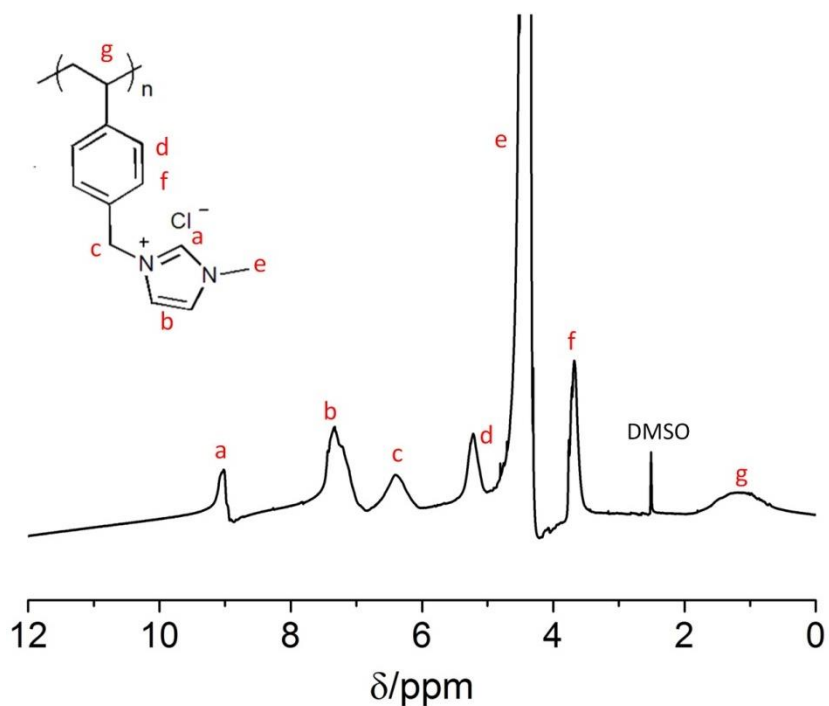
Figure S5 │ Chemical structure and ^{1}H-NMR spectrum of poly(3-methyl-1-(4-vinylbenzyl)imidazolium chloride) (**PIL-5**).

Figure S6 │ Chemical structure and ^{1}H-NMR spectrum of poly(tetrabutylammonium 4-styrenesulfonate) (**PIL-6**).
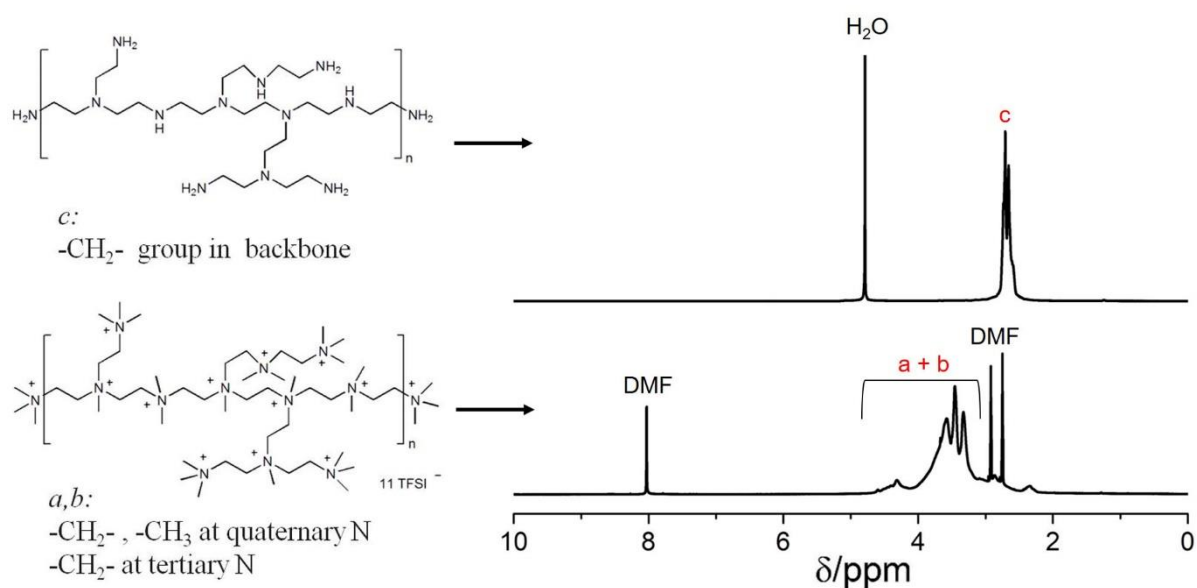
Figure S7 | Chemical structure and ^{1}H-NMR spectrum of branched polyethyleneimine (top row) and quaternary ammonium polyethyleneimine (PIL-7) (Bottom row).

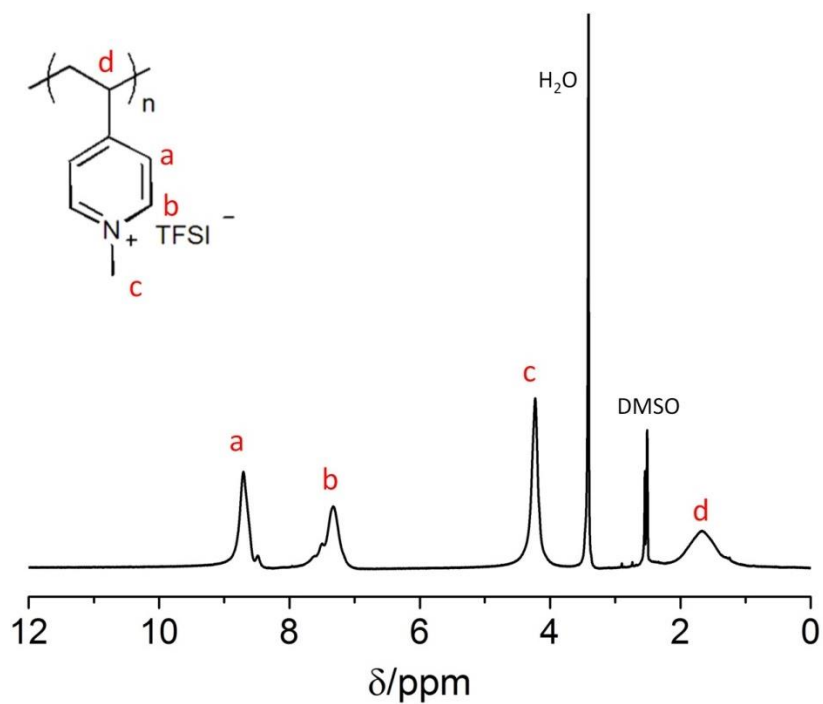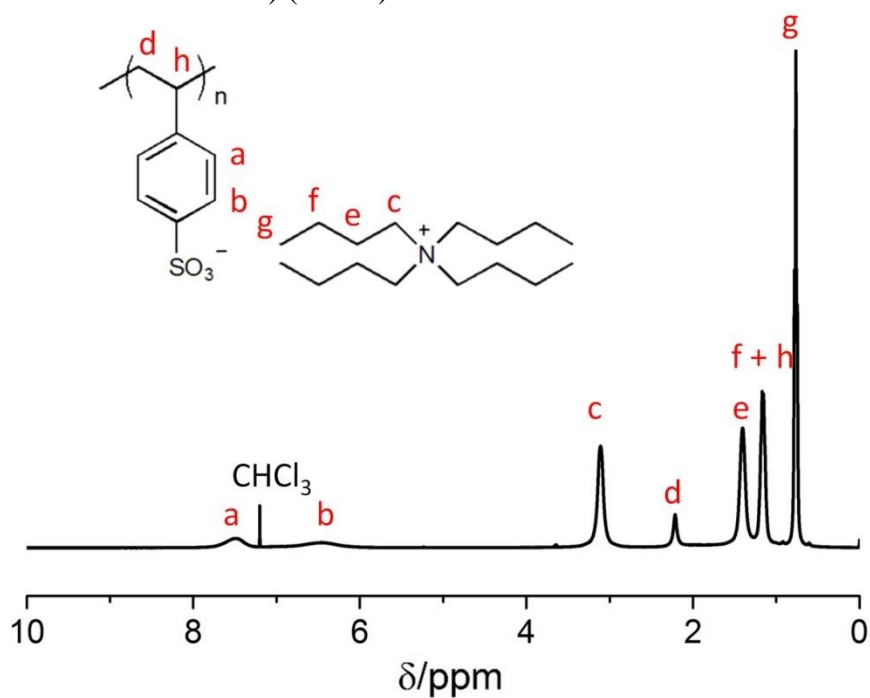The appearance of the new peaks at chemical shift (δ) in the range of 3.0–4.5 ppm in the ^{1}H NMR spectrum of quaternary ammonium polyethyleneimine was attributed to -CH$_3$ or -CH$_2$- group attached to the quaternized ammonium groups[S5]. At δ = 2.4 ppm, one can observe small peak that can be ascribed to -CH$_2$- groups in the non-charged PEI polymer backbone, which indicates that the methylation of the bPEI was not complete. This was also encountered in the same study by post-synthetic modification [S5]. The degree of substitution by the methyl group was determined from the ^{1}H NMR spectrum. It was estimated that quaternary ammonium polyethyleneimine contains about 94 % of the quaternary ammonium groups.
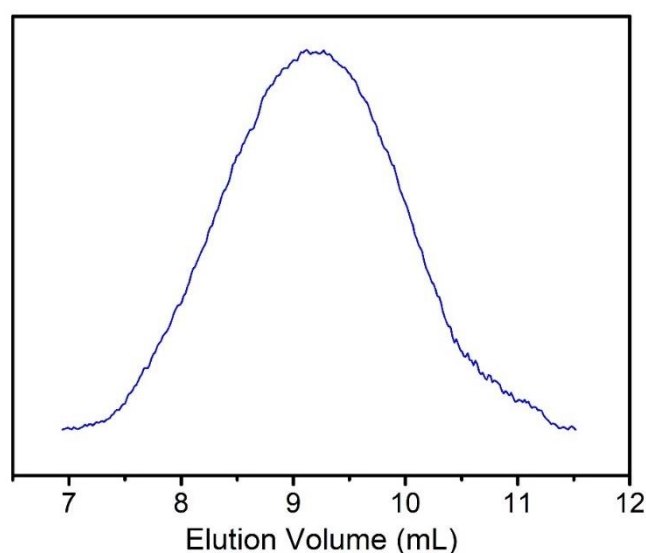
Figure S8 | GPC trace measured for poly(3-cyanomethyl-1-vinylimidazolium bromide) (3).

The apparent weight-average molecular weight and PDI value of poly(3-cyanomethyl-1-vinylimidazolium bromide) (PImi-CNBr) (3) was measured to be 2.10×10^5 g/mol and 4.09, respectively (measured by GPC, eluent: water with a mixture of 80% acetate buffer and 20% methanol). Poly(3-cyanomethyl-1-vinylimidazolium bis(trifluoromethanesulfonyl)imide) (5)

was prepared by anion exchange of PImi-CNBr with LiTFSI salt. Therefore, the apparent weight-average molecular weight of PImi-CNTFSI (**6**) is calculated to be 4.02×10^5 g/mol.
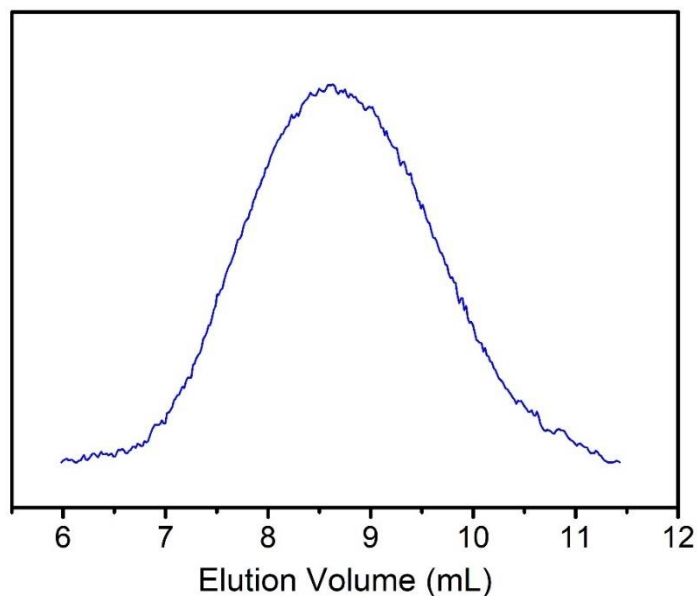
Figure S9｜GPC trace measured for poly(3-cyanomethyl-1-vinylimidazolium bromide) (**4**). The apparent weight-average molecular weight and PDI value of poly(3-cyanomethyl-1-vinylimidazolium bromide) (PImi-CNBr) (**4**) was measured to be 4.43×10^5 g/mol and 5.18, respectively. The apparent weight-average molecular weight of poly(3-cyanomethyl-1-vinylimidazolium bis(trifluoromethanesulfonyl)imide) (**6**) is calculated to be 8.49×10^5 g/mol.

Figure S10｜GPC trace measured for poly(3-methyl-1-(4-vinylbenzyl)imidazolium chloride) (**PIL-5**). The apparent weight-average molecular weight and PDI value of PIL-5 was measured to be 2.27×10^5 g/mol and 2.34, respectively.
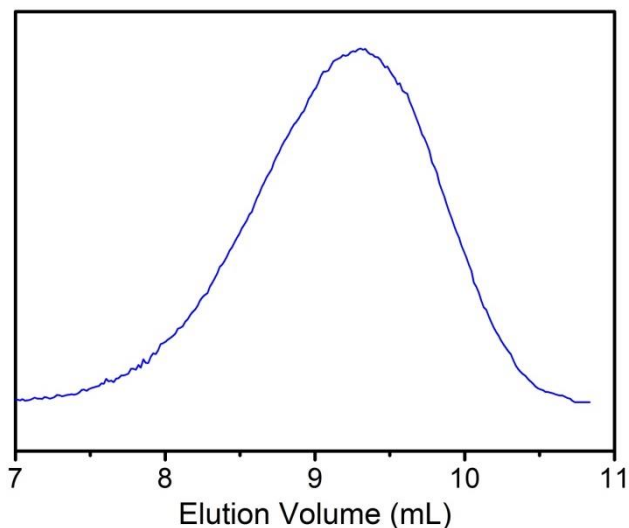
Section 2. Methods and additional data from crystal growth experiments

2.1. Measurement of equilibrium saturation concentration of trimesic acid in growth solutions

Saturation levels were measured by first adding known amounts of trimesic acid into target solution until saturation is achieved, then diluting with pure (i.e., containing no trimesic acid) solution until all crystals have dissolved. This resulted in two bounds on the saturation (equilibrium) concentration; half-distance between these bounds is indicated as measurement error in **Table S1**. All experiments were performed at 25.0 °C in a thermostatic chamber (Mean Science TEMI1300, accuracy of temperature stabilization 0.1 °C). In this "direct" method, presence or absence of crystals in the solution was determined visually *in situ* by scanning the entire solution volume with 20X-magnification optical microscope.

For experiments without shear, this procedure was further validated by measuring trimesic acid saturation concentration in solution by UV absorption spectroscopy. Trimesic acid has aromatic absorption bands in 280-300 nm region, while other substances in the solution do not absorb in this region. Narrow spectral width of these bands allowed for efficient background elimination by derivative spectroscopy. Undersaturated solutions of trimesic acid in PIL-1/DMF were used for calibrating absorption with respect to trimesic acid concentration. Resulting saturation (equilibrium) concentrations obtained spectroscopically for trimesic acid in PIL-1/DMF (MW 402 000 g/mol and MW 849 000 g/mol) fall within the bounds of "direct" measurements described above and indicated in **Table S1**. However, since our solutions are quite viscous, they had to be centrifugated to remove the crystals from the solution before measuring the absorption spectra. Centrifuge temperature during this procedure was stabilized to 25.0 ± 0.1 °C.

On timescales 3-8 hours, relevant to our crystal growth experiments, mean shear $\dot{\gamma} = 167$ s^{-1} indeed decreases global solubility of TA in PIL-1/DMF (MW 8.49×10^5 g/mol) from 167.2±2.8 mM to 161.6±0.8 mM. Only at much longer times (3 days) under shear ($\dot{\gamma} = 167$ s^{-1}), solubility of TA in PIL-1/DMF solutions slowly grows (bottom two lines in Table S1). There can be many reasons for this long-term trend, including breaking of polymer chains and some unidentified slow chemical transofrmations progressing in the solution.

Although for lower shear rates or shorter polymer chains the global solubility change upon applying shear is less than our ~2% measurement uncertainty, the proposed mechanism of shear-driven crystal growth enhancement only requires small local solubility differences (~ 0.1%) caused by large differences of local shears, which does not necessarily have to translate into large decrease of global solubility by mean shear.

Table S1. Equilibrium saturation concentration (solubility) of trimesic acid in various solutions. Concentration of PIL-1 or its monomer in all cases 300 mg / 0.75 mL DMF. Temperature (25.0 ± 0.1) °C.

Solution and condition	Equilibrium saturation concentration (solubility)		
	Molar, mM	mg per mL of DMF	mg per 0.75 mL DMF
DMF	587 ± 8	123.4 ±1.6	92.6±1.2
Monomer of PIL-1	282 ± 8	73±2	54.6±1.5
PIL-1, MW 402 000 g/mol, no shear (8 hours)	164.8 ± 3.2	41.5±0.8	31.1±0.6
PIL-1, MW 849 000 g/mol, no shear (8 hours)	167.2 ± 2.8	42.1±0.7	31.6±0.5
PIL-1, MW 849 000 g/mol, $\dot\gamma = 167$ s^{-1} (3 hours)	161.6 ± 0.8	40.7±0.2	30.5±0.15
PIL-1, MW 402 000 g/mol, $\dot\gamma = 167$ s^{-1} (3 days)	183.1 ± 2.4	46.1±0.6	28.9±0.4
PIL-1, MW 849 000 g/mol, $\dot\gamma = 167$ s^{-1} (3 days)	227 ± 8	57.3±2.0	35.9±1.2

2.2. Methods for crystal growth experiments

The experiments described below are for the stirred solutions in the presence of PIL polymers. Control experiments with the same-composition solutions and same times but no stirring were also performed in each case. All experiments were performed at 25.0 °C in a thermostatic chamber (Mean Science TEMI1300). PXRD patterns were collected on Rigaku Miniplex 600 (for crystals **2**, **3**, **5**, **9**, **10**, **11**, **12**, **14**, **18**) or PW3040/60 X'per PRO, PANalytical (for crystals **1**, **4**, **6**, **7**, **8**, **13**, **17**, **19**, **20**) instruments using Cu-Kα radiation (λ = 1.54056 Å). Diffraction of sample holder (background) was subtracted from data and relative portion of crystalline phase was evaluated by peak fitting, as illustrated in **Figure S11**.

Single-crystal X-ray diffraction was measured on a Bruker D8 VENTURE diffractometer with a graphite-monochromated Ga-Kα radiation (λ = 1.34139 Å) at 193 K. The data sets were corrected for Lorentz and polarization factors as well as for absorption by a multiscan method. The structures were solved by direct methods and refined by full-matrix least-squares fitting on F^2 by SHELX-2018. All non-hydrogen atoms were refined with anisotropic thermal parameters. The hydrogen atoms on the carbon atoms were placed in a calculated position with isotropic displacement parameters. Crystallographic data and structure refinements can be found in Supplementary **Tables S2-S4**

2, 5-dihydroxyterephthalic acid. 30 mg of commercial 2, 5-dihydroxyterephthalic acid powder (from Sigma-Aldrich; cat# 382132) was dissolved into 0.35 mL of DMF, which was subsequently added into another batch of DMF solution (0.4 mL) containing 300 mg of PIL-1. The mixture was stirred at 400 rpm for 10 min.

Anthracene-9-carboxylic acid. 40 mg of commercial anthracene-9-carboxylic acid (from Sigma-Aldrich; cat# A89405) was dissolved into 0.2 mL of DMF, which was

subsequently added into another batch of DMF solution (0.2 mL) containing 240 mg of PIL-1. The mixture was stirred at 400 rpm for 20 min.

3-cyanomethyl-1-vinylimidazolium bromide. 20 mg of 4-cyanomethyl-1-vinyl-imidazolium bromide (synthesized as described previously in *Chem. Mater.* **22**, 5003–5012, 2010) was dissolved into 0.1 mL of methanol, which was subsequently added into another batch of methanol solution (0.1 mL) containing 128 mg of PIL-6. The mixture was stirred at 400 rpm for 5 min.

Ethyl viologen dibromide. 18 mg of ethyl viologen dibromide (from Sigma-Aldrich; cat# 384097) was dissolved into 0.1 mL of methanol, which was subsequently added into another batch of methanol solution (0.1 mL) containing 100 mg of PIL-6. The mixture was stirred at 400 rpm for 10 min.

p-Nitroaniline. 80 mg of *p*-nitroaniline (from Sigma-Aldrich; cat#185310) was dissolved into 0.1 mL of DMF, which was subsequently added into another batch of DMF solution (0.1 mL) containing 200 mg of PIL-1. The mixture was stirred at 400 rpm for 10 h.

Tetrathiafulvalene. 4.6 mg of commercial tetrathiafulvalene (from Sigma-Aldrich; cat# 183180) was dissolved into 0.2 mL 1:1 v/v DCM-MeOH mixture, which was subsequently added into 0.1 mL of DCM containing 50 mg of PIL-3. The mixture was stirred at 400 rpm for 5 min.

1,2,4,5-Tetrakis(4-carboxyphenyl)benzene. 21 mg of 1,2,4,5-Tetrakis(4-carboxyphenyl)benzene (from Sigma-Aldrich; cat# 715298) was dissolved into 0.6 mL of DMF, which was subsequently added into another batch of DMF solution (0.1 mL) containing 100 mg of PIL-7. The mixture was stirred at 400 rpm for 2 h.

Meso-tetra (carboxyphenyl) porphyrin. 2 mg of Meso-tetra (carboxyphenyl) porphyrin (from TCI Chemicals; cat# A5015) was dissolved into 0.35 mL of DMF, which was subsequently added into another batch of DMF solution (0.1 mL) containing 70 mg of PIL-1. The mixture was stirred at 400 rpm for 10 min.

β-Cyclodextrin. 40 mg of commercial *β*-cyclodextrin powder (from TCI Chemicals; cat# C0777) was dissolved into 0.2 mL of DMF, which was subsequently added into another batch of DMF solution (0.2 mL) containing 150 mg of PIL-1. The mixture was stirred at 400 rpm for 10 h.

Sodium Iodide. 46 mg of sodium iodide (from Sigma-Aldrich; cat# 409286) was dissolved into 0.45 mL of DMF, which was subsequently added into another batch of DMF solution (0.2 mL) containing 300 mg of PIL-3. The mixture was stirred at 400 rpm for 20 min.

Phosphotungstic acid. 75 mg of phosphotungstic acid (from Sigma-Aldrich; cat# 455970) was dissolved into 0.1 mL of water, which was subsequently added into another batch of water solution (0.35 mL) containing 75 mg of PIL-5. Then the mixture start to stirring at speed of 400 rpm. The mixture was stirred at 400 rpm for 3 h.

Iron(III) meso-tetraphenylporphine chloride. 3.5 mg of commercial Iron(III) meso-tetraphenylporphine chloride (from Sigma-Aldrich; cat# 259071) was dissolved into 0.1 mL of DCM, which was subsequently added into another batch of DCM solution (0.1 mL) containing 100 mg of PIL-6. The mixture was stirred at 400 rpm for 3 min.

Rhodium(I) tris(triphenylphosphine) chloride. 8 mg of commercial rhodium(I) tris(triphenylphosphine) chloride (from Sigma-Aldrich; cat# 205036) was dissolved into 0.1

mL of DCM, which was subsequently added into another batch of DCM solution (0.1 mL) containing 30 mg of PIL-3. The mixture was stirred at 400 rpm for 6 min.

Hen Egg White Lysozyme. 25 mg of Hen Egg White Lysozyme ($\geq$ 40000 units/mg; from Sigma-Aldrich; cat# L6876) was dissolved into 0.2 ml of water, which was subsequently added into another batch of NaAc/HAc buffer solution (0.5 mL, pH = 5.2) containing 300 mg of PIL-5 and 25 mg of NaCl. The mixture was stirred at 400 rpm for 2 h. ***Note:*** An additional control system containing the same concentration of NaCl and PIL-5 in NaAc/HAc buffer but not protein did not yield any crystals after 2 h of stirring.

Thaumatin. 30 mg of thaumatin (from Sigma-Aldrich; cat# T7638) was dissolved into 0.2 mL of N-(carbamoylmethyl)iminodiacetic acid (ADA) buffer solution (pH = 7), which was subsequently added into another 0.1 mL batch of water solution containing 50 mg of PIL-5 and 20 mg of sodium potassium tartrate. The mixture was stirred at 400 rpm for 16 h. ***Note:*** An additional control system containing the same concentration of sodium potassium tartrate and PIL-5 in ADA buffer but not protein did not yield any crystals after 16 h of stirring.

Porous molecular cage (CC3-R). The cage was synthesized as described previously (*Nat. Mater.* **8**, 973-978, 2009). 10 mg of the as-synthesized CC3-R was dissolved into 0.1 mL of DCM, which was subsequently added into another batch of DCM solution (0.5 mL) containing 100 mg of PIL-3. The mixture was stirred at 400 rpm for 10 min.

Metal-organic polyhedron (MOP, $Na_6H_{18}[Cu_{24}(C)_{24}]$, C = 5-sulfo-1,3-benzenedicarboxylic acid). The MOP was synthesized as described previously (*Nat. Chem.* **2**, 893-898, 2010). 6 mg of the as-synthesized MOP was dissolved into 0.2 mL of methanol, which was subsequently added into another batch of methanol solution (0.1 mL) containing 100 mg of PIL-5. The mixture was stirred at 400 rpm for 10 min.

Metal-organic framework (MOF, HKUST-1). 100 mg of PIL-4 and 42 mg of TA were dissolved in 0.5 mL of DMF, which were subsequently added into another batch of DMF solution (0.25 mL) containing 60 mg of $Cu(NO_3)_2 \cdot 3H_2O$ (from Sigma-Aldrich; cat# 61194). The mixture was stirred at 400 rpm for 10 h. ***Note:*** An additional control experiment was performed by mixing the same concentrated TA and $Cu(NO_3)_2 \cdot 3H_2O$ in DMF solution without PIL-4, under continuous stirring (400 rpm). There were no crystals after 10 h, while the similar sized HKUST-1 single crystals could be obtained after stirring for 30 h.

Covalent organic framework (COF, TAPB-BTCA). 50 mg of PIL-1 and 4 mg of 1,3,5-benzenetricarbaldehyde (BTCA; from Sigma-Aldrich, cat# 753491) were dissolved in 0.5 mL of DMSO, and then they were added into another batch of DMSO solution (0.5 mL) containing 6 mg of 1,3,5-tris(4-aminophenyl)benzene (TAPB; from TCI chemicals, cat# T2728). The mixture was stirred at 400 rpm for 15 min. ***Note:*** Control experiment without stirring did not yield any crystals after 15 min; the crystals were collected and inspected only after 2 h. Another control experiment was performed by mixing the same concentrations of BTCA and TAPB in DMSO but without PIL-1. With the same stirring speed, no crystals were apparent after 15 min of rotation but appeared after stirring for 3 h.

2.3. Size and quality of crystals grown by different methods

Table S2. **Single-crystal XRD data and structure refinements** for TA grown in the presence of PIL-1 under shear

Formula	$C_{15}H_{20}N_2O_8$
Fw	356.33
T/K	193(2)
λ/ Å	1.34139
Space group	$P2_1/c$
a/ Å	16.7038(7)
b/ Å	14.4202(6)
c/ Å	7.2675(3)
α/°	90
β/°	90.355(2)
γ/°	90
V/ Å^3	1750.50(13)
Z	4
D_{calcd}/g.cm^{-3}	1.352
μ(Ga-Ka)/mm^{-1}	0.602
F(000)	752
Reflections collected / unique	9075 / 2739 [R(int) = 0.0306]
GOF on F^2	1.045
[a]R$_1$, [b]wR$_2$[I>2σ (I)]	0.0374, 0.0922
R$_1$, wR$_2$(all data)	0.0440, 0.0980

[a], $R_1 = \Sigma||F_o| - |F_c||/\Sigma|F_o|$;   [b], $wR_2 = \{\Sigma w[(F_o)^2 - (F_c)^2]^2/\Sigma w[(F_o)^2]^2\}^{1/2}$

Table S3. **Single-crystal XRD data and structure refinements** for TA grown by slow evaporation of solvent (with no PIL or shear)

Formula	$C_{15}H_{20}N_2O_8$
Fw	356.33
T/K	193(2)
λ/ Å	1.34139
Space group	$P2_1/c$
a/ Å	16.7090(9)
b/ Å	14.4157(8)
c/ Å	7.2682(4)
α/°	90
β/°	90.039(2)
γ/°	90
V/ Å^3	1750.70(17)
Z	4
D_{calcd}/g.cm^{-3}	1.352
μ(Ga-Ka)/mm^{-1}	0.602
F(000)	752
Reflections collected / unique	9948 /2864 [R(int) = 0.0358]

GOF on F^2	1.038
[a]R_1, [b]wR$_2$[I>2σ (I)]	0.0341, 0.0888
R_1, wR$_2$(all data)	0.0368, 0.0912

[a], $R_1 = \sum||F_o| -|F_c||/\sum|F_o|$;   [b], wR$_2 = \{\sum w[(F_o)^2 -(F_c)^2]^2/\sum w[(F_o)^2]^2\}^{1/2}$

Table S4. **Single-crystal XRD data and structure refinements** for TA grown by recrystallization with no PIL or shear (preparing a growth solution saturated at 36 °C and cooling it down to 25 °C)

Formula	$C_{15}H_{20}N_2O_8$
Fw	356.33
T/K	193(2)
λ/ Å	1.34139
Space group	$P2_1/c$
a/ Å	16.7084(10)
b/ Å	14.4243(9)
c/ Å	7.2680(4)
α/°	90
β/°	90.036(3)
γ/°	90
V/ Å^3	1751.64(18)
Z	4
D_{calcd}/g.cm^{-3}	1.346
μ(Ga-Ka)/mm^{-1}	0.600
F(000)	752
Reflections collected / unique	17526 / 4007 [R(int) = 0.0591]
GOF on F^2	1.060
[a]R_1, [b]wR$_2$[I>2σ (I)]	0.0415, 0.1048
R_1, wR$_2$(all data)	0.0472, 0.1097

[a], $R_1 = \sum||F_o| -|F_c||/\sum|F_o|$;   [b], wR$_2 = \{\sum w[(F_o)^2 -(F_c)^2]^2/\sum w[(F_o)^2]^2\}^{1/2}$
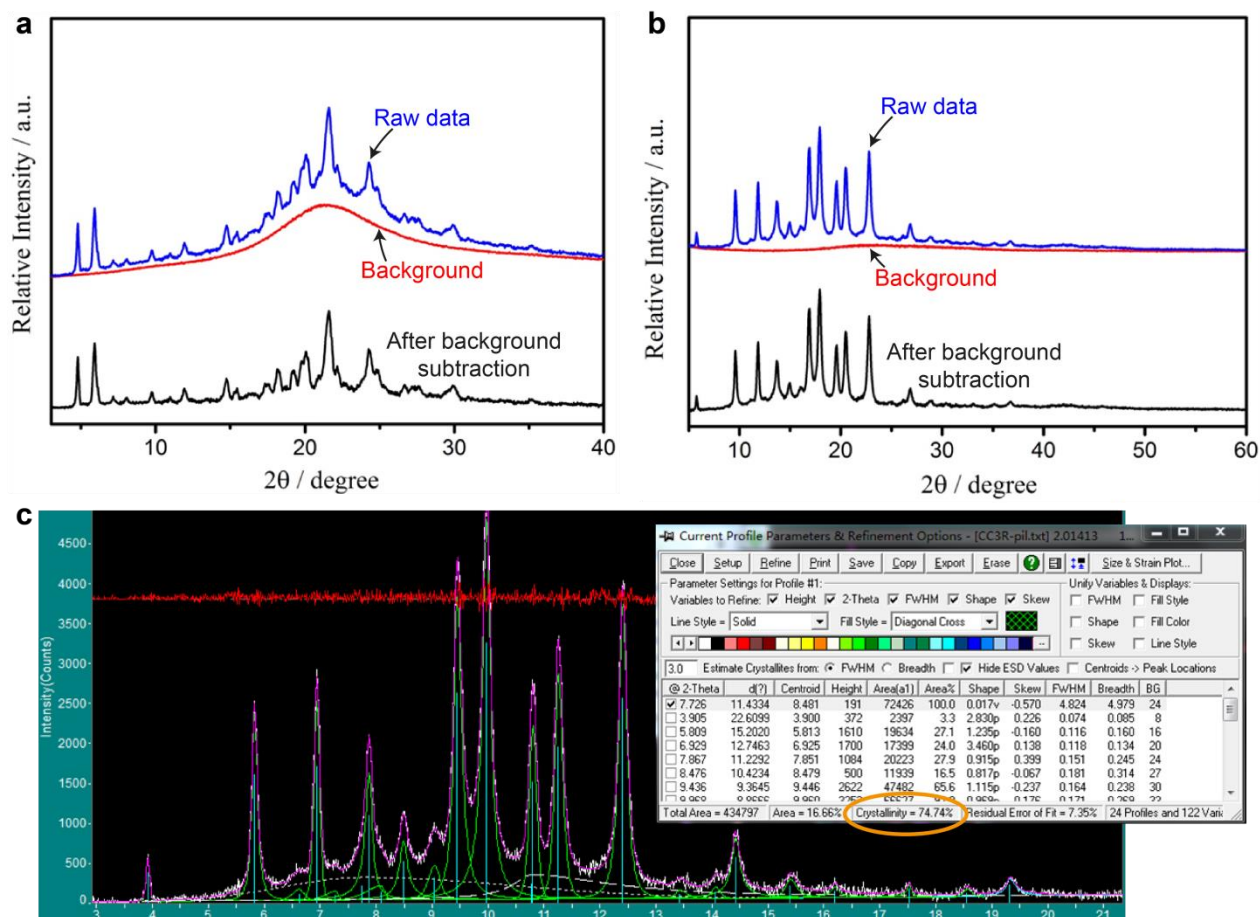
Figure S11 │ **Illustration to the procedure of PXRD data analysis**. **a-b,** PXRD curves before (blue) and after (black) subtraction of the diffraction curve of the empty sample holder (red) shown here for two devices we used in the present work: Rigaku Miniplex 600 (**a**) and PW3040/60 X'per PRO, PANalytical (**b**). Crystals used for this particular illustration are: Meso-tetra (carboxyphenyl) porphyrin (**a**) and CC3-R cage (**b**), both grown in the presence of PIL and shear. **c,** Analysis of the CC3-R cage diffraction pattern (after background subtraction) with MDI jade 6 software to determine crystallinity and residual error of fit. Diffraction pattern (white curve) was decomposed into the coherent contributions from the crystalline phase (narrow peaks, green) and the amorphous phase component (wide low profiles, white dashed). The overall fit curve is shown in purple, and its discrepancy with experimental data (residual error of fit) is shown in red, with a vertical offset for convenience. Peak fitting settings and results are shown in the screenshot on the right. Relative portion of the crystalline phase ("Crystallinity", circled with orange ellipse on the bottom of the output window) is evaluated as the ratio A_{cryst}/A_{net} of the integrated area A_{cryst} of the crystalline component and the integrated area A_{net} of the entire diffraction pattern. **Figure S12** shows crystallinities and residual errors of fit for all crystals analyzes. **Figures S16-S28, S31-S35** show individual PXRD spectra after background subtraction.
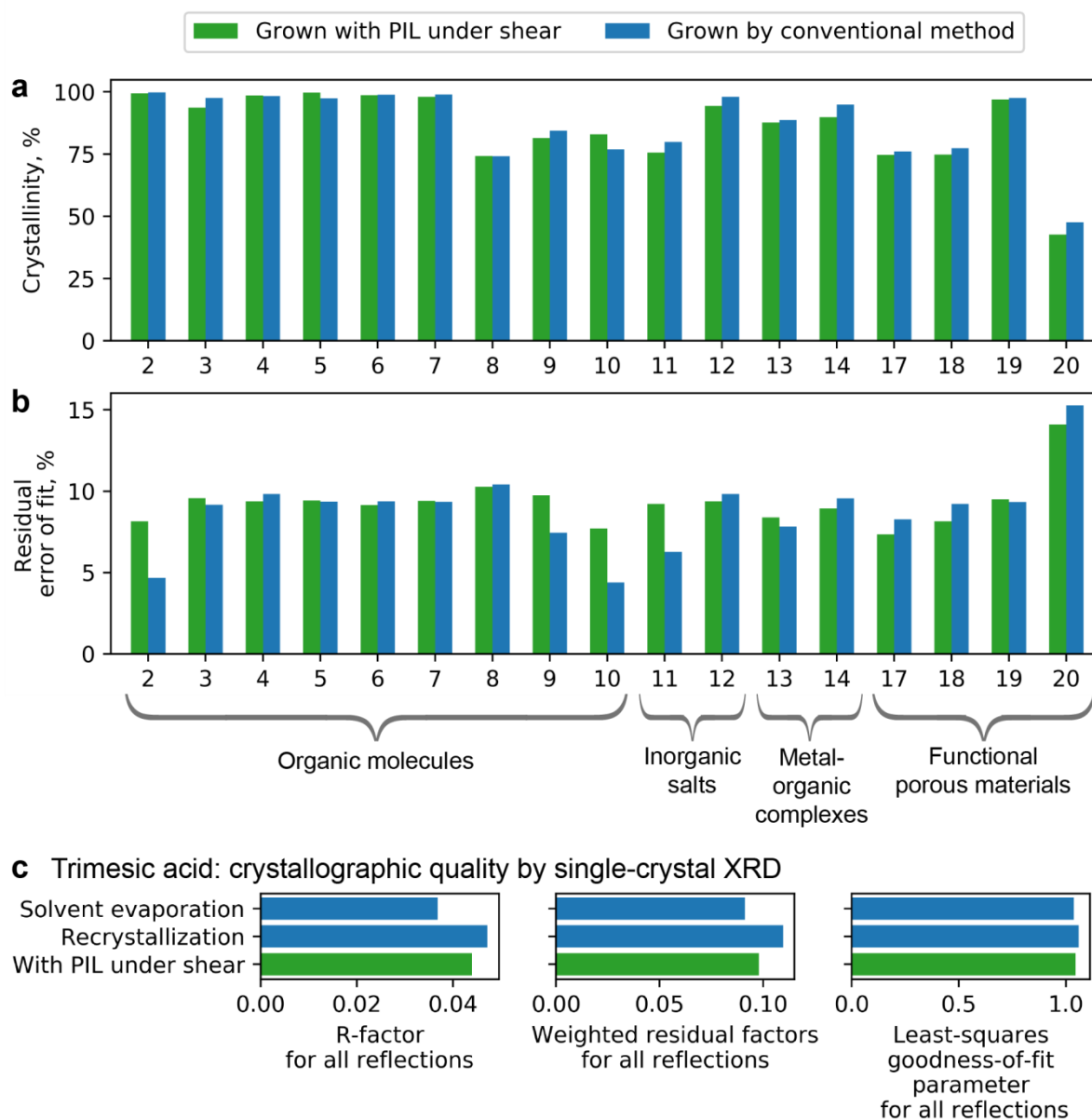
Figure S12 │ Crystallographic quality of crystals grown with PIL under shear compared to those grown by a conventional method. a, Crystallinities and **b,** residual errors of diffraction pattern fit calculated using experimental PXRD patterns as described in **Figure S11** for the same substances as in the main-text **Figure 3** (except trimesic acid **1** for which data is provided in **Figure 1f** and macromolecules **15-16**, for which UV-Vis spectra were taken). Green bars correspond to crystals grown in the presence of PIL and shear. Blue bars correspond to best crystals obtained by a conventional method or to literature data (see **Figures S16-S28, S31-S35** for more details for each substance). Typically, slow evaporation of solvent was used as a conventional method whereby a container with undersaturated solution of a target substance was covered with perforated parafilm slowing down the solvent evaporation and left at room temperature for several days until desired crystals were produced. **c,** Comparison of crystallographic qualities (as evaluated by single-crystal XRD) for trimesic crystals grown either by slow evaporation of solvent, by recrystallization (preparing undersaturated growth solution at 36 °C and cooling it down to 25 °C), or in the presence of PIL under shear. For each

18

of the three crystallographic parameters (R-factor, the weighted residual factors, and least-square goodness-of-fit parameter), lower value is associated with higher crystallographic quality. For more details see **Tables S2-S4**.
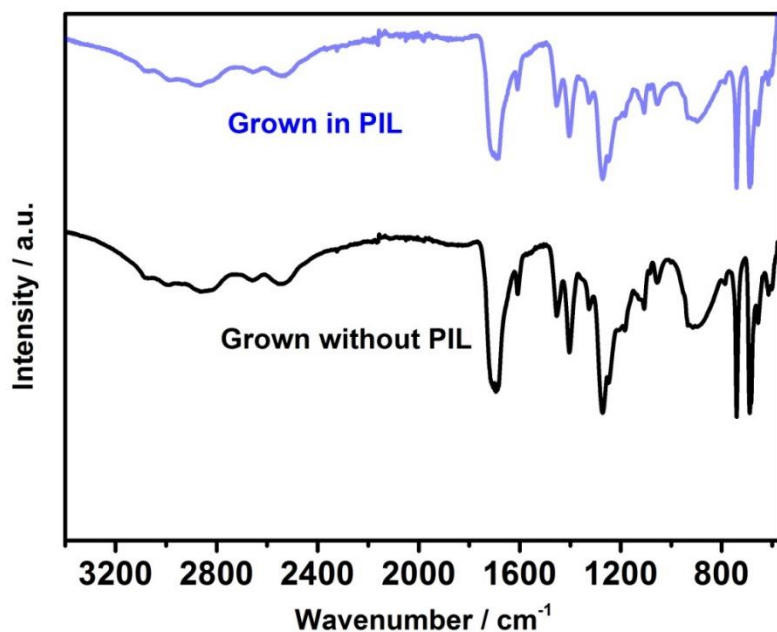

Figure S13 ｜ The FT-IR spectra of the TA single crystals (isolated from PIL-DMF solution and further purified before measuring FT-IR) grown in PIL-1 under shear (blue) and by direct evaporation from TA-containing DMF solution (black).
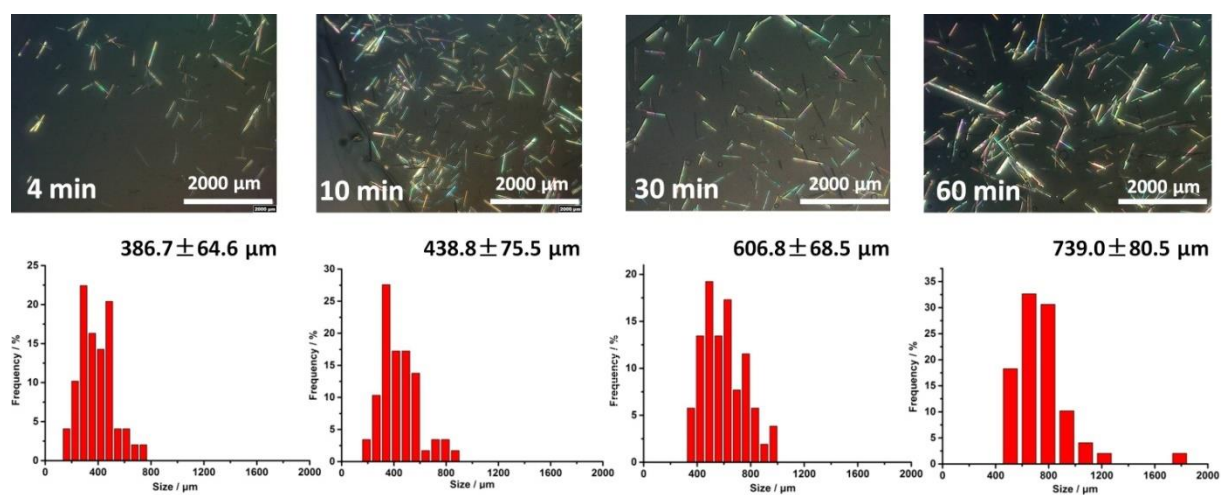
Figure S14 ｜ Time-dependent growth of the TA single crystals by mixing the TA containing DMF and PIL-1 containing DMF under stirring speed of 400 rpm.
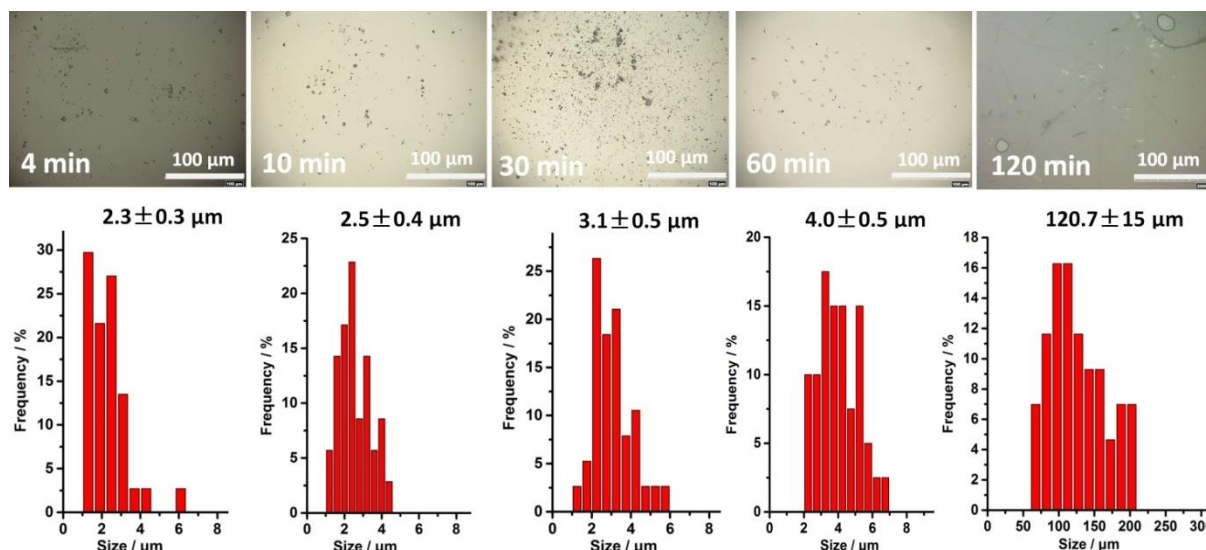
Figure S15 │ Time dependent growth of the TA single crystals by mixing the TA containing DMF and PIL-1 containing DMF without stirring.
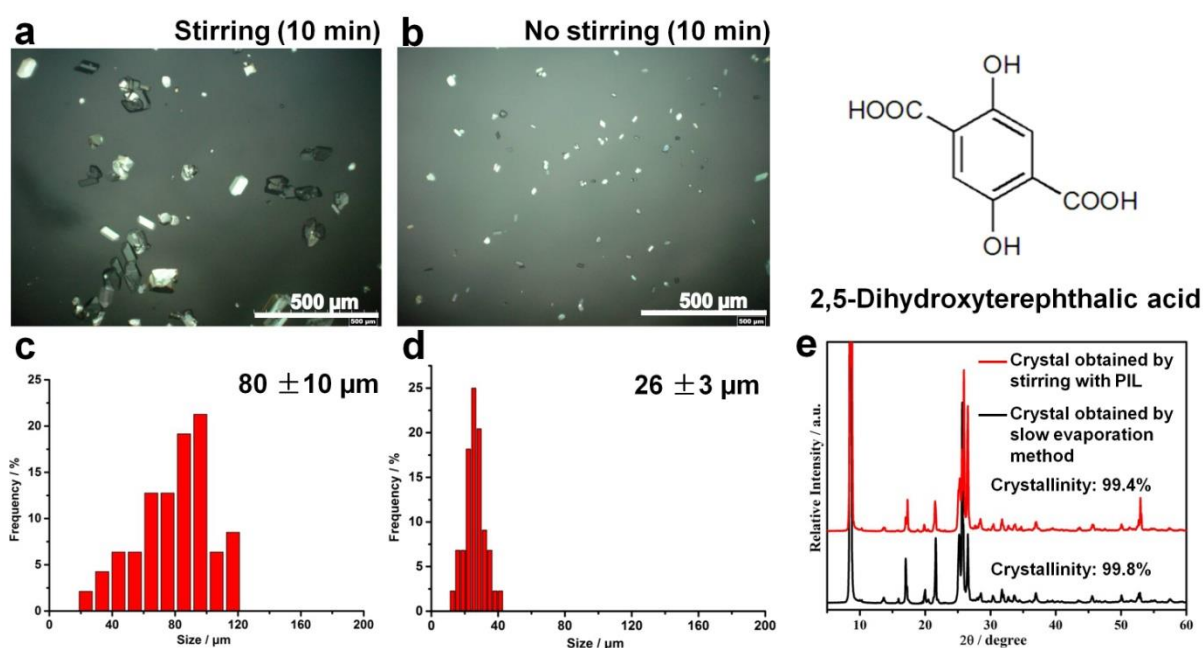
Figure S16 │ Comparison of crystallization of 2,5-Dihydroxyterephthalic acid with stirring vs. no stirring in the presence of PIL-1. Images of crystals and corresponding size distributions of 2,5-Dihydroxyterephthalic acid under stirring (**a, c**) and no stirring (**b, d**) for 10 min. **e**, PXRD patterns of crystals obtained with stirring (red) and the ones obtained by slow evaporation of 2,5-Dihydroxyterephthalic acid solution in DMF (black).
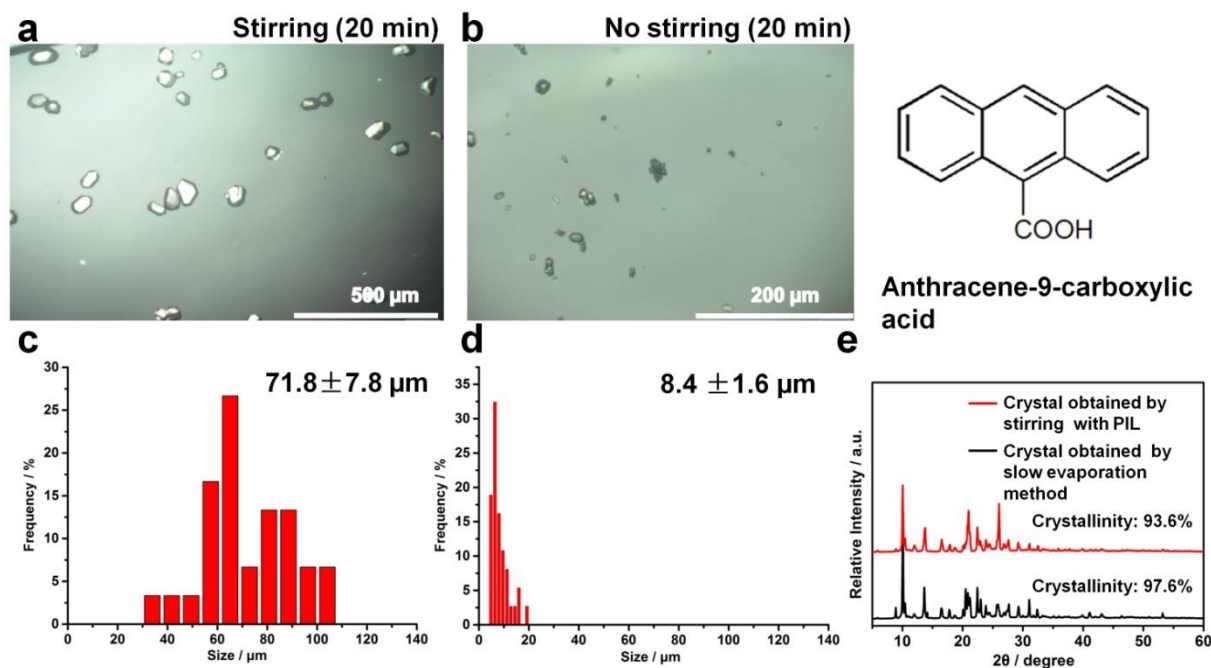
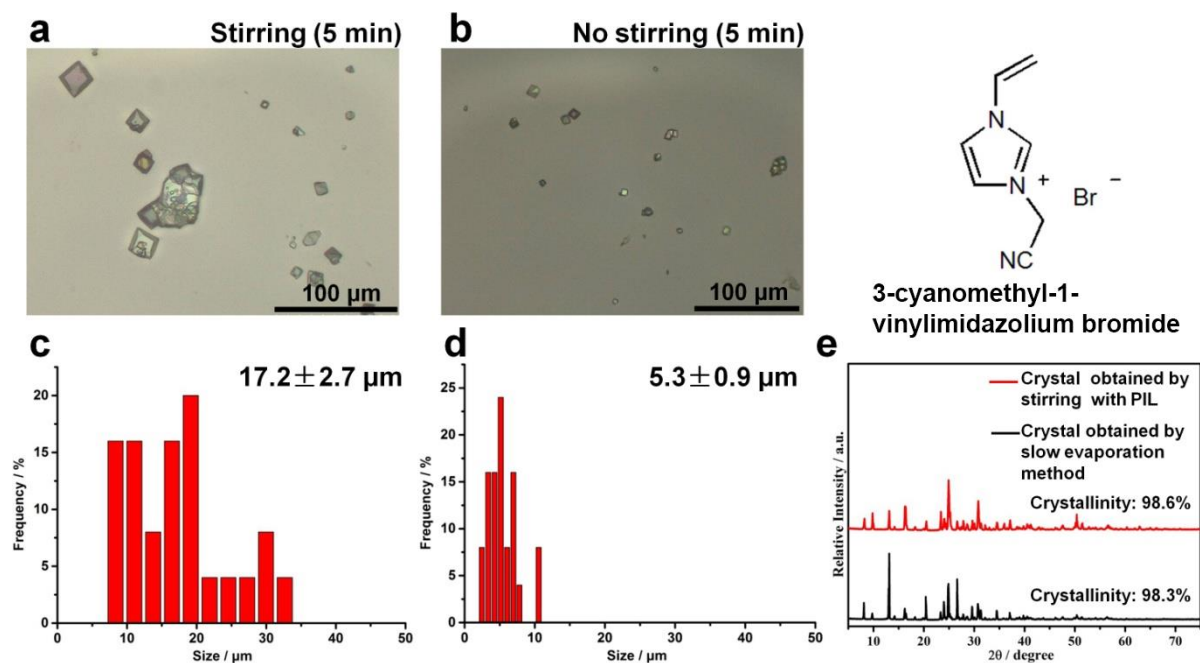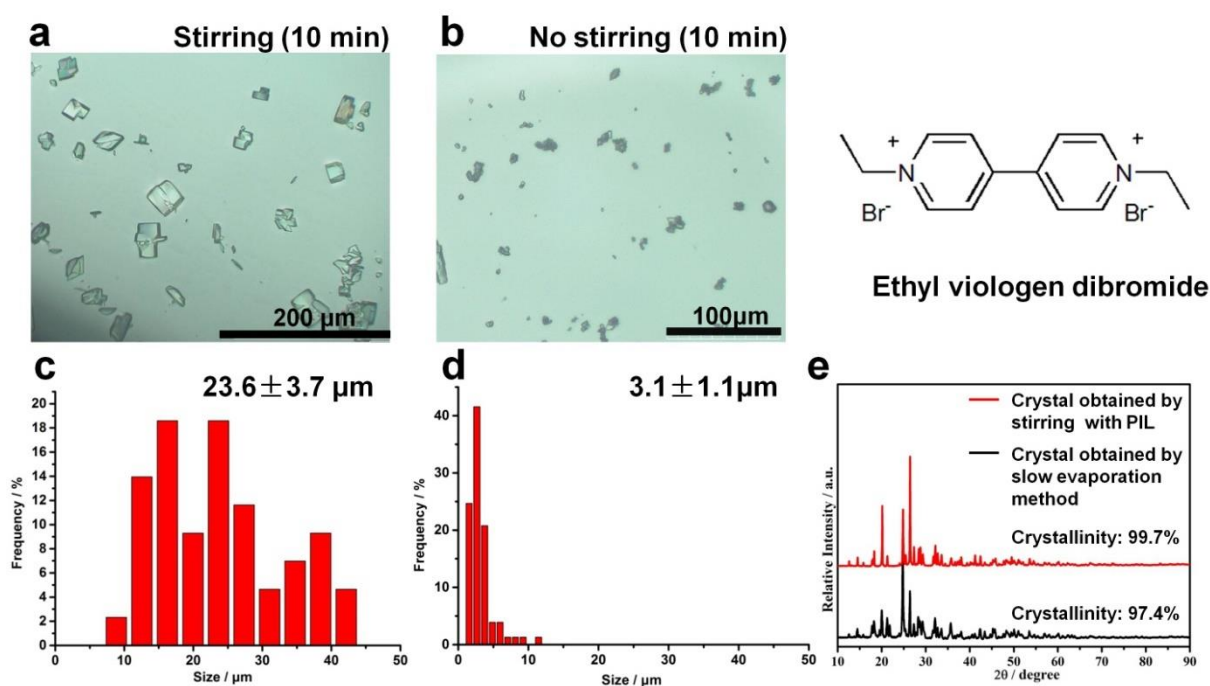**Figure S17** │ Comparison of crystallization of Anthracene-9-carboxylic acid with stirring vs. no stirring in the presence of PIL-1. Images of crystals and corresponding size distributions of Anthracene-9-carboxylic acid under stirring (**a, c**) and without stirring (**b, d**) for 20 min. **e**, PXRD patterns of crystals obtained under stirring (red) and the ones obtained by slow evaporation of Anthracene-9-carboxylic acid solution in DMF (black).

Figure S18 │ Comparison of crystallization of 3-cyanomethyl-1-vinylimidazolium bromide with stirring vs. no stirring in the presence of PIL-6. Images of crystals and corresponding size distributions of 3-cyanomethyl-1-vinylimidazolium bromide under stirring (**a, c**) and without stirring (**b, d**) for 5 min. **e**, PXRD patterns of crystals obtained under stirring (red) and the ones obtained by slow evaporation of the solution of 3-cyanomethyl-1-vinylimidazolium bromide in methanol (black).
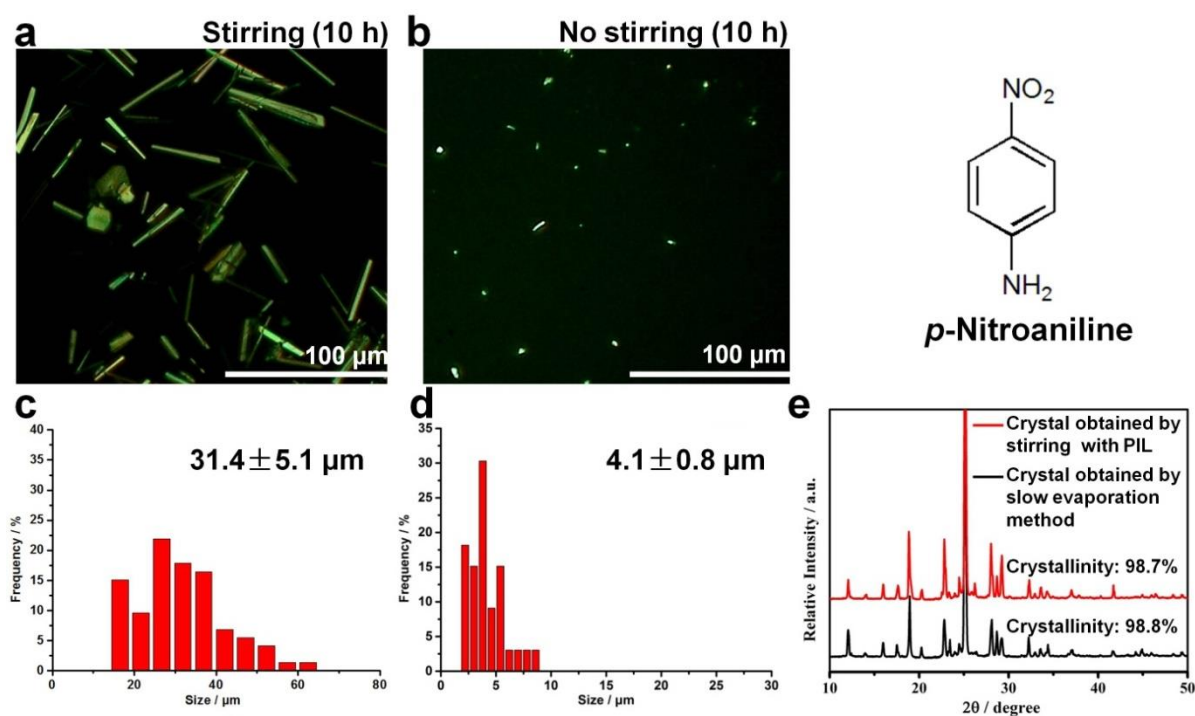
Figure S19 │ Comparison of crystallization of Ethyl viologen with stirring vs. no stirring in the presence of PIL-6. Images of crystals and corresponding size distributions of Ethyl viologen under stirring (**a, c**) and without stirring (**b, d**) for 10 min. **e**, PXRD patterns of crystals obtained under stirring (red) and the ones obtained by slow evaporation of the solution of Ethyl viologen in methanol (black).

Figure S20 │ Comparison of crystallization of *p*-Nitroaniline with stirring vs. no stirring in the presence of PIL-1. Images of crystals and corresponding size distributions of *p*-Nitroaniline under stirring (**a, c**) and without stirring (**b, d**) for 10 h. **e**, PXRD patterns of crystals obtained

22

under stirring (red) and the ones obtained by slow evaporation of the solution of *p*-Nitroaniline in DMF (black).
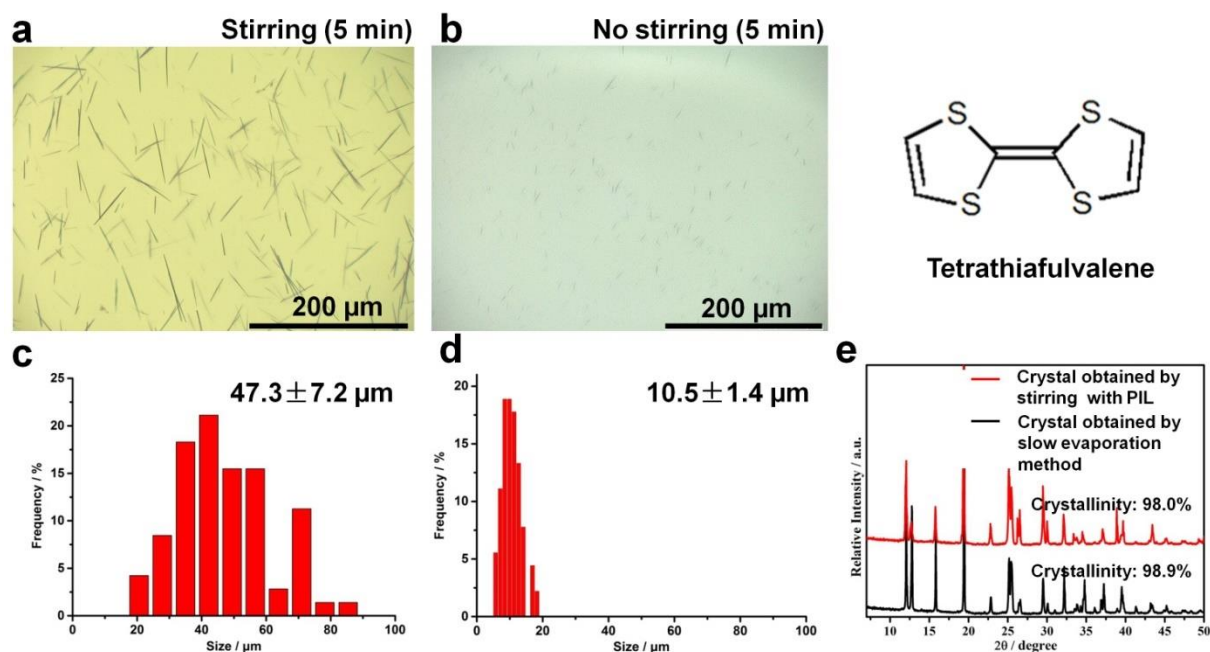

Figure S21 │ Comparison of crystallization of Tetrathiafulvalene with stirring vs. no stirring in the presence of PIL-3. Images of crystals and corresponding size distributions of Tetrathiafulvalene under stirring (**a, c**) and without stirring (**b, d**) for 5 min. **e**, PXRD patterns of crystals obtained under stirring (red) and the ones obtained by slow evaporation of the solution of Tetrathiafulvalene in DCM-MeOH mixture (black).

Figure S22 │ Comparison of crystallization of 1,2,4,5-Tetrakis(4-carboxyphenyl)benzene with stirring vs. no stirring in the presence of PIL-7. Images of crystals and corresponding size

distributions of 1,2,4,5-Tetrakis(4-carboxyphenyl)benzene under stirring (**a, c**) and without stirring (**b, d**) for 2 h. **e**, PXRD patterns of crystals obtained under stirring (red) and the ones obtained by slow evaporation of the solution of 1,2,4,5-Tetrakis(4-carboxyphenyl)benzene in DMF (black).

Figure S23 │ Comparison of crystallization of Meso-tetra (carboxyphenyl) porphyrin with stirring vs. no stirring in the presence of PIL-1. Images of crystals and corresponding size distributions of Meso-tetra (carboxyphenyl) porphyrin under stirring (**a, c**) and without stirring (**b, d**) for 10 min. **e**, PXRD patterns of crystals obtained under stirring (red) and the ones obtained by slow evaporation of the solution of Meso-tetra (carboxyphenyl) porphyrin in DMF (black).
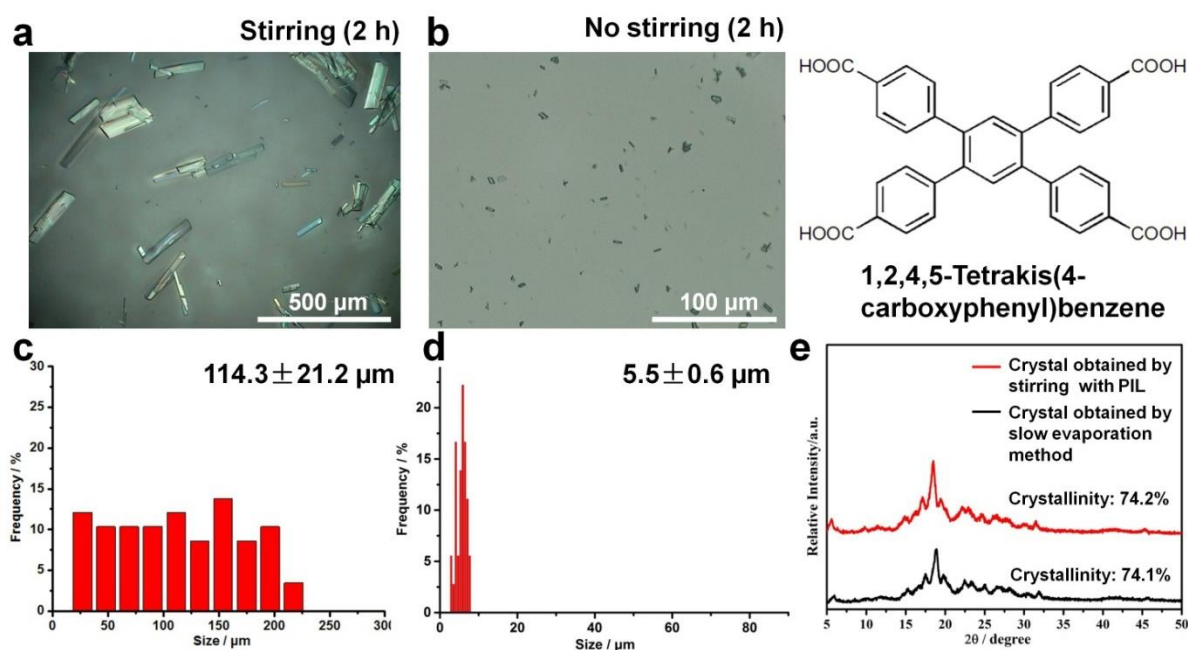
Figure S24 │ Comparison of crystallization of *β*-Cyclodextrin with stirring vs. no stirring in the presence of PIL-1. Images of crystals and corresponding size distributions of *β*-Cyclodextrin under stirring (**a, c**) and without stirring (**b, d**) for 10 h. **e**, PXRD patterns of crystals obtained under stirring (red) and the ones obtained by slow evaporation of the solution of *β*-Cyclodextrin in DMF (black).
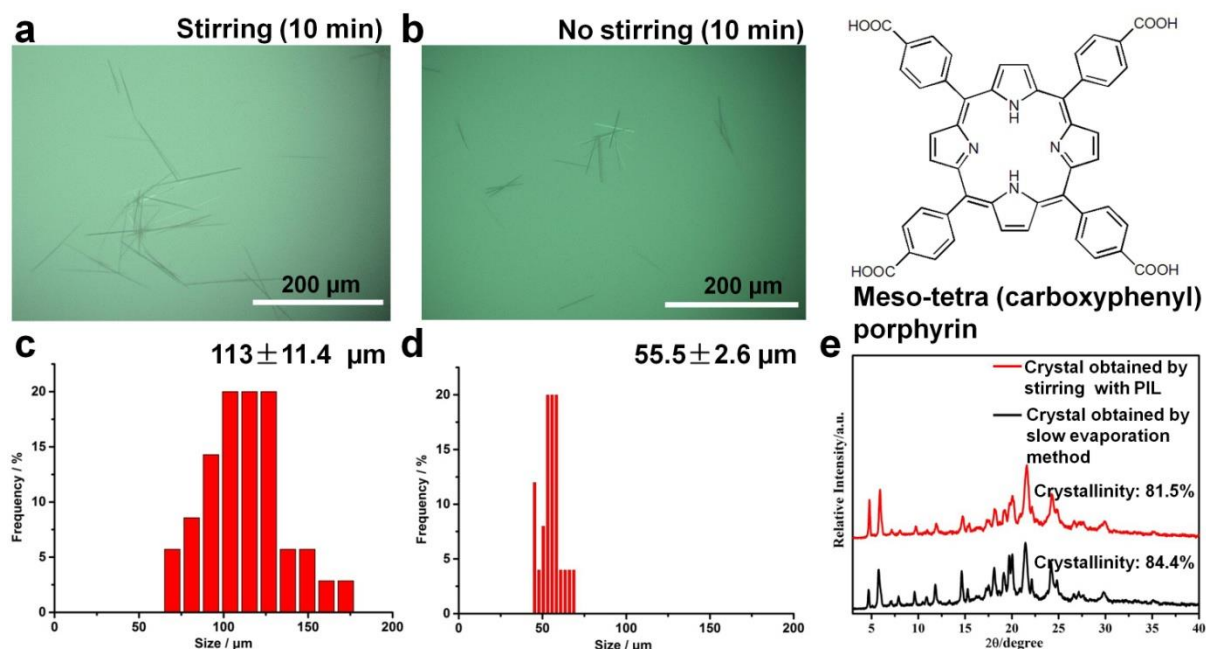

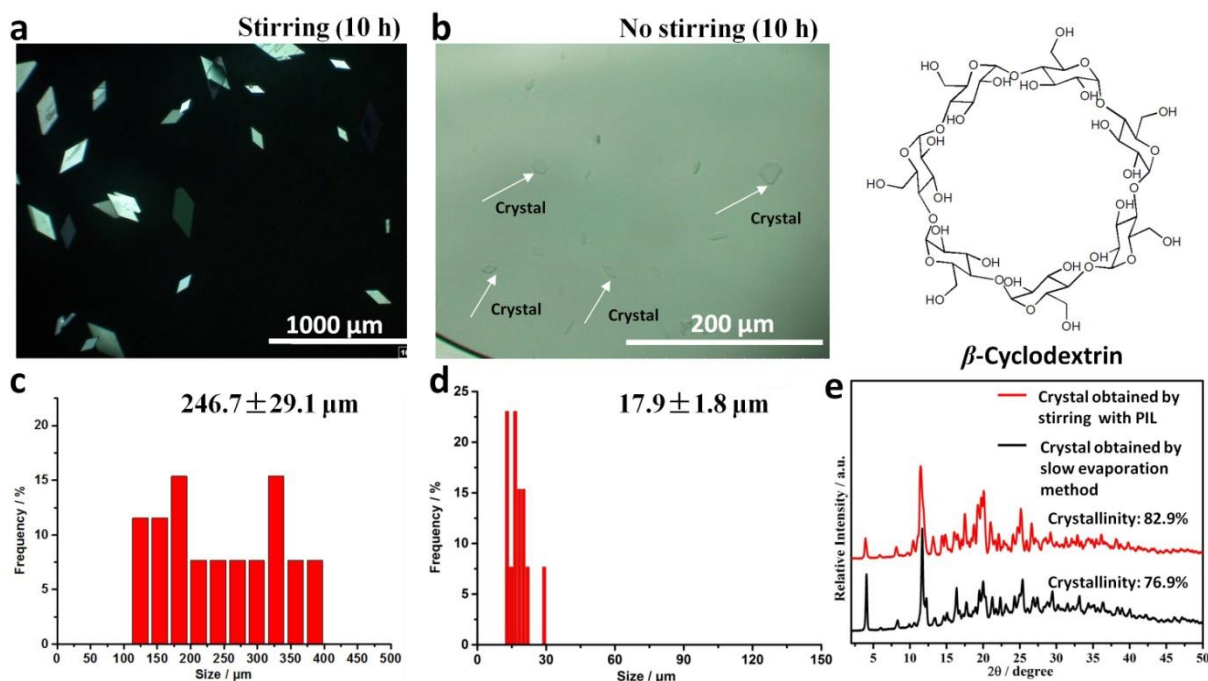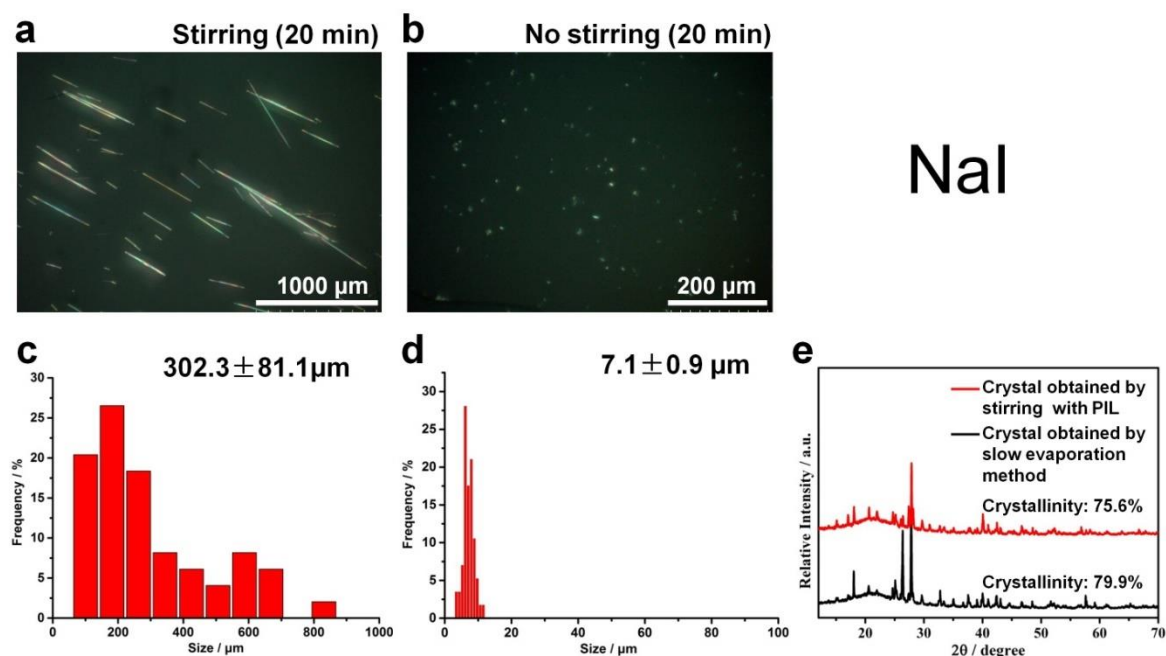**Figure S25** │ Comparison of crystallization of NaI with stirring vs. no stirring in the presence of PIL-3. Images of crystals and corresponding size distributions of NaI under stirring (**a, c**) and without stirring (**b, d**) for 20 min. **e**, PXRD patterns of crystals obtained under stirring (red) and the ones obtained by slow evaporation of the solution of NaI in DMF (black).
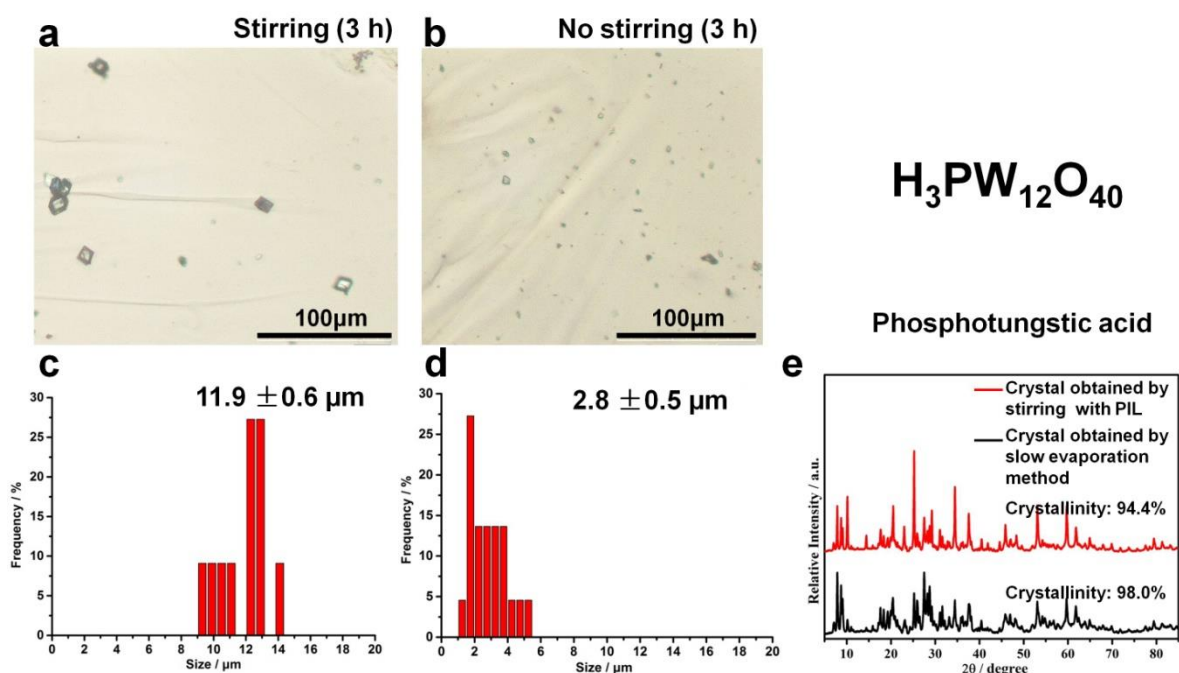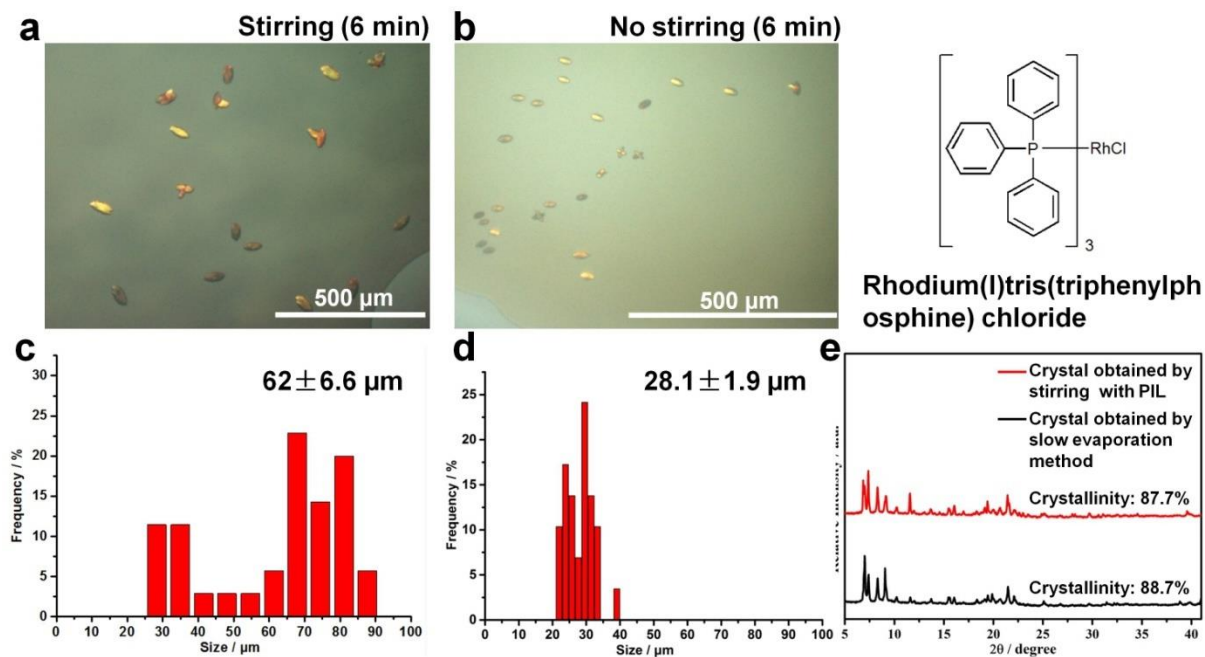
Figure S26 │ Comparison of crystallization of Phosphotungstic acid with stirring vs. no stirring in the presence of PIL-5. Images of crystals and corresponding size distributions of Phosphotungstic acid under stirring (**a, c**) and without stirring (**b, d**) for 3h. **e**, PXRD patterns of crystals obtained under stirring (red) and the ones obtained by slow evaporation of the solution of Phosphotungstic acid in water (black).

Figure S27 │ Comparison of crystallization of Rhodium(I) tris(triphenylphosphine) chloride with stirring vs. no stirring in the presence of PIL-3. Images of crystals and corresponding size distributions of Rhodium(I) tris(triphenylphosphine) chloride under stirring (**a, c**) and without stirring (**b, d**) for 6 min. **e**, PXRD patterns of crystals obtained under stirring (red) and the ones obtained by slow evaporation of the solution of Rhodium(I) tris(triphenylphosphine) chloride in DCM (black).

Figure S28 │ Comparison of crystallization of Iron(III) meso-tetraphenylporphine chloride with stirring vs. no stirring in the presence of PIL-6. Images of crystals and corresponding size distributions of Iron(III) meso-tetraphenylporphine chloride under stirring (**a, c**) and without stirring (**b, d**) for 3 min. **e**, PXRD patterns of crystals obtained under stirring (red) and the ones obtained by slow evaporation of the solution of Iron(III) meso-tetraphenylporphine chloride in DCM (black).

Figure S29 │ Comparison of crystallization of Hen egg white lysozyme with stirring vs. no stirring in the presence of PIL-5. Images of crystals and corresponding size distributions of Hen egg white lysozyme under stirring (**a, c**) and without stirring (**b, d**) for 2 h. **e**, UV-vis spectra of

crystals obtained under stirring (red) and the commercial Hen egg white lysozyme (black) match each other well, exhibiting absorption different from that of PIL-5 (blue). For these measurements, all samples/crystals were dissolved in deionised water.
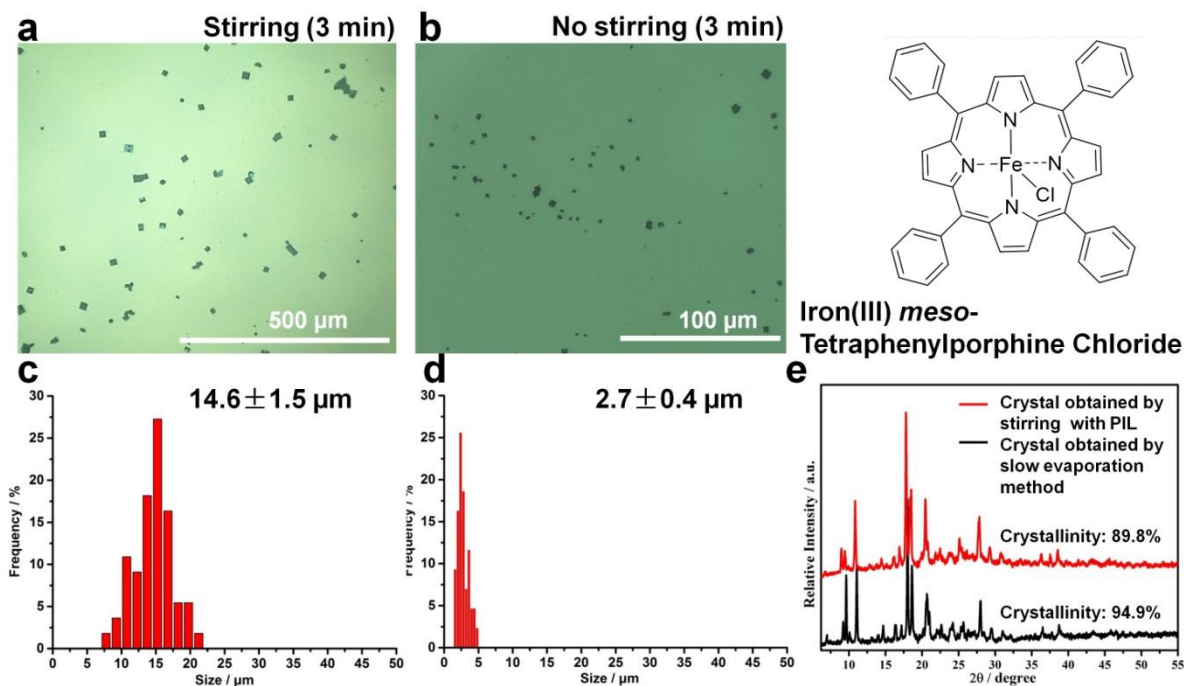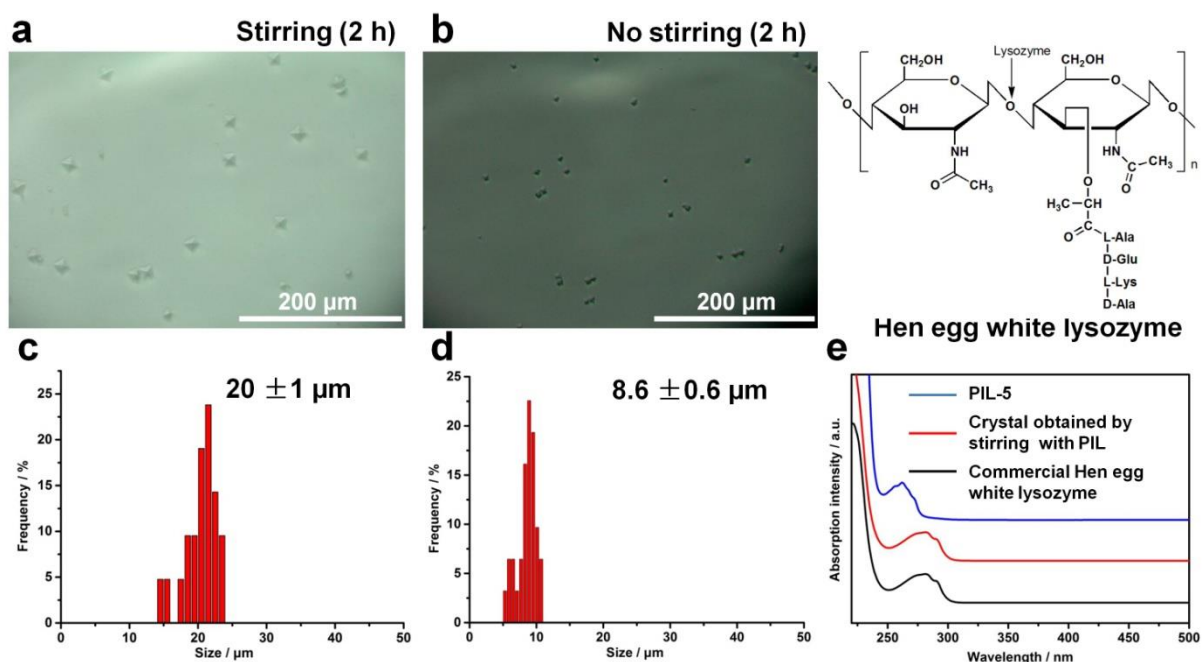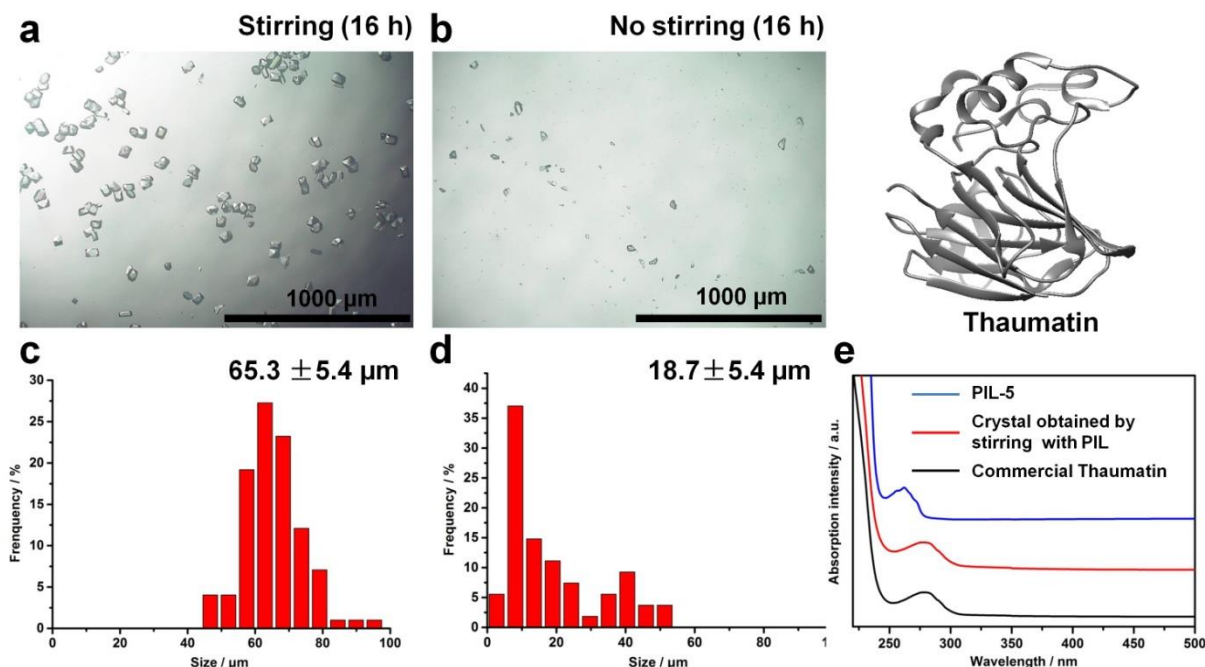

Figure S30 │ Comparison of crystallization of Thaumatin with stirring vs. no stirring in the presence of PIL-5. Images of crystals and corresponding size distributions of Thaumatin under stirring (**a, c**) and without stirring (**b, d**) for 16 h. **e**, UV-vis spectra of crystals obtained under stirring (red) and the commercial Thaumatin (black) match each other well, exhibiting absorption different from that of PIL-5 (blue). For these measurements, all samples/crystals were dissolved in deionised water.

Figure S31 │ Comparison of crystallization of CC3-R with stirring vs. no stirring in the presence of PIL-3. Images of crystals and corresponding size distributions of CC3-R under stirring (**a, c**) and without stirring (**b, d**) for 10 min. **e**, PXRD pattern of crystals obtained by us under stirring (red) and the one synthesized following a literature procedure[S6] (black).
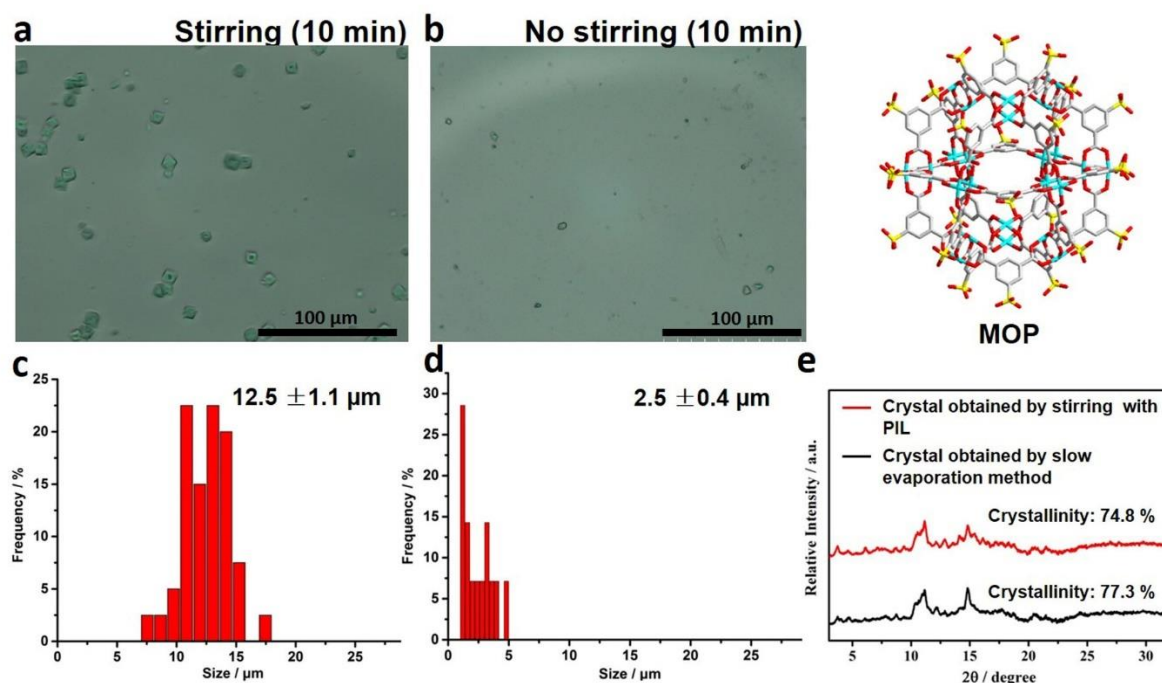
Figure S32 │ Comparison of crystallization of MOP with stirring vs. no stirring in the presence of PIL-5. Images of crystals and corresponding size distributions of MOP under stirring (**a, c**) and without stirring (**b, d**) for 10 min. **e**, PXRD pattern of crystals obtained under stirring (red) and via slow evaporation of the MOP's methanolic solution.
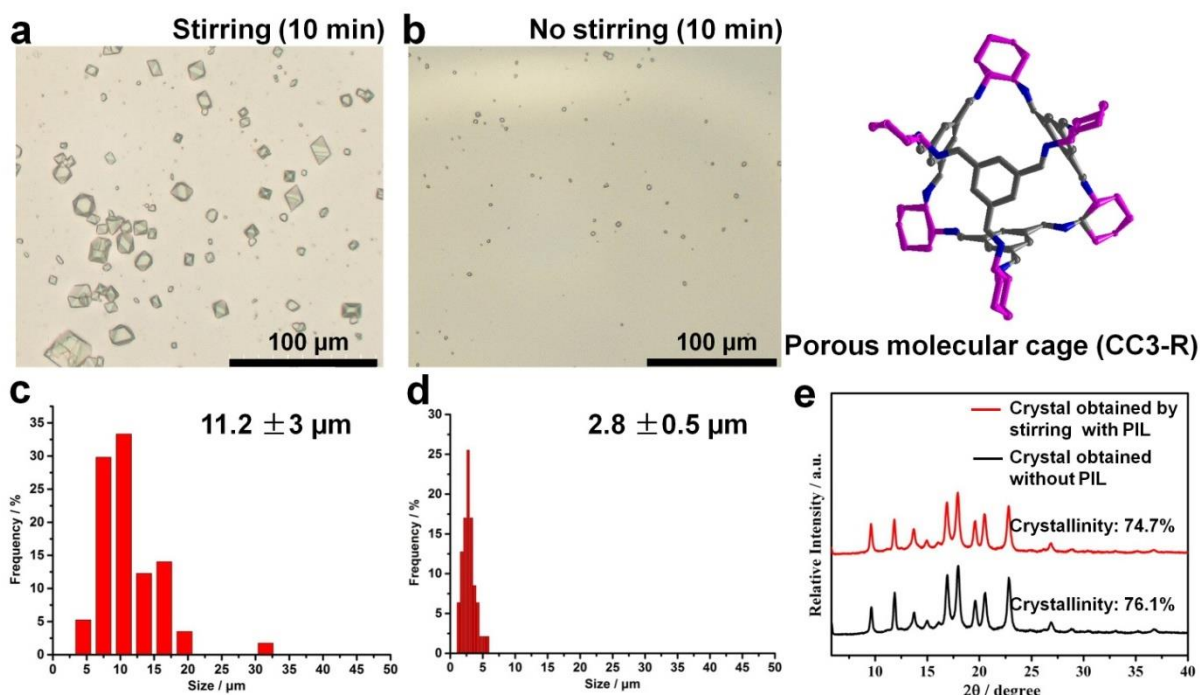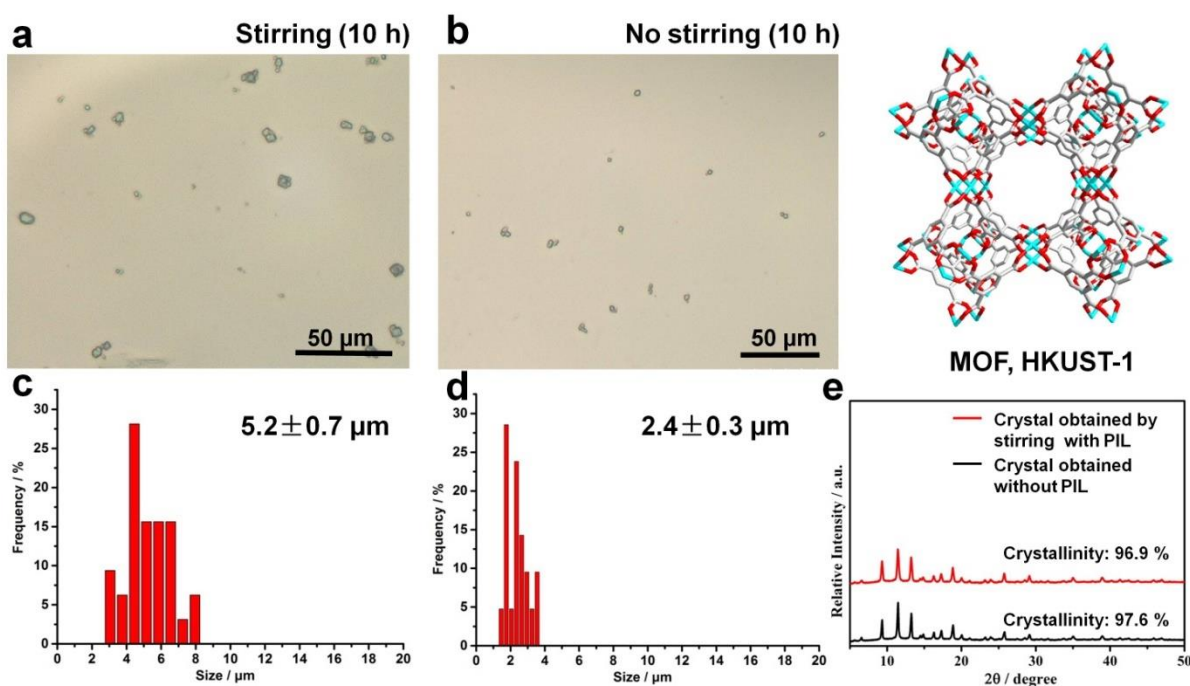
Figure S33 │ Comparison of crystallization of HKUST-1 MOF with stirring vs. no stirring in the presence of PIL-4. Images of crystals and corresponding size distributions of HKUST-1 MOF under stirring (**a, c**) and without stirring (**b, d**) for 10 h. **e**, PXRD pattern of crystals obtained under stirring (red) and the one synthesized following a literature procedure[S7] (black).
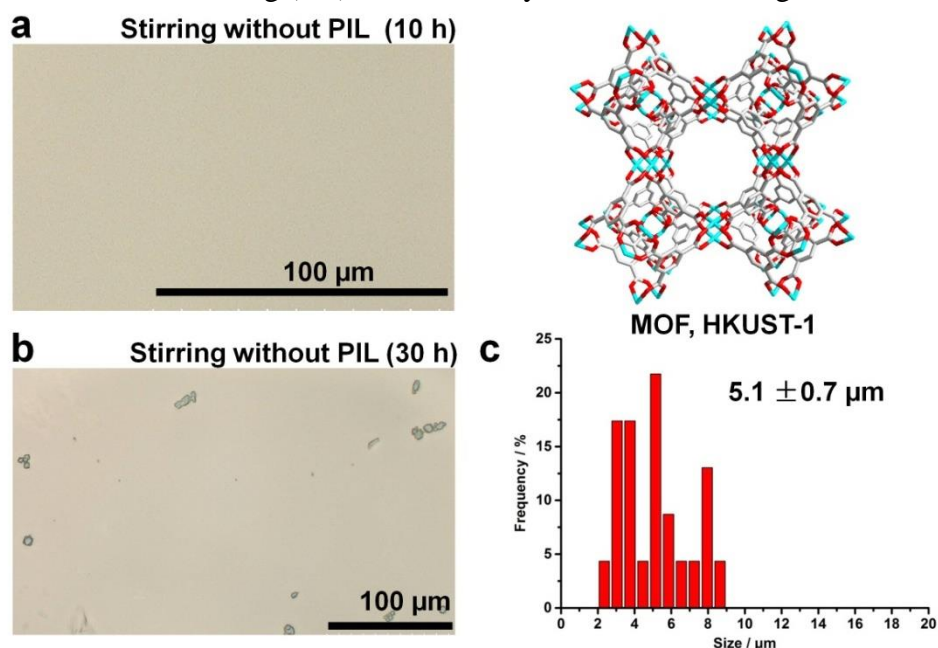
Figure S34 │ The synthesis of the HKUST-1 by stirring same concentrated TA and $Cu(NO_3)_2 \cdot 3H_2O$ raw materials in DMF solution but without PIL-4. **a**, The solution was taken out for recording after stirring for 10 h, no crystals could be obtained. Single crystals (**b**) and corresponding size distribution (**c**) of HKUST-1 under stirring for 30 h.
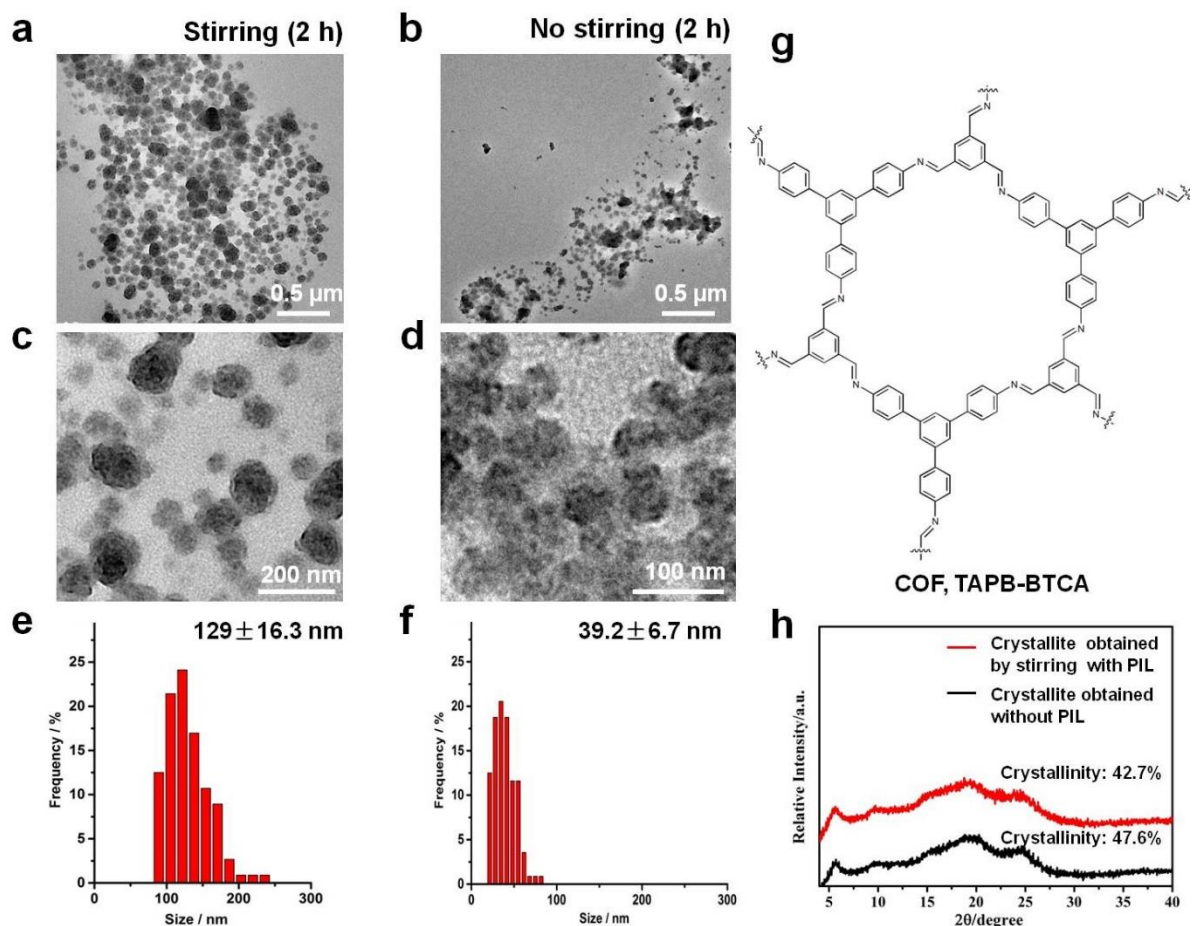
Figure S35 │ Comparison of crystallization of a covalent organic network (COF, TAPB-BTCA[S8]) under stirring vs. no-stirring in the presence of PIL-1. TEM images of crystallites and corresponding size distributions of TAPB-BTCA COF under stirring (**a, c, e**) and without stirring (**b, d, f**) for 2 h. The formation of COF colloidal crystallites has also been reported in literature.[S9] **h**, The PXRD pattern of the crystal obtained by our current stirring method (red) and the one synthesized following a literature procedure.

a Stirring without PIL (15 min)

50 μm

b Stirring without PIL (3 h)

250 nm

0.5 μm

COF, TAPB-BTCA

c 92.6±14.4 nm
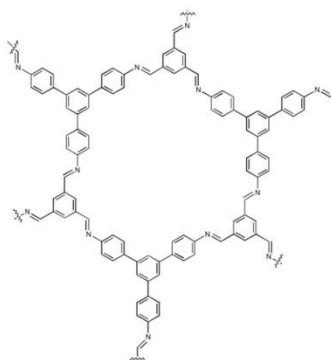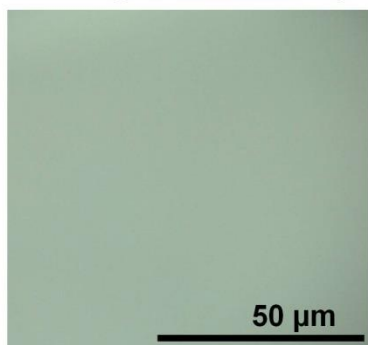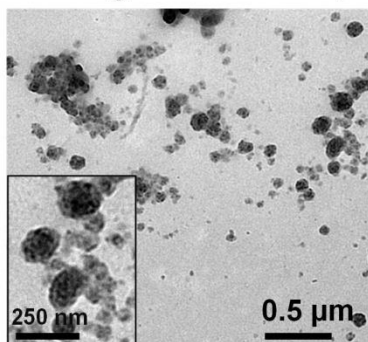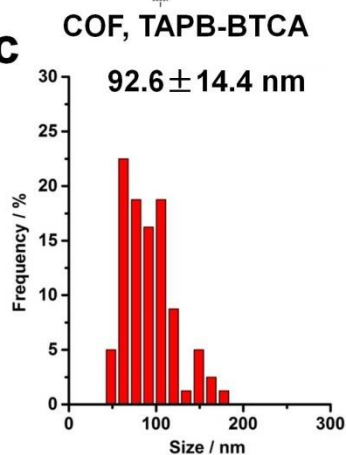
Figure S36 │ The synthesis of TAPB-BTCA COF by stirring the same concentrated TAPB and BTCA precursors in DMSO but without PIL-1. **a**, The solution was taken out for recording after stirring for 15 min, no crystallites could be obtained. TEM image of crystallites (**b,** inset is high magnification) and corresponding size distribution (**c**) of TAPB-BTCA COF under stirring for 3 h.
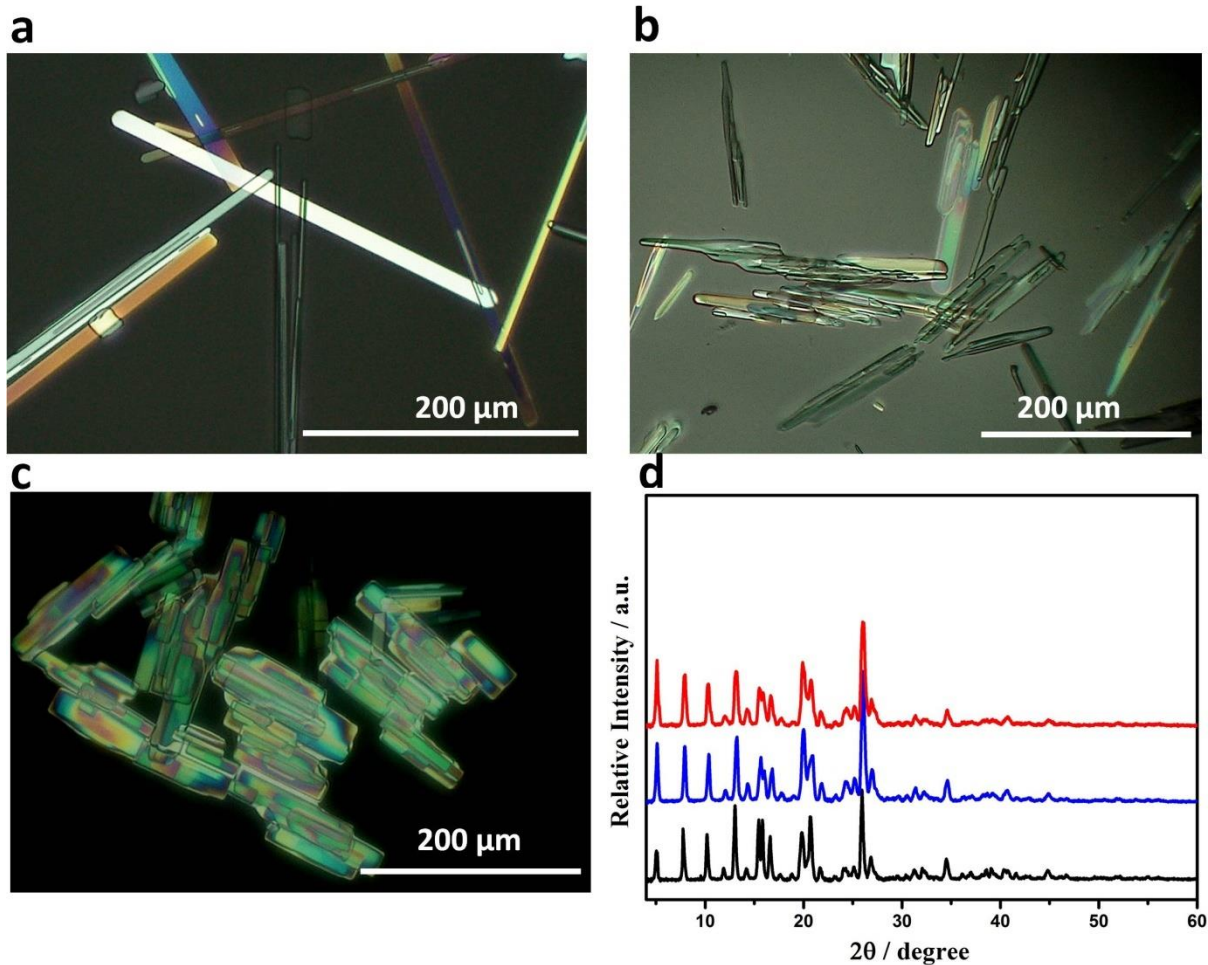
Figure S37 │ Growing TA crystals in solutions containing different PILs can alter crystal morphology, Crystals obtained in sheared DMF solutions containing. **a**, PIL-1; **b**, PIL-2; **c**, PIL-7. **d,** PXRD patterns of the TA crystals grown under these three conditions are not altered (black curve: PIL-1, blue curve: PIL-2, red curve: PIL-7).
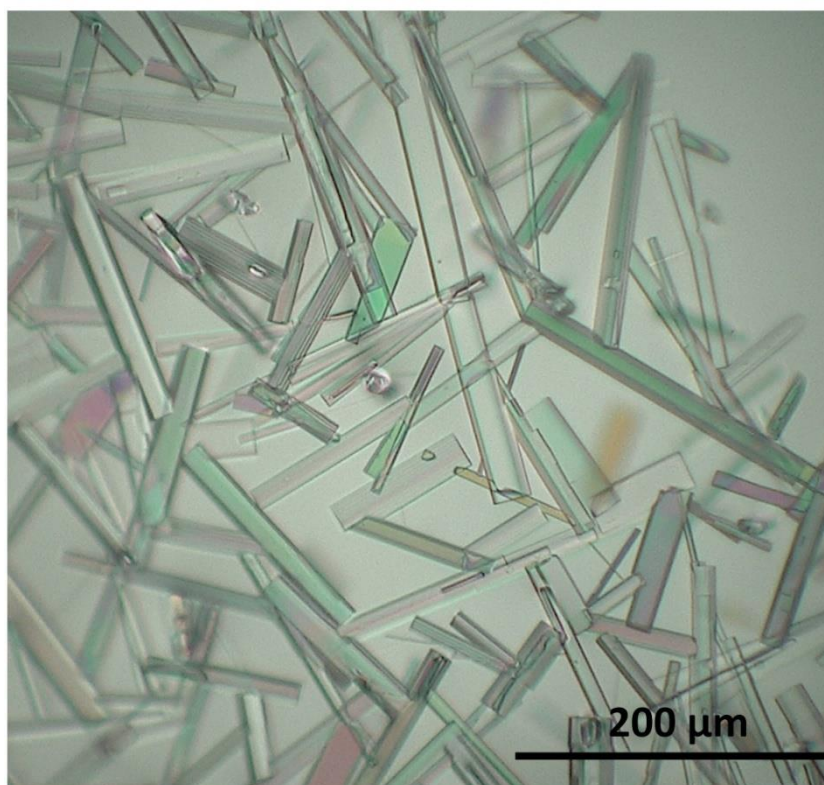
Figure S38 ｜ Crystals of TA grown by slow evaporation from DMF solution at room temperature for more than one week.
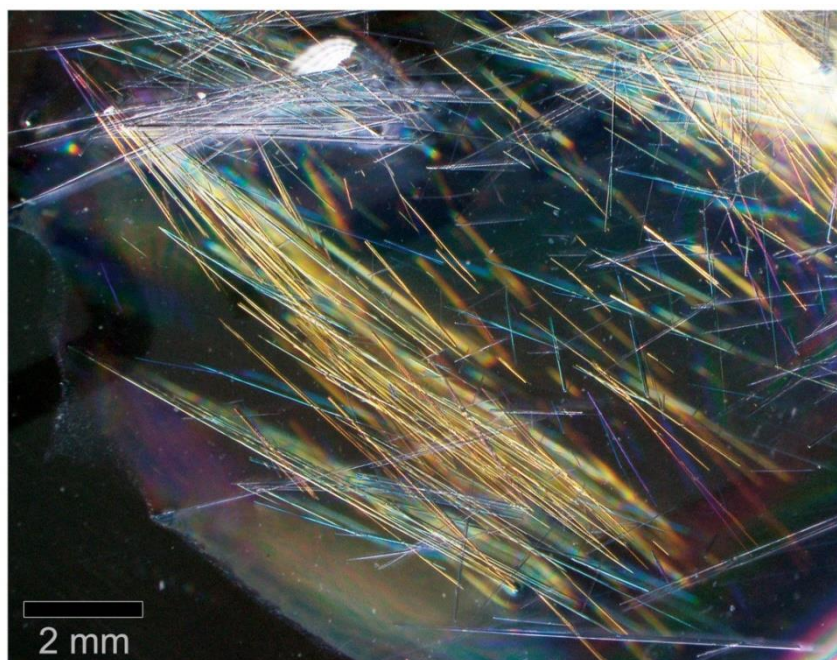
Figure S39 ｜ The TA single crystals grown under stirring for 7 days but in a larger Couette cell (gap between inner and outer cylinders: 8.7 mm).
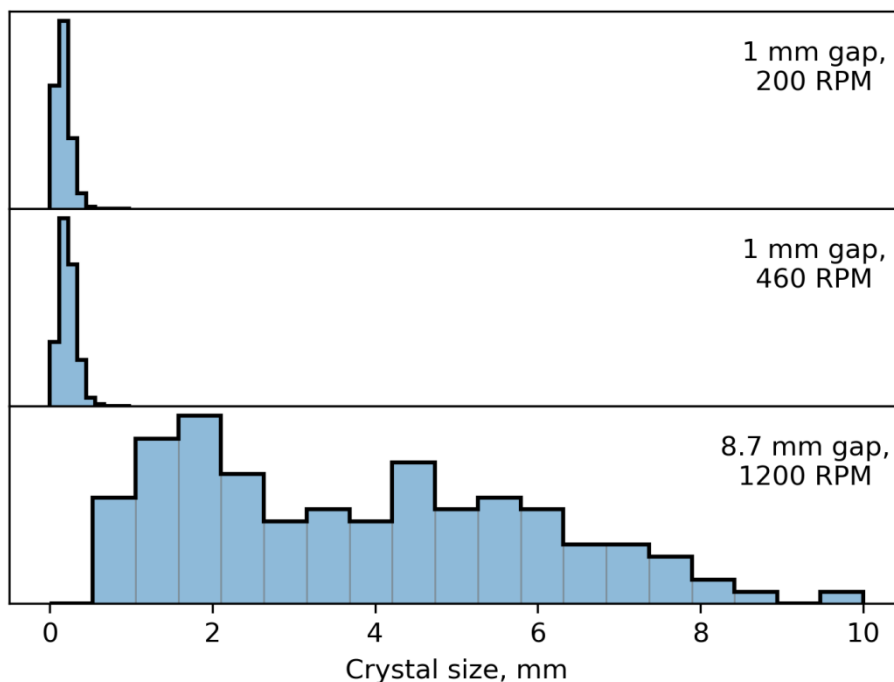
Figure S40 ｜ Size histograms of TA crystals grown in PIL-1/DMF using comparable shear rates but different Couette cells. Large cell: inner wall radius 4 mm, outer wall radius 12.7 mm, rotation speed 1200 rpm. Small cell: inner wall radius 4 mm, outer wall radius 5 mm, rotation speed either 200 rpm or 460 rpm (shear rates and choice of rotational speeds here is discussed below, in **Section 4.4**). Larger gap between the walls of the Couette cell results in larger crystals under similar shear rates. Growth time is 7 days.

2.4. Surface areas of porous functional materials grown in the presence of PIL's under shear as compared to results of a conventional method

The N_2 sorption isotherms were measured with BELSORP-max automatic volumetric adsorption equipment at liquid nitrogen temperature (77 K).

Pore activation of CC3-R Cage and TAPB-BTCA COF before gas adsorption experiments was performed as follows. The CC3R cage and TAPB-BTCA COF crystals were grinded. The crystals were soaked in methanol for 2 days and exchanged by fresh methanol. Before adsorption measurement, additional activation at 100 $^\circ$C for 6 hours was performed to remove all solvents from the samples.

Pore activation of HKUST-1 before gas adsorption experiments was performed as follows. The HKUST-1 crystals were grinded. Crystals were soaked in DMF/methanol (volume ratio = 1:1) for 2 days and exchanged by fresh solvent. Then, the HKUST-1 was isolated by centrifugation and further soaked in acetone for 2 days. Before adsorption measurement, additional activation at 150 $^\circ$C for 6 h was performed to remove all solvents from the samples.

Note: Improvement of BET surface area for CC3-R (**Figure S41c**) can be related to previously reported[S10] inverse relationship between crystallinity and BET surface area for CC3-R grown with different rates of crystallization (592 m^2/g for 77% crystallinity, 409 $\pm$ 8 m^2/g for crystallinity 93%). Note that crystallinity of CC3-R grown with PIL under shear is 74.7%, and BET surface area is 676 m^2/g. In contrast, Zhu *et. al.*[S11] reported that when missing-linker-type molecular defects were installed into CC3-R via nonsolvent-induced crystallization, it caused a decrease of BET surface area for N_2, but increase of absorption of CO_2. This indicates that BET surface area can change in both directions, depending on the way the defects are introduced during the crystal growth.
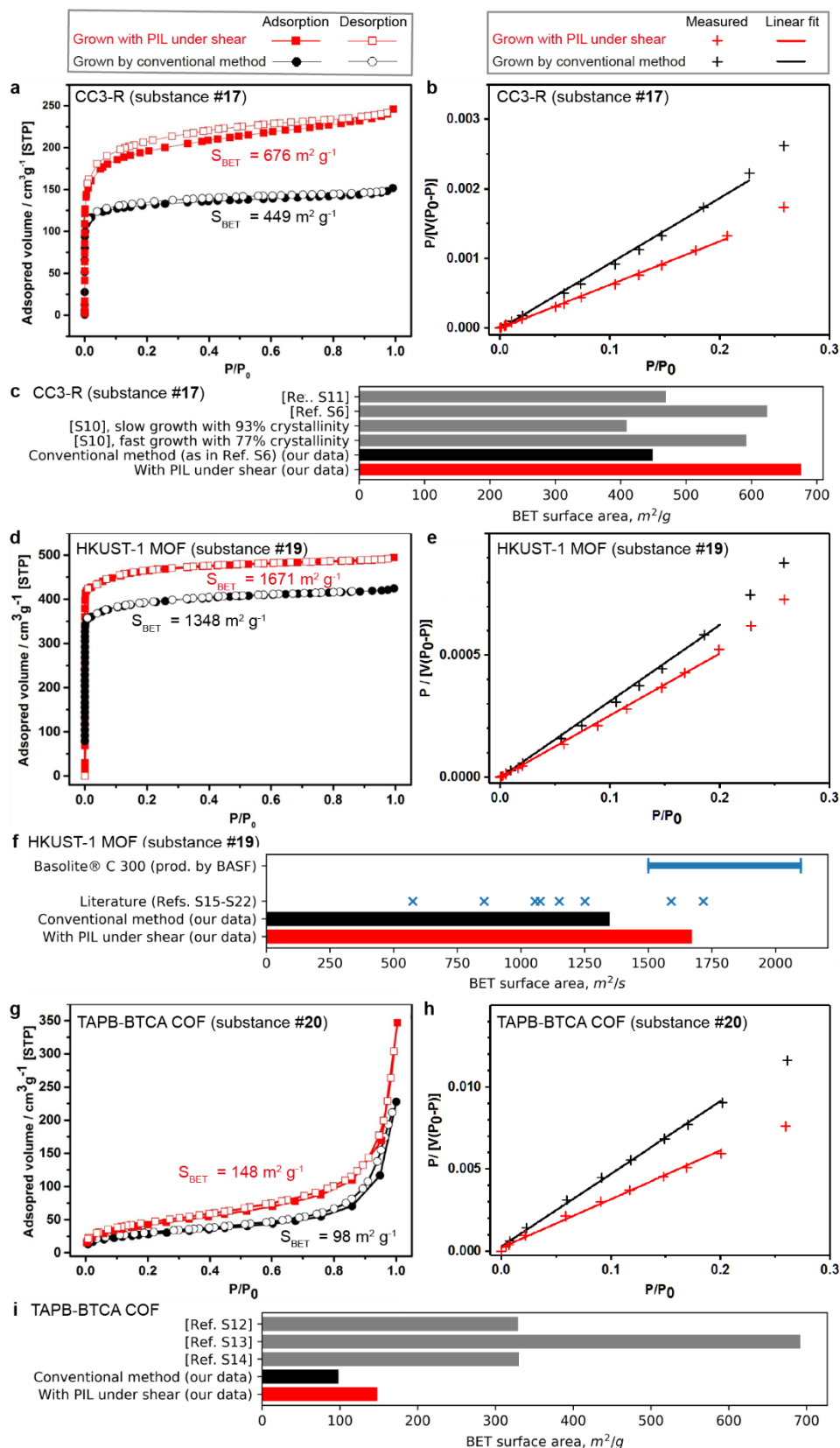
Figure S41 | Surface areas of functional porous materials grown in the presence of PIL's under shear (*red*) and of those grown by conventional methods, with no PIL (*black*, also see Figures S32,S34). a,d,g) N$_2$ adsorption (*filled markers*) and desorption (*empty markers*) isotherms. **b,e,h**) Linear BET curve fits (*solid lines*) used for evaluating BET surface areas. Fitting was

performed for measured data points (*crosses*) in the range $P/P_0 < 0.25$ for CC3-R (**b**), and in the range $P/P_0 < 0.2$ for both HKUST-1 MOF (**e**) and TAPB-BTCA COF (**f**). Graphs **c,f,i**) compare literature values (*grey* or *blue*) to our data for conventional method (*black*) and for growing crystals in the presence of PIL's and under shear (*red*). Using PIL and shear resulted in BET surface area increasing by 51% for CC3-R (676 m^2 g^{-1} vs. 449 m^2 g^{-1}, **c**), by 24% for HKUST-1 MOF (1671 m^2 g^{-1} vs. 1348 m^2 g^{-1}, **f**), and by 51% for TAPB-BTCA COF (148 m^2 g^{-1} vs. 98 m^2 g^{-1}, **i**) with respect to crystals grown conventionally but treated identically after growth.

Section 3. Dynamic light scattering measurements.

DLS measurements of the hydrodynamic radius of PIL-1 (MW 402 kg/mol) in DMF were performed on a Malvern ZetaSizer Nano instrument. Results show that PIL-1 slowly dissolved in DMF (300 mg / 0.35 mL; further diluted to 5 nM concentration for DLS measurements) exists as large clumps ca. 600 nm in diameter (**Figure S42a**, grey distributions). When sonicated, 5 nM solution of PIL-1 in DMF shows typical sizes ca. 12 nm (**Figure S42b**), and therefore the hydrodynamic radii of 6 nm. Since radius of gyration for polymers in solution is usually roughly 0.7 of the hydrodynamic radius[S23], we estimate that radius of gyration is approximately 4 nm.

We subjected PIL-1/DMF solution to shear ($\dot{\gamma} = 167\ s^{-1}$) for 3 hours. We first slowly dissolved 300 mg of PIL-1 in 0.35 mL of DMF (without stirring), then diluted it to 5 nM concentration of PIL-1 immediately before DLS measurements. These measurements showed that the number distribution of sizes had initially shifted to ca. 35 nm (**Figure S42a**, dark blue), and then slowly drifted to larger sizes as we took measurements every 3 minutes (**Figure S42a**, colored distributions). This indicates that polymer entanglement, unfolding, or both happened under shear flow.
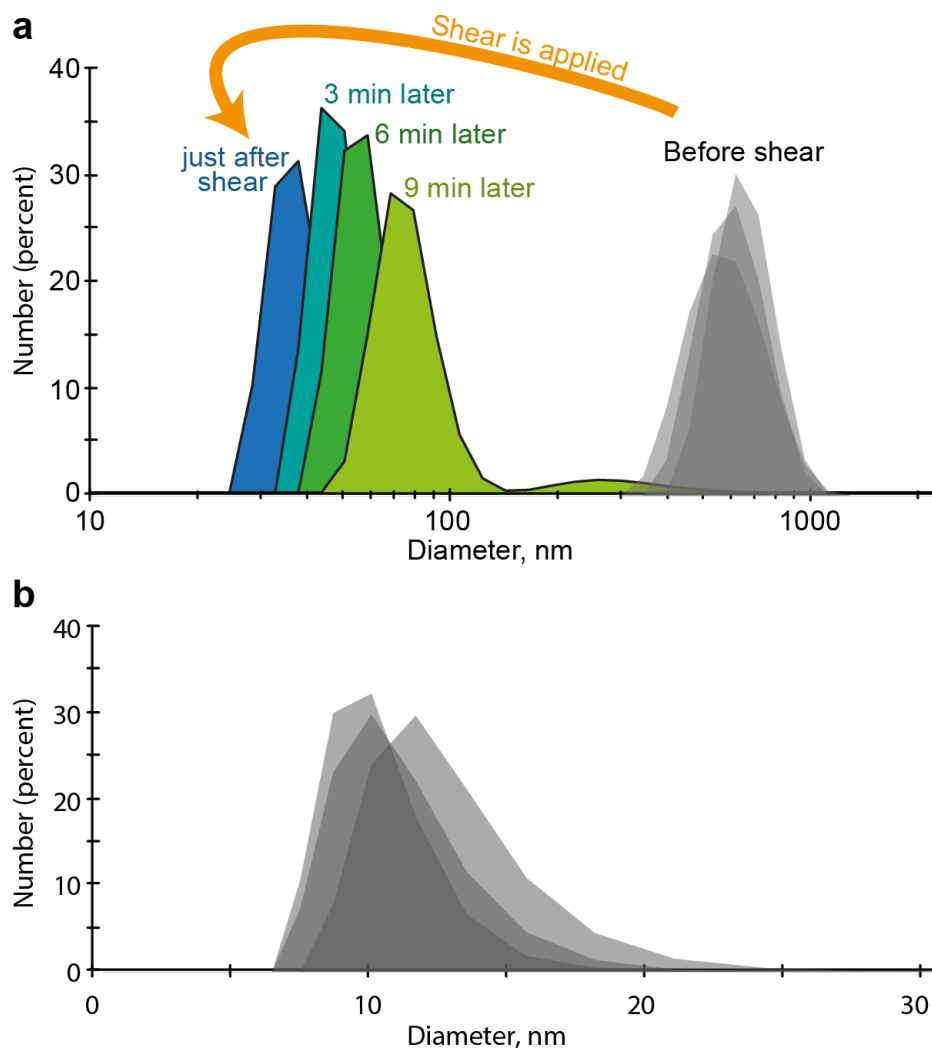
Figure S42. Number distribution by size obtained from dynamic light scattering measurements. **a**. Three superimposed grey distributions on the right correspond to solution of PIL-1 (402 kg/mol) in DMF obtained by first slowly dissolving 300 mg of PIL-1 in 0.35 mL of DMF (without stirring), then diluting it to 5 nM concentration of PIL-1 immediately before DLS measurements. Alternatively, solution of 300 mg of PIL-1 in 0.35 mL of DMF was kept in shear flow (167 s^{-1}) for 3 hours, then diluted to 5 nM before obtaining colored distributions in 3 minute intervals – time after dilution is indicated next to each colored distribution. Time of each measurement 1.5 min. **b**. Sonicated 5 nM solution of PIL-1 (402 kg/mol) in DMF. Superimposed data from 3 samples is shown. Temperature 20 °C, measurement duration 2 min.

Section 4. Theoretical modelling of local shear flow near crystals

The purpose of this theoretical model was to investigate whether the local shear flow near a crystal subject to mean shear (Couette) flow grows with crystal size, and to establish the order of magnitude of this effect. To avoid proliferation of free parameters, we present only a very simple model and geometry of the problem that still retain this scaling of local shear with crystal size. We show that the overall trend holds for both fixed (**Section 4.1**) and freely moving particles (**Section 4.2**), and for both Newtonian and shear-thinning liquids.

4.1. Stationary flow around a fixed crystal particle.

Geometry of the model is illustrated in **Figure S43**. We considered a Couette flow between two parallel walls moving in opposite directions with equal velocities $U_0/2$. Given the fixed distance D between the moving walls, and no-slip condition on the walls, this geometry corresponds to Couette flow with shear rate $\dot{\gamma}_0 = U_0/D$. Crystal was situated in the liquid in the middle of the inter-wall gap. Crystal shape was assumed to be a rod with its longest dimension parallel to the cell walls and perpendicular to wall velocity vectors – in other words, pointing into the drawing in **Figure S43**. Cross-section of this rod-like crystal was a square with edge length L and corners of this square were rounded with the radius of curvature $r_c < L/2$. It was assumed that the longest dimension of this rod-like crystal is much greater than L, so the problem can be treated as two-dimensional. This last assumption is not only convenient but also roughly corresponds to the typical crystal shape and orientation we observed experimentally for trimesic acid crystallizing in PIL-1/DMF (cf. **Figure 1c** in the main text).
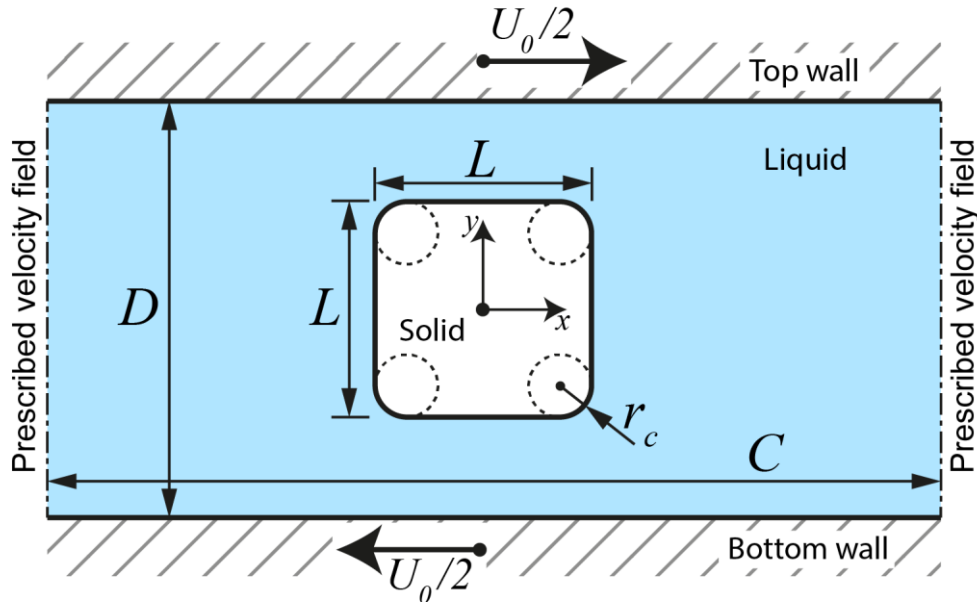
Figure S43. **Geometry of the model**. Top and bottom moving walls (hatched) confine the liquid (dotted volume) hosting the solid particle whose cross-section is a smoothed rectangle (edge L, radius of corner curvature r_c). Boundary conditions are described in the text.

Fluid velocity vector field $\boldsymbol{u}$ was found by numerically solving Navier-Stokes equations for stationary incompressible flow:

$$\rho(\boldsymbol{u} \cdot \nabla)\boldsymbol{u} = \nabla \cdot [-p\boldsymbol{I} + \mu(\nabla\boldsymbol{u} + (\nabla\boldsymbol{u})^T) \ ]$$
$$\nabla \cdot (\rho\boldsymbol{u}) = 0$$

Here, ρ is the density, μ is the dynamic viscosity, $\boldsymbol{I}$ is the identity matrix. In contrast to the actual shear-thinning of our PIL-1/DMF solutions, liquid in our models was treated as Newtonian: dependence of viscosity on shear rate was ignored but realistic non-Newtonian case yielded similar results as described below in **Section S4.2**. External walls of the cell, as well as surfaces of the crystal particle were modelled with "no slip" boundary conditions: fluid at each solid surface had the same velocity as the surface itself ($\boldsymbol{u} = (0, 0)$ at the crystal surfaces, $\boldsymbol{u} = (\frac{U_0}{2}, 0)$ at the top wall of the cell, $\boldsymbol{u} = (-\frac{U_0}{2}, 0)$ at the bottom wall). Prescribed velocity field corresponding to simple Couette flow was set at the "ends" of the calculation volume (dash-dot lines in **Figure S43**):

$$u_y = 0$$
$$u_x = \frac{U_0}{2} \cdot \frac{y}{D/2}$$

Coordinate y is defined such that $y = 0$ in the middle of the gap between the walls of the cell. The distance C between the ends of the calculation volume was chosen such that its further increase did not influence the calculation results; we found that $C = 20D$ was enough to fulfill this condition.

Stationary flow field was calculated by using finite-element method with linear elements for the velocity components and for the pressure field. Meshing algorithm and linear direct PARDISO solver were provided by COMSOL Multiphysics 5.1 software package. In the simulations we present here, parameter values were $\rho = 1.6$ g/cm^3, $\mu = 0.1$ Pa$\cdot$s, $D = 1$ mm, $\dot{\gamma}_0 = 167 \ s^{-1}$ (corresponds to 400 rpm in our experiments), $U_0 = D\dot{\gamma}_0 = 167$ mm/s.

Typical picture of the stationary flow is shown in **Figure S44.** Calculations show that shear rate is highest near the corners of the particle (**Figure S44c**). Scaling of this maximal value of local shear rate with size L of the crystal for a fixed corner sharpness r_c is presented in **Figure 5a** of the main text.
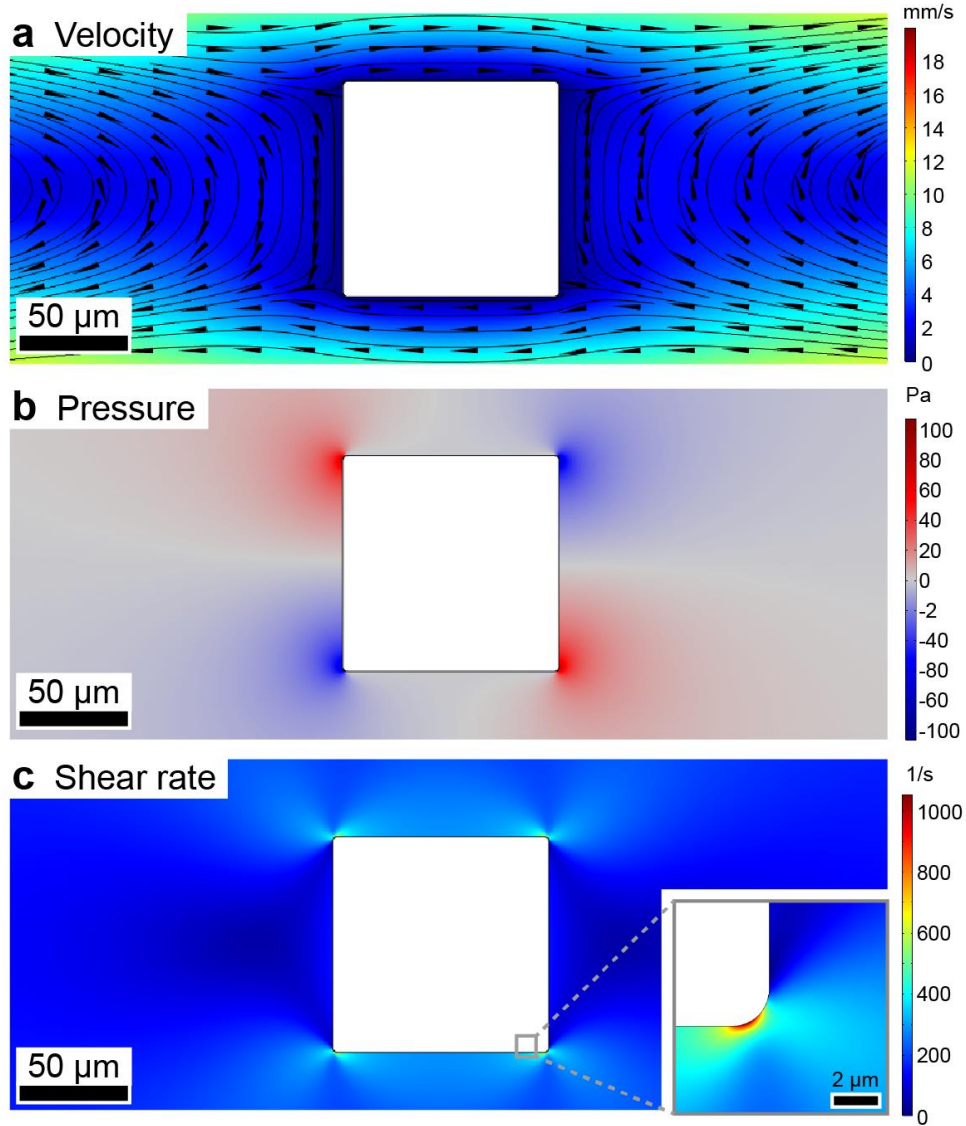
Figure S44. **Stationary flow around a fixed crystal particle** of size $L = 0.1$ mm and corner curvature $r_c = 2$ µm. **a,** Velocity map. Color represents velocity magnitude, streamlines are plotted along velocity vectors. Arrow cones indicate direction of velocity at their tails. **b,** Map of pressure measured with respect to ambient value. **c,** Map of shear rate. Inset shows magnified corner.

4.2. Case of freely moving crystal particle

We start with the same initial conditions as in **Figure S43**, but allow the particle to freely move and rotate. However, if the flow is laminar and hydrodynamic instabilities can be neglected, it is easy to see from the symmetry of this 2D problem that the center of the particle will remain at the same initial point, and only the rotation of the particle around its center will commence. Navier-Stokes equations in this case are in time-dependent form:

$$\rho \frac{\partial \boldsymbol{u}}{\partial t} + \rho(\boldsymbol{u} \cdot \nabla)\boldsymbol{u} = \nabla \cdot [-p\boldsymbol{I} + \mu(\nabla \boldsymbol{u} + (\nabla \boldsymbol{u})^T)]$$

$$\rho \nabla \cdot (\boldsymbol{u}) = 0$$

but now the mesh for finite-elements method must be continuously deformed by the motion of the particle. Arbitrary Lagrangian-Eulerian (ALE) method was used to couple the Eulerian description of fluid flow equations formulated in the deformed reference frame and the Lagrangian description of the solid particle motion formulated in non-deformed (global) reference frame.

Force exerted on the particle boundary is opposite to the reaction force of the fluid:

$$\boldsymbol{f} = \boldsymbol{n} \cdot \{-p\boldsymbol{I} + \mu(\nabla \boldsymbol{u} + (\nabla \boldsymbol{u})^T) \}$$

This force should be transformed from deformed (mesh) reference frame to undeformed (global) reference frame. If mesh element scale factors in these two reference frames are dm and dM, respectively, the transformed force vector is

$$\boldsymbol{F} = \boldsymbol{f} \frac{dm}{dM}$$

Reaction force vector at each element of the particle surface contributes to the net torque, which is then used to integrate the solid-body rotation of the particle. In turn, the influence of the particle's motion on the fluid is modeled by matching fluid velocities on particle's boundary (the "no slip" condition) to velocities $\boldsymbol{u}_p = \boldsymbol{\omega} \times \boldsymbol{r}$ computed from particle's instantaneous angular velocity $\boldsymbol{\omega}$ at all points of the particle surface (defined by radius-vectors $\boldsymbol{r}$ from the axis of rotation).

Model's equations were solved using finite-element method with linear elements for the velocity components and for the pressure field. Meshing algorithm and solver were provided by COMSOL Multiphysics 5.1 software package. To maintain the mesh quality near the moving boundaries during the deformation of the mesh, complete remeshing was performed during the simulation whenever mesh deformation (defined similar to the Cauchy strain) exceeded 0.6 for at least one mesh element. After such remeshing, all fields were interpolated from old mesh to the new one and the simulation recommenced from the preceding time step. Linear direct PARDISO solver was used in combination with fully coupled nonlinear Newton solver for obtaining time-dependent solution from 0 to 0.2 s in 0.001 s steps (or smaller steps chosen by BDF stepping algorithm having maximum order 2 and minimum order 1).

As for the stationary case, parameter values we used for the case of a freely floating particle were $\rho = 1.6$ g/cm^3, $\mu = 0.1$ Pa$\cdot$s, $D = 1$ mm, $\dot{\gamma}_0 = 167$ s^{-1}, $U_0 = D\dot{\gamma}_0 = 167$ mm/s, and the density of the crystal equal to 2 g/cm^3. Note that crystal density does not play a significant role in our experimental conditions. For millimeter-scale crystals and liquid viscosity 0.1 Pa$\cdot$s, crystal particle rapidly (in ca. 0.2 milliseconds, see **Figure S45**) adopts its terminal value $\omega_T \approx \dot{\gamma}_0/2$ of angular velocity. If period or rotation $2\pi/\omega_T$ (~72

ms for our parameters) is much larger than this relaxation time, inertia of the particle can be neglected, and therefore density becomes unimportant.
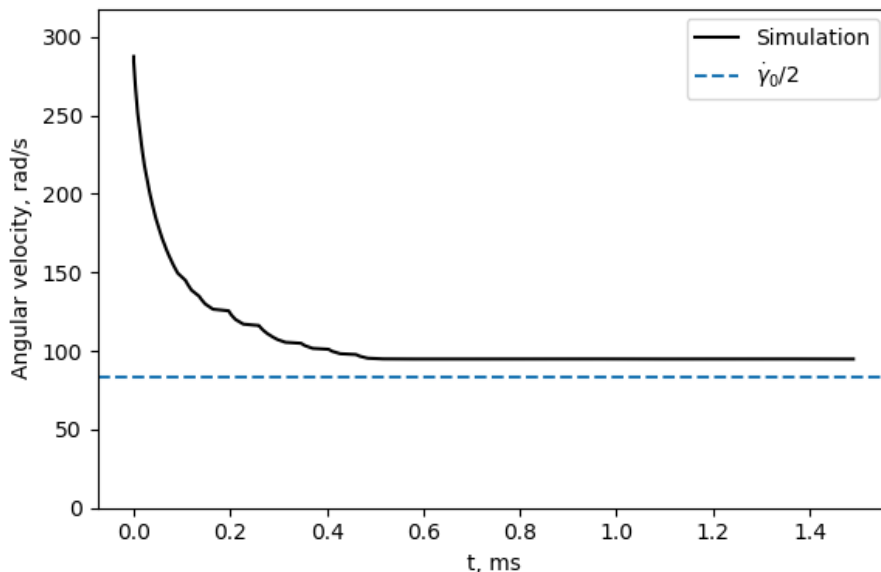
Figure S45. **Relaxation to terminal angular velocity**. In this example, crystal size was $L = 0.2$ mm, corner curvature was $r_c = 2$ µm.

As in the case of a fixed particle discussed above, local shear rate near moving particle is highest near its corners (**Figure S46a-d**). As particle rotates in the flow, minimum shear rate, plotted against time in **Figure S46e**, is reached whenever particle faces are parallel to the moving walls (**Figure S46a**). Maximum shear rate is reached whenever the two corners of the particle point towards the moving walls (**Figure S46d**). Maxima over both space and time (that is, highest points in **Figure S46e**) were calculated for various L and r_c and are plotted in **Figure 5a** in the main text.

To implement realistic dependence of viscosity on shear rate, we used in our simulations measurements shown in the main-text **Figure 4d** (solid blue curve, molecular weight 402 kg/mol, concentration 2 mM). Achieving numerical stability during the initial transient processes at the start of the simulation was harder for this non-Newtonian case. As a stabilization method, we used constant (Newtonian) viscosity (0.1 Pa s) for the first 5 ms of the simulation to let the flow fully develop. Then, constant viscosity was gradually (over the span of 10 ms) replaced with viscosity that depends on the shear rate. This transition was completed by 15 ms (indicated by grey arrow in **Figure S46e**) and the rest of the simulation was computed using the realistic, shear-thinning viscosity. The resulting flow and particle rotation were very close to the results obtained with constant viscosity 0.1 Pa, as can be seen by comparing the orange and blue curves in **Figure S46e**. We conclude that while the shear thinning may affect the flow at the initial stages of the flow development, in a steady regime of flow and rotation of the particle it would produce the same scaling of local shear rate with crystal size as in the Newtonian case.
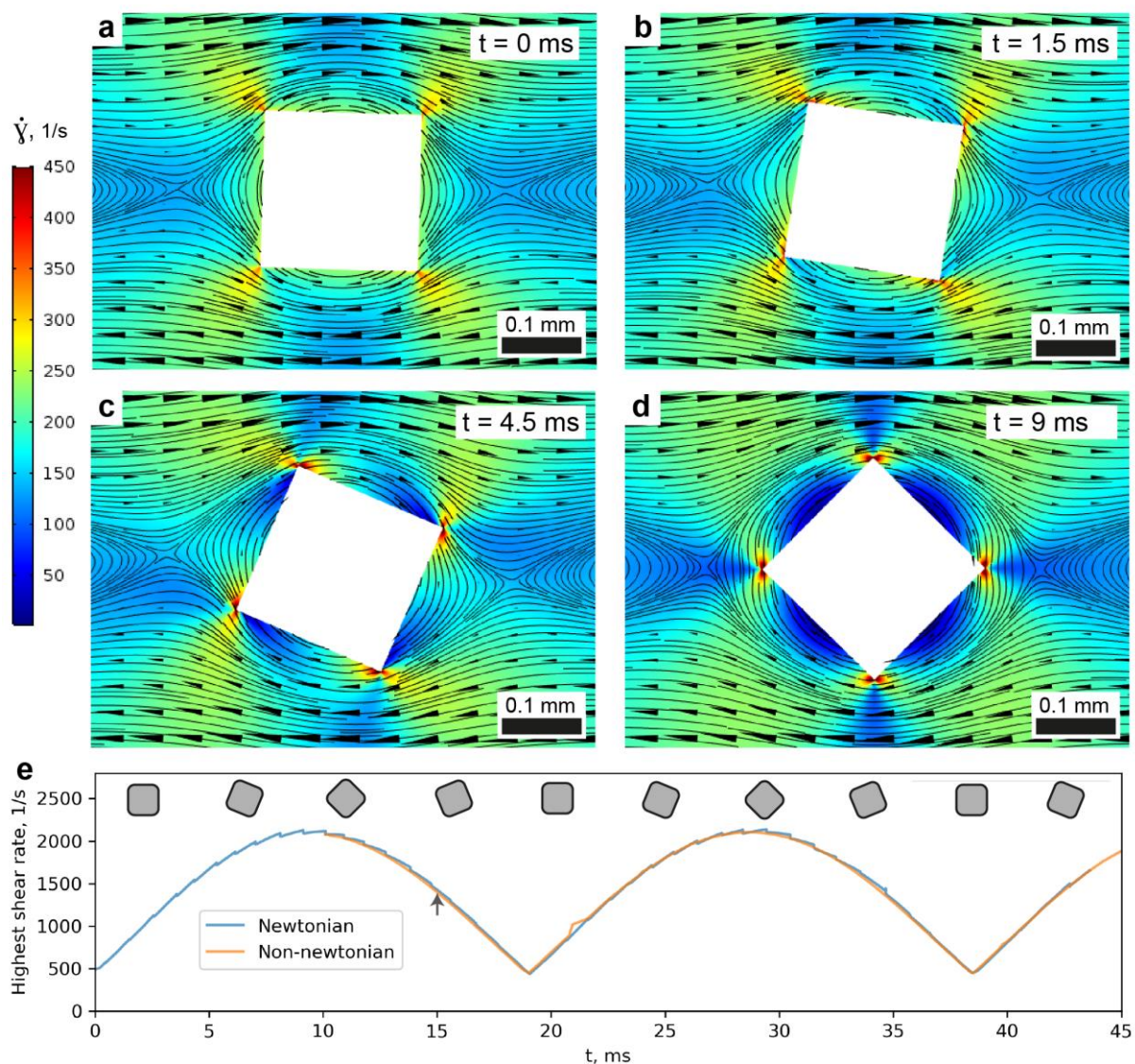
Figure S46. **Evolution of local shear rate during particle rotation in the Couette flow**. Particle size here is $L = 0.2$ mm, and corner sharpness $r_c = 2$ μm, but the picture is qualitatively similar for other values L and r_s. **a-d**. Shear rate maps at different moments during one 45° rotation of the particle. Shear rate is indicated by color (color scale is on the left). Streamlines show velocity field. Arrow cones indicate direction and magnitude of velocity. **Movie S3** shows a complete animation of this map in 1 ms steps. **e**. Maximum local shear rate plotted against time for Newtonian liquid (blue curve) and for the non-Newtonian case (orange) where we used realistic dependence of viscosity on shear rate from solid blue curve in **Figure 4d**. Corresponding orientations of the particle are indicated by grey squares above the curve. Small sawtooth-like fluctuations are artefacts of calculation: jumps of maximum value happen after each remeshing, since maximum is evaluated over mesh elements.

4.3. Viscous heating.

To estimate the temperature increase near the crystal particle due to viscous dissipation, fluid velocity field $\boldsymbol{u}(\boldsymbol{r},t)$ and pressure field $p(\boldsymbol{r},t)$ obtained by numerically solving Navier-Stokes equations for stationary flow (**Section 4.1**) were used in heat transfer equations:

$$\rho(T)C_p\frac{\partial T}{\partial t} + \rho(T)C_p\boldsymbol{u}\cdot\nabla T + \nabla\cdot\boldsymbol{q} = Q_p + Q_{vd}$$

where T is the temperature, C_p is the specific heat capacity at constant pressure, $\boldsymbol{q}$ is the heat flux by conduction:

$$\boldsymbol{q} = -k\nabla T$$

where k is the heat conductivity. Q_p denotes heat due to the work done by pressure changes, Q_{vd} is the heat due to viscous dissipation:

$$Q_p = \beta T\left(\frac{\partial p}{\partial t} + \boldsymbol{u}\cdot\nabla p\right)$$

$$Q_{vd} = \boldsymbol{\tau}:\nabla\boldsymbol{u} = 2\mu\left(\left(\frac{\partial u_x}{\partial x}\right)^2 + \left(\frac{\partial u_y}{\partial y}\right)^2 + \left(\frac{\partial u_z}{\partial z}\right)^2 - \frac{1}{3}(\nabla\cdot\boldsymbol{u})^2\right) + \mu\left(\frac{\partial u_y}{\partial x} + \frac{\partial u_x}{\partial y}\right)^2$$

$$+ \mu\left(\frac{\partial u_z}{\partial y} + \frac{\partial u_y}{\partial z}\right)^2 + \mu\left(\frac{\partial u_x}{\partial z} + \frac{\partial u_z}{\partial x}\right)^2$$

where β is the volumetric thermal expansion coefficient, $\boldsymbol{\tau}$ is the viscous stress tensor, colon denotes double inner product.

Boundary conditions with constant temperature were maintained on the top and bottom moving walls, while the surface of the particle was assumed to be thermally insulating. Left and right edges of the calculation volume (dash-dotted vertical lines in **Figure S43**) had periodic boundary condition for the temperature and the heat transfer.

We only solved for the stationary flow and temperature field, neglecting the rotation of the particle as in **Section 4.1**. We solved heat transfer equations on the same mesh as used for fluid dynamics equations. The second direct PARDISO solver was used to solve for temperature during the second step of a segregated stationary solver. Values of specific heat, thermal capacity, and volumetric thermal expansion coefficient were equal to those of DMF: $C_p = 1998$ J/(kg $\cdot$ K), $k = 0.184$ W/(m $\cdot$ K), $\beta = 10^{-4}$ K^{-1} (Ref. S24).

Simulations showed that increase of temperature with respect to ambient 20 °C never exceeded $3\cdot 10^{-3}$ °C, the hottest region being the middle of the gap between the moving walls (**Figure S47**). Despite the relatively large shear localized near the particle's corners (**Figure S46a-d**), temperature at these corners was not significantly different from the average temperature in the middle of the interwall gap.

It can be concluded that thermal factors do not play any significant role in our experiments. Besides, even if heating were appreciable, it would oppose the ripening by making larger crystals more soluble (solubility normally increases with temperature, and stronger shear near larger crystals would heat them more than their smaller neighbors), contrary to the trend we observe experimentally for the crystal growth enhancement by shear.
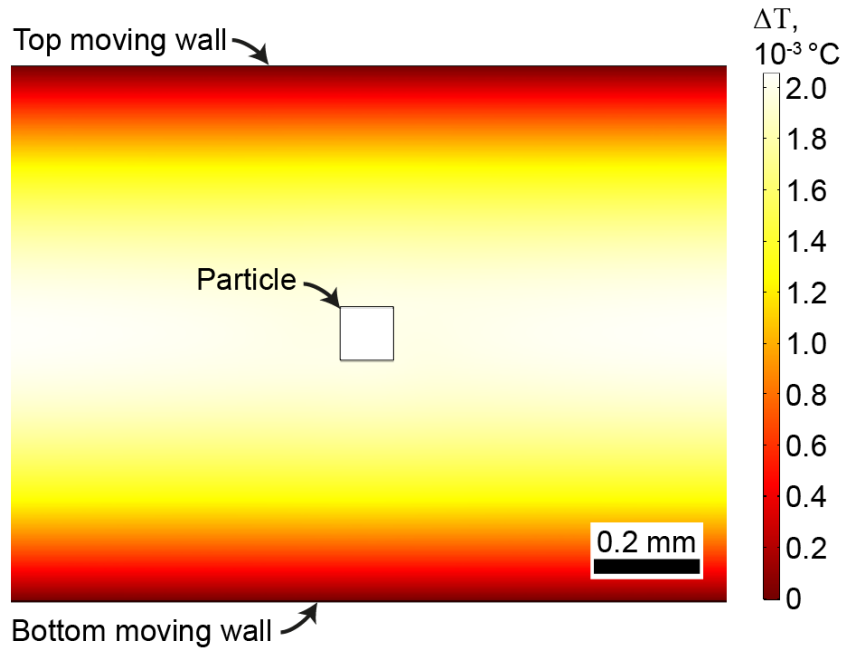
Figure S47. **Effect of viscous heating on the stationary distribution of temperature** in the Couette cell with a fixed particle in the middle. Color scale for temperature is on the right. Particle size $L = 0.1$ mm, corner curvature $r_c = 2$ μm.

4.4. Radial uniformity of shear rate in the Couette cells

Tangential velocity of flow between two coaxial cylinders with radii R_1 and R_2, if only the inner cylinder rotates with angular velocity Ω, is[S25]:

$$v_\theta(r) = ar + \frac{b}{r}$$

where r is the radius from the axis of rotation, and constants a and b are given by

$$a = -\frac{\Omega R_1^2}{R_2^2 - R_1^2}$$

$$b = \frac{\Omega R_1^2 R_2^2}{R_2^2 - R_1^2}$$

This simple flow (Couette flow) only takes place if Reynolds number $Re = \Omega R_1 (R_2 - R_1)\rho / \mu$ does not exceed ca. 100; otherwise, Couette flow becomes unstable and develops into more

complicated flow structures[S26,S27]. At our experimental parameters, $Re < 2$. Shear rate is therefore[S28]

$$\dot{\gamma}(r) = \frac{dv_\theta(r)}{dr} - \frac{v_\theta(r)}{r} = -\frac{2b}{r^2}$$

Plots of $|\dot{\gamma}(r)|$ for R_1, R_2 and Ω of our experimental Couette cells are shown in **Figure S48**.
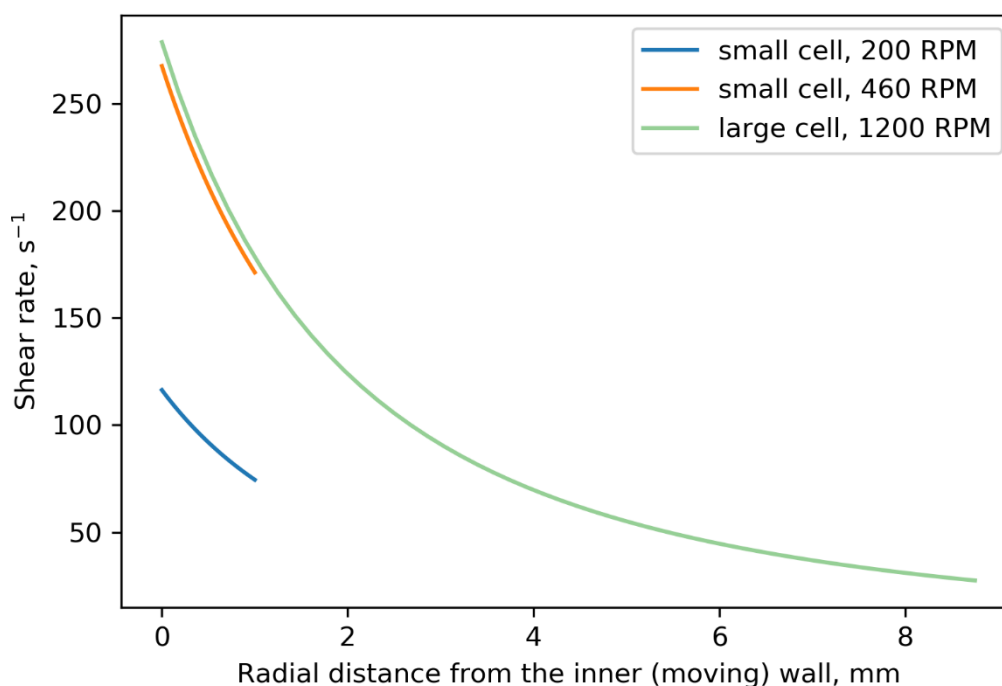
Figure S48. Radial distribution of shear rate in experimental Couette cells. Large cell: inner wall radius 4 mm, outer wall radius 12.7 mm, rotation speed 1200 rpm. Small cell: inner wall radius 4 mm, outer wall radius 5 mm, rotation speed either 200 rpm or 460 rpm.

One can see that for the small cells, variation of shear rate are no more than 20% around the average shear rate, independently of the rotation speed.

Radial variation of shear rate in the large cell is much stronger: shear rate near the outer wall is ca. 5 times lower than shear rate near the inner wall, which owes to the large ratio R_2/R_1 of the large cell we used. Couette cells with large inter-wall gap $D = R_2 - R_1$ but small ratio of radii R_2/R_1 would have required larger R_1 and R_2 and therefore larger volume of material (especially, poly-ionic liquid) to fill ($V \propto R_2^2 - R_1^2 = (R_2 + R_1)/(R_2 - R_1) = (R_2 + R_1)/D$). Instead of increasing R_1 of large cell, we compared the crystals grown in a large cell at 1200 rpm to crystals obtained in small cell with different rotational rates (either 460 rpm or 200 rpm). As one can see from **Figure S48**, small cell rotated at 200 rpm has shear rates similar to *average* shear rate in the large cell. Alternatively, small cell rotated at 460 rpm reproduces shear rates

similar to the region of highest shear rates in the large cell. Since smaller rotational rates generally lead to smaller crystals (see **Figure 4a** in the main text), but crystals grown in 1 week at either rotational rate in the small cell are ca. 10 times smaller than crystals grown in the large cell in the same time, this difference in sizes can only be due to increased gap as such, not due to variations/non-uniformity of shear rate.

Section 5. Design of magnetically actuated Couette cells.

Couette cells were fabricated from two glass test tubes (dimensions shown in **Figure S49**), two ball bearings (6800Z EZO Japan, internal Ø10 mm, external Ø19 mm, thickness 5 mm), three 3D-printed elements, two spherical permanent magnets (Nd, Ø5 mm) and a bit of epoxy (EPO-TEK 310M-2). 3D-printing was performed with ProJet 3510 HD Plus printer. Assembly sequence and technical drawings of 3D-printed elements are shown in **Figure S49**. If needed, the elements we 3D-printed (**Figure S49**, bottom) can be manufactured from harder materials using a lathe, since these shapes all have rotational symmetry.

The assembly should be performed as follows. First, a 3D-printed spacer, a permanent spherical magnet, a bit of epoxy, and another copy of same spacer are inserted into the inner glass tube (**Step 1**). Function of these spacers is to align the magnet center with the axis of the tube. To orient the spherical magnet such that its magnetic field is perpendicular to the axis of the tube, a larger magnet was kept underneath the tube while the epoxy was hardening (**Step 2**). After epoxy around the first magnet has hardened, second spherical magnet was inserted into the tube with some epoxy. External magnet was present during the hardening of this epoxy as well. It's crucial that these magnets are glued into the tube one by one, not two or more at once – if both magnets are put into the tube together, they will align such that their magnetic dipoles are aligned vertically. Note that two spherical magnets are required for using this Couette cell with liquids of viscosity around $0.1 \div 1$ Pa·s; one magnet does not provide enough torque with conventional magnetic stirrers (we used IKA RCT B S0A0 and DAIHAN Scientific MS-MP8 stirrers).

After both magnets are glued inside the inner tube, this tube is inserted into a 3D-printed sleeve, and a ball bearing is put on the sleeve. This assembly is then inserted into the main holder (**Figure S49**, **Step 4**). Second ball bearing is put on the sleeve from the top (**Step 5**). This second ball bearing is necessary to keep the axis of rotation of the inner tube stable. Finally, outer glass test tube is filled with the liquid mixture of interest and inserted into the main holder from below (**Step 6**).

Assembly is placed vertically at the center of the magnetic stirrer plate (e.g., IKA RCT B S0A0) or at one of the points of a multipoint magnetic stirrer (e.g., DAIHAN Scientific MS-MP8). If the friction between the stirrer plate and the assembly's glass bottom is not sufficient to prevent sliding/slipping of the assembly, a piece of double-sided sticky tape should be added between the plate and the stirrer. For viscous liquids, torque applied by the stirrer might be not sufficient

to overcome the sum of viscous force and friction in the bearing. For this reason, care should be taken to make sure that the inner tube rotates at the rate of the magnetic stirrer – if there is a mismatch of angular velocities, inner tube will move in jumps instead of rotating uniformly.
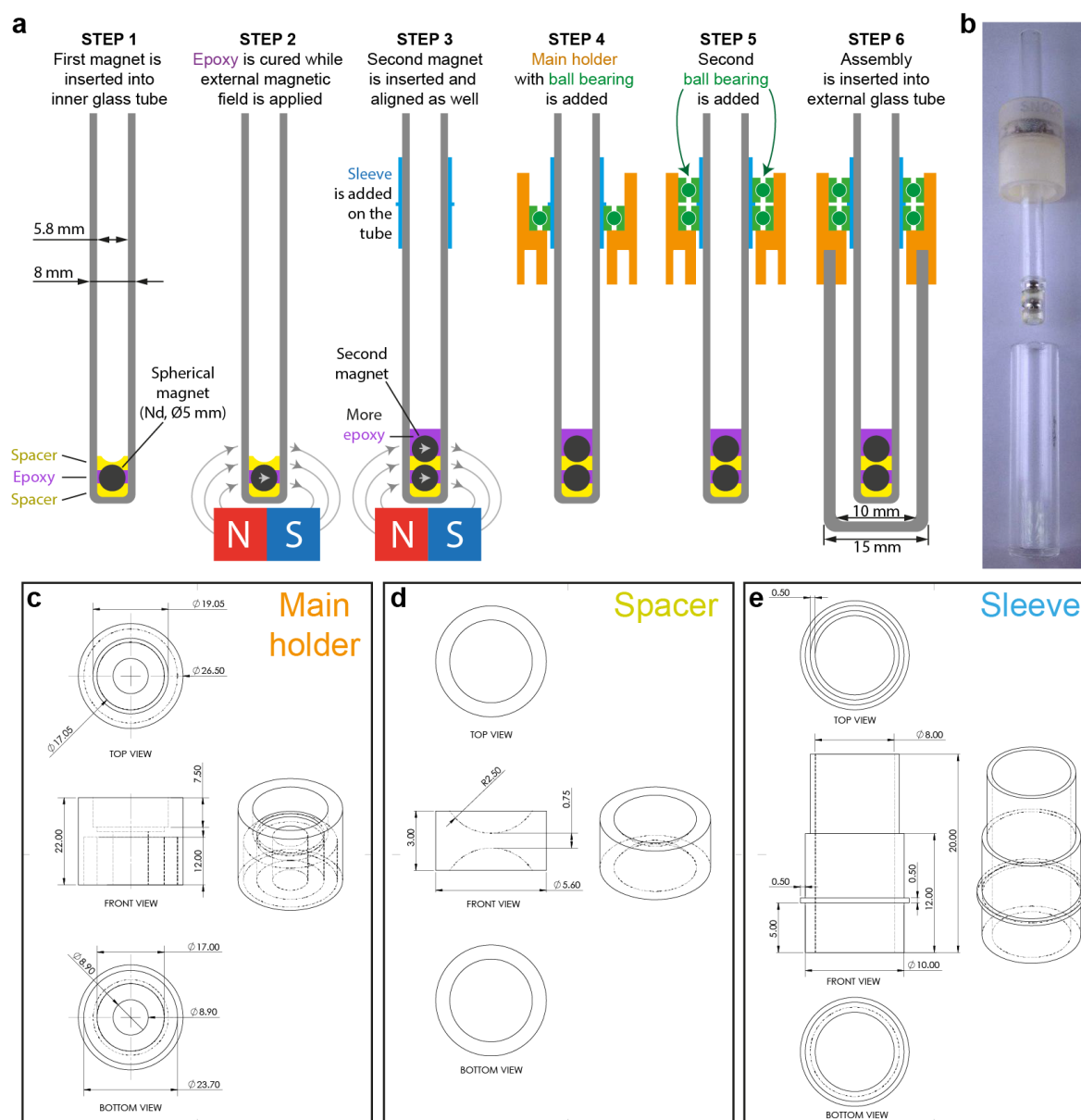
Figure S49. **Design and manufacturing of Couette cells** compatible with conventional laboratory magnetic stirrers. **a,** Sequential steps of assembly sequence. See text for details. **b,** Photo of an assembled cell; outer tube is temporarily detached. **c-e,** Technical drawings of 3D-printed elements.

Section 6. Additional rheological studies

It is instructive to put these qualitative arguments in the context of scaling arguments of polymer physics. In particular, the so-called Weissenberg number $\mathrm{Wi} = \dot{\gamma}\tau$, which is the ratio of shear rate $\dot{\gamma}$ to the relaxation rate $1/\tau$ of the polymer, is commonly used to estimate whether polymer's microstructure would be affected by shear: this influence becomes visible

at Wi ~ 1 and for some systems has been shown[S40] to saturate at Wi ~ 100. Viscoelastic measurements of PIL-1 give relaxation rates 22 s^{-1} for MW 8.49×10^5 g/mol, and 314 s^{-1} for MW 4.02×10^5 g/mol, matching estimates obtained from empirical scaling relationships (16 s^{-1} and 355 s^{-1}, respectively; see details below) and corresponding to Wi = 8 and Wi = 0.5 in mean shear 167 s^{-1}. Note that PILs with longer chains relax slower, so they are more responsive to shear. On the curves of viscosity vs. shear rate, these relatively fast relaxations are probably responsible for the "secondary" shear-thinning that onsets at $\sim$50 s^{-1} (**Figure 4e**). Primary, stronger shear thinning at $\dot{\gamma} < 10$ s^{-1} (**Figure 4d**) owes to much slower relaxations with rates below 10^{-4} s^{-1}, which are likely related to entanglement or gel-like structuration; for these slow relaxations, Wi > 10^4 at our typical shear rates. Also, since local shear rates near a crystal particle are always larger than the mean shear rate and increase with crystal size, the requirement for *local* Wi to be within the $1 - 100$ range can be satisfied even for fast relaxations by the *mean* shear rates we used in experiments ($25 \div 167$ s^{-1}) – e.g., based on the data from **Figure 5b**, local Wi is equal to 20 for short-chain PIL near 0.2-mm-sized crystals with corner curvature radius 200 nm when mean shear rate is 167 s^{-1}. All in all, disentanglement and other changes of polymer microstructure are theoretically feasible within the range of shear rates we apply ($25 \div 167$ s^{-1}).

In order to estimate the relaxation times of PIL-1/DMF mixtures, dynamic relaxation measurements were performed on Anton Paar MCR 502 WESP rheometer (cone-plate configuration) for PIL-1 with molecular weights 402 000 g/mol and 849 000 g/mol at concentration of 300 mg per 0.75 mL DMF (same as in crystal growth experiments) and 3 hours after PIL-1 and DMF were mixed. First, to choose the proper strain for frequency sweeps, amplitude sweeps were performed to find the linear viscoelastic region (LVR). This region was found to span up to ca. 1% (**Figure S50a**), and this strain was used for all subsequent frequency sweeps for both polymers. Note that $G' \cong G''$ at low strains in the linear viscoelastic region in **Figure S50a** may indicate gel-like behavior at low frequency (10 Hz).

The frequency ω_c – which storage modulus G' and loss modulus G'' cross over (intersections marked by black dots in **Figure S50b**) and which corresponds to the inverse of the characteristic relaxation time of the structured liquid – increased with decreasing molecular weight: 22 s^{-1} for MW 849 000 g/mol, and 314 s^{-1} for MW 402 000 g/mol. Notably, these values are of the same order of magnitude as the relaxation rates estimated from empirical relationship for unentangled polymers. They are also of the same order of magnitude as the critical shear rate of the onset of "secondary" shear thinning (50 s^{-1} for MW 402 000 g/mol, see **Figure 4** in the main text).

Further evidence linking the measured relaxation rates to the "secondary" shear thinning is the equality of "zero-shear viscosity" η_0 obtained by fitting $G''(\omega)$ and the viscosity η_0 at the Newtonian plateau (around 10 s^{-1}) of the "secondary" shear thinning. At frequencies below ω_c, polymer with MW 402 000 g/mol shows Maxwell behavior: the storage modulus G' scales as ω^2, the loss modulus G'' scales as ω (as indicated by log-log slopes 1 and 2 for blue curves

in **Figure S50b**). For a Maxwell material, prefactor in linear scaling of $G''(\omega)$ is expected to be approximately equal to the zero-shear viscosity η_0 and can be determined from a linear fit $G''(\omega) = \eta_0\omega$ to the $G''(\omega)$ curve in **Figure S50b** in the low-frequency region. This fitting results in $\eta_0 = 0.14$ Pa·s, which closely matches the onset viscosity $\eta_0 = 0.13$ Pa·s of the "secondary" shear thinning (see the dark blue curve in **Figure 4d-e** in the main text).

The experimentally measured relaxation times roughly match the longest Rouse relaxation time estimated by using scaling relationships. For a dilute, unentangled polymer solution, the Rouse relaxation time is given by[S29,S30] $\tau_R = \eta R_g L^2 / \pi k_B T$, where η is the dynamic viscosity, R_g is the gyration radius, L is the polymer chain length, k_B is Boltzmann constant, and T is temperature. From DLS measurements of hydrodynamic radius (see details in **SI Section S3**) we estimated $R_g \approx 4$ nm for PIL-1/DMF. For PILs with molecular weights 402 kg/mol and 849 kg/mol, viscosities are about 0.1 Pa·s and 0.5 Pa·s (**Figure 4d**, solid curves), and chain lengths are 299 nm and 632 nm, respectively. These values result in a relaxation rate $1/\tau_R$ equal to 16 s^{-1} for the long-chain PIL (MW 849 kg/mol) or 355 s^{-1} for the short-chain PIL (MW 402 kg/mol).

The "primary" shear thinning, which occurs at $\dot{\gamma} < 10$ s^{-1} (see **Figure 4d**) is likely related to entanglement between polymer chains, since entanglement relaxation is expected to be much slower than Rouse dynamics. Theoretically, the relaxation time related to entanglement of polymer chains is $\tau_e = 3\tau_R N/N_e$ (see Refs. [S31,S32]), where $N = L/R_g$ and N_e is entanglement length, unknown for our PIL-1/DMF solution. Yet, for polymers, typically, $5 < N/N_e < 100$, so the longest entanglement relaxation time τ_e can be at least 30 times larger than τ_R in our case, which puts its relaxations rate at < 12 s^{-1} for the short-chain PIL (MW 402 kg/mol). In case of MW 849 000 g/mol, strong entanglement or gel-like structuration might be responsible for observed transition from a liquid-like to solid-like regime at $\omega_c = 22$ s^{-1} (orange curves **Figure S50b**) with a very flat "rubbery plateau" at $\omega > \omega_c$.

Overall, these measurements show that relaxations of polymer microstructure (both entanglement and Rouse dynamics) in our solutions are slow enough for this microstucture to be significantly affected by shear rates present in our crystal growth experiments.
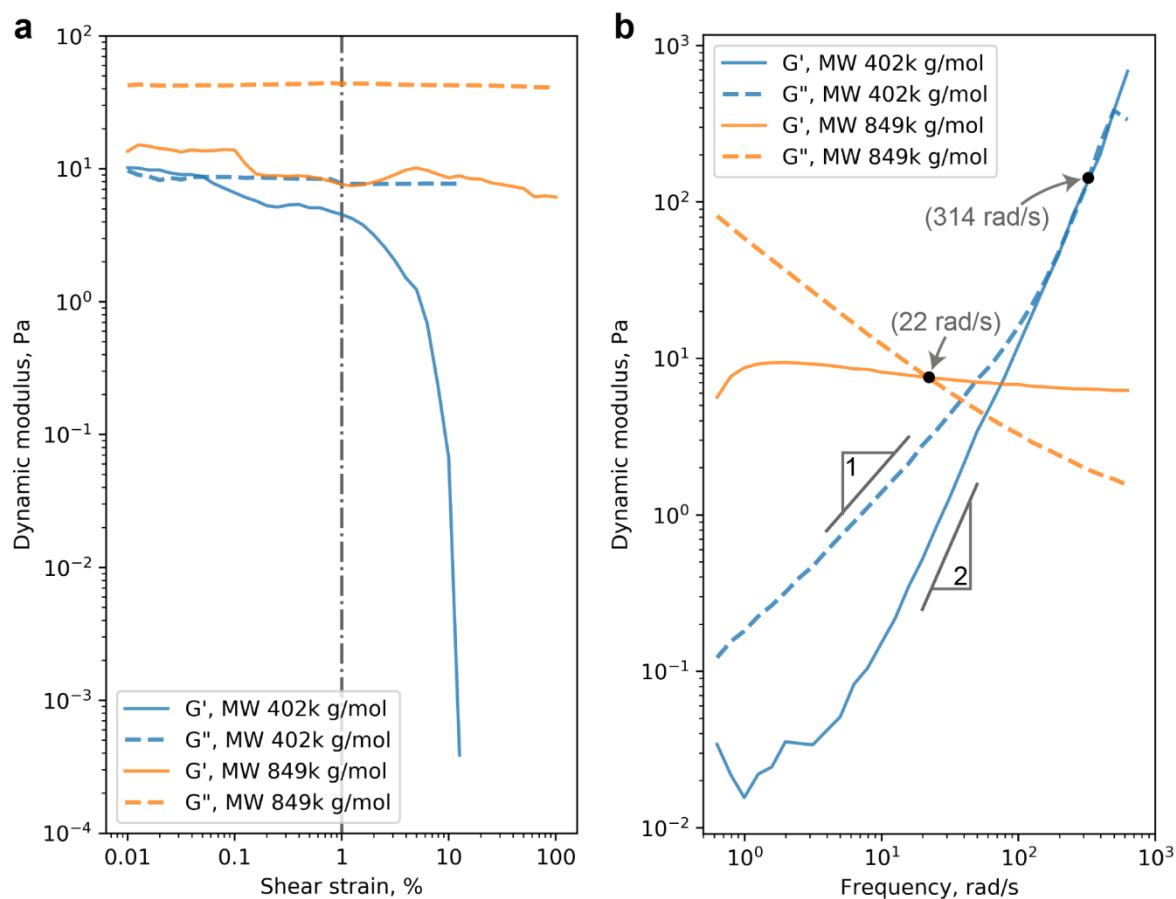
Figure S50. **Dynamic relaxation data for PIL-1. a**, Plot of storage modulus (G') and loss modulus (G") for amplitude sweep at 10 Hz performed for evaluating the span of linear viscoelastic region. Both polymers demonstrate liquid behavior (G" > G'), with the possible exception of 402 000 g/mol polymer at the lowest strains (blue curves), where it approaches gel-like behavior. Dash-dotted vertical line corresponds to the 1% strain used in all frequency sweeps. **b**, Frequency sweeps at 1% strain. For each molecular weight, the point where G' and G" cross over (black dots) corresponds to frequency (denoted by grey arrow) that is the inverse of the characteristic relaxation time of the structured liquid. Exponents of the power laws for 402 000 g/mol (blue curves) are indicated on the plot. In all cases, concentration of polymer is 300 mg per 0.75 mL DMF. Measurements were performed 3 hours after PIL-1 and DMF were mixed.

Section 7. Extension of LSW theory of coarsening to the case of shear flow.

Lifshitz & Slyozov[S33] and Wagner[S34] (LSW) theory for diffusion-controlled Ostwald ripening predicts that the average particle (crystal) radius $r(t)$ grows with time t as

$$r^n(t) - r^n(0) = Kt \qquad (7.1)$$

where n is the so-called coarsening exponent equal to 3 for diffusion-controlled ripening (i.e. with negligible fluid flow), and K is the rate constant having diffusion-limited value

$$K = \frac{8}{9} \cdot \frac{D\sigma\Omega c}{k_\mathrm{B}T(c_p - c)} \tag{7.2}$$

where D is the diffusion coefficient, σ is the surface energy, Ω is the atomic volume, k_B is the Boltzmann constant, T is temperature, c is the equilibrium (saturation) concentration in the solution, and c_p is the concentration inside the crystal particle (typically, $c_p \gg c$, and thus $c_p - c \approx c_p$).

Building on the approach of Ardell[S35] and White[S36], the LSW theory can be generalized to include the influence of convection and particle motion[S37,S38], resulting in values of coarsening exponent n different from 3. Here, we similarly derive the coarsening exponent and scaling of the rate constant in the case of shear flow around the particles. By differentiating both sides of the equation (7.1) with respect to time t, we can see that

$$\frac{dr(t)}{dt} = \frac{K}{n}r(t)^{1-n} \tag{7.3}$$

On the other hand, diffusional flux I' to the surface of the particle makes the particle radius grow as[S37]

$$\frac{dr(t)}{dt} = \frac{1}{4\pi r^2} \cdot \frac{I'}{c_p - c} \tag{7.4}$$

Diffusive flux on a spherical particle in a shear flow was derived by Gupalo & Riazantsev[S39]:

$$I' \approx 15.3 \cdot c_0 (\dot{\gamma}D^2 r^5)^{1/3} \tag{7.5}$$

where $\dot{\gamma}$ is the mean shear rate of the flow, and c_0 is the concentration of the diffusing species. By combining (7.5) with Gibbs-Thomson equation as described by Ratke and Thieringer[S37] and substituting the resulting flux into (7.4), we obtain

$$\frac{dr(t)}{dt} \propto \frac{\dot{\gamma}^{1/3}D^{2/3}\sigma\Omega c}{(c_p - c)k_B T}r^{-4/3} \tag{7.6}$$

Comparing the power of r in (7.6) to the power of r in (7.3), we can conclude that the coarsening exponent n is equal to $7/3$, and the rate constant scales as

$$K \propto \frac{\dot{\gamma}^{1/3}D^{2/3}\sigma\Omega c}{(c_p - c)k_B T} \tag{7.7}$$

Finally, (7.1) formula for average crystal size becomes

$$r^{7/3}(t) - r^{7/3}(0) \propto \frac{\dot{\gamma}^{1/3}D^{2/3}\sigma\Omega c}{(c_p - c)k_B T}t \tag{7.8}$$

and, if $r(0)$ is negligible and $c_p \gg c$, then

$$r(t) \propto c^{3/7} \cdot \dot{\gamma}^{1/7} \cdot D^{2/7} \cdot t^{3/7} \tag{7.9}$$

Thus the average crystal size monotonously increases with equilibrium solubility (saturation concentration), shear rate, diffusion coefficient, and time. Note that the dependence on shear rate is weak: size grows as the seventh root of the shear rate.

Section 8. Movie captions.

Movie S1. **Growing crystals in shear flow created using conventional stirring bar**. We start by pouring undersaturated solution of TA in DMF (47 mg of TA / 0.4 mL of DMF) on top of 0.35 mL of the same solvent containing a polyionic liquid polymer (300 mg of PIL-1, MW 402 kg/mol) in a glass vial containing a stirring bar and placed on a magnetic stirrer. The video begins when the stirrer is turned on (at 400 rpm). Right side of the frame shows enlarged part from the red rectangle on the left. Real time is shown in the top left corner. After the 0:30 mark, video jumps forward by increments of 10 minutes, showing 5 seconds at real-time speed after each jump. At the end of the video, microscope images (taken in crossed polarizers) of the produced crystals are shown.

Movie S2. **Growth of TA crystals in PIL-1/DMF solution under shear**. We start by mixing undersaturated solution of TA in DMF (47 mg of TA / 0.4 mL of DMF) with 0.35 mL of the same solvent containing a polyionic liquid polymer (300 mg of PIL-1, MW 402 kg/mol). Time indicated at the top of the frame is measured from the beginning of stirring. Needle-shaped crystals become visible to a naked eye after ~30 sec of rotation. First two minutes of the experiment are presented at real-time speed. It is followed by a fast time-lapse of snapshots at one-minute intervals obtained by briefly stopping the rotation of the Couette cell (to minimize the motion blue) and taking a photo. Final snapshot of the video (at **2:39**) corresponds to 63 minutes of real time after the start of Couette cell rotation. At the end of the video, microscope images (taken in crossed polarizers) of the produced crystals are shown.

Movie S3. **Simulated evolution of local shear rate during particle rotation in the Couette flow**. Shear rate is indicated by color (color scale is on the left). Streamlines show velocity field. Arrow cones indicate direction and magnitude of velocity. Particle size here is $L = 0.2$ mm, and corner curvature $r_c = 2$ µm, but the picture is qualitatively similar for other values of L and r_s. This movie corresponds to **Figure S46a-d**. Maximum local shear rate is plotted against time in **Figure S46e**. For implementation details and discussion, see **SI Section 4.**

Supplementary references:

S1. Yuan, J., Giordano, C., & Antonietti, M. Ionic liquid monomers and polymers as precursors of highly conductive, mesoporous, graphitic carbon nanostructures. *Chem. Mater.* **22**, 5003-5012 (2010).

S2. Lee, J. S., Sakaushi, K., Antonietti, M., & Yuan, J. Poly (ionic liquid) binders as Li^{+} conducting mediators for enhanced electrochemical performance. *RSC Advances* **5**, 85517-85522 (2015).

S3. Salamone, J. C., Israel, S. C., Taylor, P., & Snider, B. Synthesis and homopolymerization studies of vinylimidazolium salts. *Polymer* **14**, 639-644 (1973).

S4. Yu, X., Yuan, X., Zhao, Y., & Ren, L. Synthesis of paramagnetic polymers based on polyethyleneimine (PEI). *RSC Advances* **5**, 92207-92211 (2015).

S5. Kwolek, U., Wójcik, K., Janiczek, M., Nowakowska, M., & Kepczynski, M. Synthesis and antibacterial properties of quaternary ammonium derivative of polyethylenimine. *Polimery* **62**, 311-316 (2017).

S6. Tozawa, T., Jones, J.T., Swamy, S.I., Jiang, S., Adams, D.J., Shakespeare, S., Clowes, R., Bradshaw, D., Hasell, T., Chong, S.Y. and Tang, C. Porous organic cages. *Nat. Mater.* **8**, 973-978 (2009).

S7. Chui, S. S. Y., Lo, S. M. F., Charmant, J. P., Orpen, A. G., & Williams, I. D. A chemically functionalizable nanoporous material $[Cu_3(TMA)_2(H_2O)_3]_n$. *Science* **283**, 1148-1150 (1999).

S8. de la Peña Ruigómez, A., Rodríguez-San-Miguel, D., Stylianou, K.C., Cavallini, M., Gentili, D., Liscio, F., Milita, S., Roscioni, O.M., Ruiz-González, M.L., Carbonell, C. and Maspoch, D. Direct On-Surface Patterning of a Crystalline Laminar Covalent Organic Framework Synthesized at Room Temperature. *Chem. Eur. J.* 21, 10666-10670 (**2015**).

S9. Smith, B.J., Parent, L.R., Overholts, A.C., Beaucage, P.A., Bisbey, R.P., Chavez, A.D., Hwang, N., Park, C., Evans, A.M., Gianneschi, N.C. and Dichtel, W.R. Colloidal covalent organic frameworks. *ACS Cent. Sci.* **3**, 58-65 (2017).

S10. Hasell, T., Chong, S. Y., Jelfs, K. E., Adams, D. J., & Cooper, A. I. Porous organic cage nanocrystals by solution mixing. *J. Am. Chem. Soc.* **134**, 588-598 (2011).

S11. Zhu, G. *et. al.* Formation mechanisms and defect engineering of imine-based porous organic cages. *Chem. Mater.* **30**, 262-272 (2017).

S12. de la Peña Ruigómez, A. *et. al.* Direct On-Surface Patterning of a Crystalline Laminar Covalent Organic Framework Synthesized at Room Temperature. *Chem. Eur. J.* **21**, 10666-10670 (2015).

S13. Dong, J., Wang, Y., Liu, G., Cheng, Y., & Zhao, D. Isoreticular covalent organic frameworks for hydrocarbon uptake and separation: the important role of monomer planarity. *CrystEngComm* **19**, 4899-4904 (2017).

S14. Montoro, C. *et. al.* Ionic conductivity and potential application for fuel cell of a modified imine-based covalent organic framework. *J. Am. Chem. Soc.* **139**, 10079-10086 (2017).

S15. Li, L., Liu, X. L., Geng, H. Y., Hu, B., Song, G. W., & Xu, Z. S. A MOF/graphite oxide

hybrid (MOF: HKUST-1) material for the adsorption of methylene blue from aqueous solution. *J. Mater. Chem. A* **1**, 10292-10299(2013).

S16. Lin, K. S., Adhikari, A. K., Ku, C. N., Chiang, C. L., & Kuo, H. Synthesis and characterization of porous HKUST-1 metal organic frameworks for hydrogen storage. *Int. J. Hydrogen. Energ.* **37**, 13865-13871 (2012).

S17. Casco, M. E., Fernández-Catalá, J., Martinez-Escandell, M., Rodríguez-Reinoso, F., Ramos-Fernández, E. V., & Silvestre-Albero, J. Improved mechanical stability of HKUST-1 in confined nanospace. *Chem. Commun.* **51**, 14191-14194 (2015).

S18. Todaro, M., Buscarino, G., Sciortino, L., Alessi, A., Messina, F., Taddei, M., ... & Gelardi, F. M. Decomposition process of carboxylate MOF HKUST-1 unveiled at the atomic scale level. *J. Phys. Chem. C* **120**, 12879-12889 (2016).

S19. Mosleh, S., Rahimi, M. R., Ghaedi, M., Dashtian, K., & Hajati, S. $BiPO_4/Bi_2S_3$-HKUST-1-MOF as a novel blue light-driven photocatalyst for simultaneous degradation of toluidine blue and auramine-O dyes in a new rotating packed bed reactor: optimization and comparison to a conventional reactor. *RSC Adv.* **6**, 63667-63680 (2016).

S20. O'Neill, L. D., Zhang, H., & Bradshaw, D. Macro-/microporous MOF composite beads. *J. Mater. Chem.* **20**, 5720-5726 (2010).

S21. Chen, H., Wang, L., Yang, J., & Yang, R. T. Investigation on hydrogenation of metal–organic frameworks HKUST-1, MIL-53, and ZIF-8 by hydrogen spillover. *J. Phys. Chem. C* **117**, 7565-7576 (2013).

S22. Sun, X. *et. al*. A novel mechanochemical method for reconstructing the moisture-degraded HKUST-1. *Chem. Commun.* **51**, 10835-10838 (2015).

S23. Kok, C. M., Rudin, A. Relationship between the hydrodynamic radius and the radius of gyration of a polymer in solution. *Makromol. Chemie* **2**, 655-659 (1981).

S24. Egorov, G. I., and Kolker, A. M. The thermal properties of water-n, n-dimethylformamide solutions at 278–323.15 K and 0.1–100 MPa. *Russ. J. Phys. Chem. A* **82**, 2058-2064 (2008).

S25. Stokes, G.G. On the theories of the internal friction of fluids in motion and of the equilibrium and motion of elastic solids. *Mathematical and Physical Papers*, 102-104 (Cambridge Univ. Press, Cambridge, 1880).

S26. Andereck C.D., Liu S.S., Swinney H.L. Flow regimes in a circular Couette system with independently rotating cylinders. *J. Fluid Mech.* **164**, 155–83 (1986)

S27. Grossmann, S., Detlef L., and Chao S. High–Reynolds number Taylor-Couette turbulence. *Ann. Rev. Fluid Mech.* **48**, 53-80 (2016)

S28. Landau, L. D. and Lifshitz, E. M. *Fluid Mechanics (2nd ed., Course of Theoretical Physics, vol. 6),* 55-56. (Pergamon Press, London, 1987).

S29. Larson, R. G. *The structure and rheology of complex fluids.* (Oxford University Press, 1999).

S30. Barnes, H. A. *A handbook of elementary rheology.* (Univ. of Wales, Institute of Non-Newtonian Fluid Mechanics, Aberystwyth, 2000).

S31. Hou, J.-X., Svaneborg, C., Everaers, R. & Grest, G. S. Stress relaxation in entangled polymer melts. *Phys. Rev. Lett.* **105**, 068301 (2010).

S32. Dobrynin, A. V., & Rubinstein, M. Theory of polyelectrolytes in solutions and at surfaces. *Prog. Polym. Sci.* **30**, 1049-1118 (2005).

S33. Lifshitz, I. M. and Slyozov, V. V. The kinetics of precipitation from supersaturated solid solutions. *J. Phys. Chem. Solids.* **19**, 35-50 (1961).

S34. Wagner, C. Theorie der alterung von niederschlägen durch umlösen (Ostwald-reifung). *Zeitschrift für Elektrochemie, Berichte der Bunsengesellschaft für physikalische Chemie* **65**, 581-591 (1961).

S35. Ardell, A. J. The effect of volume fraction on particle coarsening: theoretical considerations. *Acta. Metall.* **20**, 61-71 (1972).

S36. White, R. J. The particle size distributions in systems evolving from interface-controlled to diffusion-controlled coarsening kinetics. *Mater. Sci. Eng.* **40**, 15-20 (1979).

S37. Ratke, L., & Thieringer, W. K. The influence of particle motion on Ostwald ripening in liquids. *Acta. Metall.* **33**, 1793-1802 (1985).

S38. Ratke, L., & Voorhees, P. W. *Growth and coarsening: Ostwald ripening in material processing*, 126-148. (Springer Science & Business Media, 2013).

S39. Gupalo, I. P. and Riazantsev, I. S. Diffusion on a particle in the shear flow of a viscous fluid. Approximation of the diffusion boundary layer. *J. Appl.* Math. *Mech.* **36**, 447-451 (1972).

S40. Smith, D. E., Babcock, H. P. & Chu, S. Single polymer dynamics in steady shear flow. *Science* **283,** 1724–1727 (1999).